1-1-2000

Iron and helium emission lines in Classical T Tauri Stars.

Georgina, Beristain
University of Massachusetts Amherst

IRON AND HELIUM EMISSION LINES IN CLASSICAL T TAURI STARS

A Dissertation Presented

by

GEORGINA BERISTÁIN

Submitted to the Graduate School of the
University of Massachusetts Amherst in partial fulfillment
of the requirements for the degree of

DOCTOR OF PHILOSOPHY

May 2000

Department of Physics and Astronomy

IRON AND HELIUM EMISSION LINES IN CLASSICAL T TAURI STARS

A Dissertation Presented

by

GEORGINA BERISTÁIN

Approved as to style and content by:

Suzan Edwards, Co-Chair

John Kwan, Co-Chair

Eugene Tademaru, Member

Bruce Turkington, Member

John F. Donoghue, Department Head
Physics and Astronomy

A mis Padres,

Jorge Armando Beristáin Marquez y

María Antonieta Yolanda Larraza de Beristáin

To David, my beloved.

ACKNOWLEDGMENTS

Throughout my career in graduate school, there have many people whose kindness and patience has made this period bearable, enjoyable and even possible. I would like to start by naming my advisors John Kwan and Suzan Edwards. Thank you for your patience and for caring so much. May God continue to bless you for your generous and compassionate hearts. Both of your contributions have made this thesis unique and wonderful. While working with you, I have learned much about science and my own humanity. It has been a privilege to work with both of you and I have thoroughly enjoyed our (all too brief!) times of serious talk. Thank you for your advice and your insights; thank you for those times when you poured out your heart.

I also want to mention Eugene Tademaru, who from the beginning offered a fresh perspective, helpful suggestions and much needed encouragement. I cannot begin to tell you what your words meant to me at the time; you made a huge difference in my ability to push on, when the Fe lines project seemed too big for me to do.

Dr. Turkington, thank you for agreeing to be on my committee and for your suggestions. The thesis is better for them and I hope will be of use to others even outside the field.

Our parents, both mine and David's, have provided much material assistance, endless moral support and kind words and prayers, and have made our time at graduate school pleasant and sunny, especially for Aeowyn. David, my precious

husband, best friend, *entrañable compañero*, loving father, how can I ever thank you? You have been taskmaster, editor and typesetter while teaching full time, taking care of Aeowyn and running the household business; how did you do it? Aeowyn, most precious child, thank you for your beautiful smiles, your laughter and your joy. In your 2.5 years of life, you have continually surprised and delighted us and enriched our lives beyond anything I had imagined.

And then are our friends (or fellow inmates!) at The Tower. Dearest Diane Dutkevitch, how I miss you and how many hours we spent together in fascinating conversation! Dear David Hiriart, thank you for your immense patience and resourcefulness regarding physics, astronomy, and C. I can't help but to laugh as I remember the homeworks and projects we did together. Also, thank you Milena and dearest little David (who is not little anymore!). Your influence made a difference in our decision to have our Aeowyn, WOW! There have been many other friends along the way who have enriched my life with their love and their perspectives, and with whom we have been privileged to spend happy times. Dearest among them are Mari Paz Miralles, Christine Schwarz, Chunming Li, Lynne Deutsch, Irene Grimberg, Amy Lovell and David Smith and their children, Durgesh Tiwari, Meg Lysaght, Louma Ghandour, Shuding Xie and Sandor Molnar. Several faculty members have been teachers as well as friends; among them are David and Janet van Blerkom, Steve Schneider and Ted Harrison from Astronomy, Doris and Fred Stockton from Mathematics and Engineering, respectively, Ward Motts from Geology and Matthew Ouelette from the Center for Teaching.

Lastly, I want to thank the staff at Astronomy, physics and the graduate school who have done so much to make this work possible. Foremost among them are Terri, Sandy Ostrowski, Anne Cairl, Jane Knapp, and the kind and helpful ladies at the desk in the office of degree requirements.

ABSTRACT

IRON AND HELIUM EMISSION LINES

IN CLASSICAL T TAURI STARS

MAY 2000

GEORGINA BERISTAIN, B.A., RICE UNIVERSITY

Ph.D., UNIVERSITY OF MASSACHUSETTS AMHERST

Directed by: John Kwan and Suzan Edwards

Results are presented for the He emission in 31 CTTS from the Taurus-Auriga molecular cloud spanning two orders of magnitude in the mass accretion rate, and for the Fe emission in DR Tau, based on a series of high resolution echelle spectra.

The He lines admit a description in terms of a narrow component (NC) and a broad component (BC). The NC has FWHM between 32-55 km/s and centroid velocities near zero km/s or moderately redshifted, consistent with an origin in the postshock region of the magnetospheric accretion model. The BC, with FWHM between 128 and 287 km/s and centroid velocities between -93 and +35 km/s, includes a wind and an accretion component; we argue the BC is predominantly formed in the wind. Estimates of the wind and accretion component equivalent widths are oppositely related to the NC, so the NC equivalent width increases with the accretion component but decreases as the wind component increases. The NC

is undetectable where profiles appear dominated by the wind, requiring a source of veiling other than the accretion shock to account for the observed continuum excess. Intensity ratios indicate that physical conditions are nearly uniform in the NC but span a range in the BC.

For DR Tau, the range of morphologies in 62 unblended Fe I and Fe II lines can be resolved in terms of a narrow component (NC) that dominates the weakest lines, and a broad component (BC) that dominates the strongest lines. The (NC) has FWHM $\sim$ 20 km/s and centroid velocity near zero km/s. The (BC) has FWHM $\sim$ 100 km/s, and a tendency to be blueshifted by $\leq$ 10 km/s. Estimates of iron line opacities τ and column densities N yield $\tau_{NC} \sim 3 \times \tau_{BC}$, $N_{FeI} \gtrsim 10^{17} - 10^{18}\,\mathrm{cm}^{-2}$, and $N_{FeII} \gtrsim 10^{18} - 10^{19}\,\mathrm{cm}^{-2}$ for the BC. Estimates of kinetic temperature for iron suggest that the NC gas is hotter than the BC by several thousand degrees. For iron, the NC is consistent with an origin in the postshock gas while the BC may originate in the inner accretion disk close to the corotation radius.

TABLE OF CONTENTS

LIST OF TABLES

LIST OF FIGURES

CHAPTER 1

INTRODUCTION

The research presented in this thesis has two main thrusts into the study of Classical T Tauri Stars. The first part is a comprehensive study of the helium emission in a sample of 31 of these objects. The second part comprises an in depth study of permitted iron emission lines in the spectrum of the single Classical T Tauri star DR Tau (Beristain, Edwards & Kwan 1998). Below I use the results of a large body of observational and theoretical work. For references, and a complete treatment of several of the aspects of low-mass star formation, the interested reader may consult the excellent reviews by Natta (1999) and Hartmann (1998).

Classical T Tauri stars (or CTTS) are thought to be young ($T \leq 10^7$ yrs), low mass ($M \sim 0.5 M\odot$) objects believed to represent the latter stages of star formation, after most of the parent cloud remnant has been removed by outflows or accreted onto the central object. They are often associated with molecular cloud material. The objects in this study are located in the nearest star formation complex, the Taurus molecular cloud, $\sim$ 140 pc away. Despite their association with dense cores of molecular clouds, their photospheres are optically visible, so that in principle, their spectral type and luminosity and thus masses and ages can be determined. In practice, optical continuum and infrared emission above levels expected for cool (4,000 K) photospheres as well as a multitude of emission lines overlying the stellar

absorption spectrum complicate their analysis and indicate that non-stellar processes are occurring. The optical emission lines include permitted transitions due to hydrogen, helium, and lower excitation metals such as sodium, calcium, iron and iron group elements and 'forbidden' lines from oxygen, nitrogen, sulfur and iron. Therefore, the emission line spectrum represents a range of gas densities and temperatures. The velocity profiles of the emission lines show that complex and high speed motions are taking place in these systems. Figure 1 shows a sample of emission lines from the object DR Tau, a CTTS with large levels of optical continuum emission and a rich emission spectrum (the object of the second part of this study). The profiles present a variety of line widths, shapes and multiple absorption components suggesting that regions of distinct physical properties are responsible for the emission. With respect to the stellar photosphere, the blueshifted absorption in Hα and Na I and the blueshifted emission in [OI] are signatures of outflowing material, while the redshifted absorption of the He I and Na I lines indicate infalling gas.

The present conceptual framework for CTTS is that of a pre-main sequence star surrounded by a rotationally supported accretion disk. As originally suggested by Lynden-Bell & Pringle (1974), if accretion occurs directly onto the stellar surface, a boundary layer is set up where matter moving at the Keplerian velocity $v_{phi} \sim$ 200-300 km s^{-1} , dissipates most of its rotational energy to match the slowly moving photosphere, with velocity between 10-30 km s^{-1} . The accretion disk model naturally accounts for the infrared excess as due to dust emission, and explains the optical continuum excess as due to energy dissipated at the boundary layer. The disk geometry explains our ability to see the stellar photosphere in spite of the amounts of dust required, which if uniformly distributed around the star would occult it with a few hundred magnitudes of extinction. Mass accretion rates needed

to account for the excess continuum emission in CTTS range from $10^{-9} M\odot$ yr^{-1} to $10^{-6} M\odot$ yr^{-1}.

These stars are believed to have fully convective interiors and can therefore generate dynamo magnetic fields. If the stellar field is of order $\sim$ 1 kG, it can disrupt the structure of the accretion disk near the star (Ghosh & Lamb 1979; Konigl 1991) near to the co-rotation radius, typically a few stellar radii, where the disk angular velocity equals the stellar angular velocity. In the case of magnetically controlled accretion, the boundary layer is replaced by an accretion shock at the stellar surface, where matter falling in at supersonic velocities is deposited onto the stellar surface. The influence of the magnetic field can account for phenomena that are not readily understood if a boundary layer mediates the star-disk interaction. The high speed infall indicated by the redshifted absorption features in the emission lines (cf. Fig 1) can be understood as arising from gas that is falling along the magnetic field lines at nearly free-fall speeds and is seen against the hot continuum from the accretion shock. The photometric modulation observed in these stars can be interpreted as 'hot spots' that rotate in and out of view and are due to emission from the accretion shock of a magnetosphere that is not aligned with the rotation axis. The rotational velocities of CTTS, which are lower than those of similar age stars without disk accretion signatures, is a puzzling result if CTTS are accreting high angular momentum material. While the details of how this could be accomplished are unknown, in the magnetospheric accretion model the stellar magnetic field couples to disk regions with smaller angular velocity than the star, counteracting its tendency to spin up by coupling to regions inside the corotation radius, where mass accretion can occur.

Winds and outflows are observed at all stages of star formation, from the early phases when most of the stellar mass is accreted in deeply embedded and heavily

extincted protostars, to the older and optically revealed CTTS. Outflows are closely linked to mass accretion; objects of similar ages but without accretion disk indicators also lack outflow signatures. Outflows may be essential to the star formation process as reservoirs of excess angular momentum that must be shed if accretion is to proceed. At the same time the powerful molecular outflows driven by embedded protostars clear away parent cloud material, setting a limit to the final mass of the star.

Although the mechanism that drives the winds and their region of origin is unknown, present models rely on magnetic fields and rotation to eject and collimate disk material. The wind must arise close to the star, so that mass can be ejected at a velocity larger than the escape velocity and be observable as a jet or outflow. The efficiency of conversion of the potential energy of the infalling mass into the kinetic energy carried by the wind is indicated by the ratio of the mass loss in the wind to the mass accretion rate through the disk, $\dot{M}_w/\dot{M}_{acc}$. Since some of the energy which could power the wind is radiated away, it is reasonable to expect that even in the limit of 100% efficiency of conversion $\dot{M}_w/\dot{M}_{acc} < 1$. Current estimates of $\dot{M}_w/\dot{M}_{acc}$ in CTTS range from 10^{-2} to 10^{-1}, using the jet emission from the the [OI] lines to estimate $\dot{M}_w$ and the the excess continuum emission to estimate $\dot{M}_{acc}$. In addition to the molecular outflows from embedded sources and the spatially resolved, collimated jets radiating in the forbidden lines of CTTS, observational evidence suggestive of winds emanating from the surface of disks exists. In CTTS, the low velocity component of the forbidden line emission, which shows small outflow velocities and is denser and of lower excitation than the high velocity component ascribed to the jet, has been spatially resolved as a compact source close the star and is thought to represent a slow disk wind or a disk corona. In FU Ori, from a class of objects believed to represent low mass stars with much higher accretion

rates than CTTS, spectroscopic signatures of outflowing and rotating material have been similarly attributed to a disk wind.

While the forbidden emission lines in CTTS have been convincingly explained in terms of jets and disk winds/coronae, the origin of the permitted emission lines in CTTS has yet to be established. The goal of this study is to provide observational constraints for models of these objects using He, with upper levels at energies $\leq$ 24.6 eV, and Fe, with upper levels at $\leq$ 7.8 eV. Each of these necessarily probes energetically different regions and together can provide a complementary picture of the circumstellar environment. The data set is comprised of high resolution echelle spectra covering optical wavelengths for 31 objects that span two orders of magnitude in the mass accretion rate. The velocity profiles contain the kinematic information necessary to constrain their origin and the equivalent widths of transitions can be used to obtain estimates of physical conditions.

The emission line profiles used throughout this work are residual profiles free from the contributions of the underlying stellar photosphere and extracted according to the procedure described in Hartigan et al (1989) and used in Hartigan et al (1995) to obtain measurements of the continuum excess or veiling emission for the stars in this study. The top panel of Figure 2 shows the spectrum of LK Ca7, a standard star of the same spectral type (mass and temperature) and luminosity class (size and gravity) as the CTTS GG Tau in the bottom panel. The CTTS spectrum shows absorption features with the same relative depth to each other as those of the standard, indicating a similar spectral type, but the spectrum is said to be 'veiled' because the absorption lines are shallower, indicating that the continuum level against which they appear is larger. The procedure for extracting residual emission profiles can be briefly described as follows. The GG Tau spectrum, which consists of emission line and excess continuum contributions on top of a normal

stellar absorption spectrum, is modeled as the sum of a standard template plus a flat continuum over short wavelength intervals of $\sim$ 15 Å. The spectrum of the standard is 'veiled' until the depth of its photospheric features match those of the standard. The difference in depth between absorption lines in the observed object spectrum and in the veiled standard yields residual emission lines. In Figure 2 the heavy lines show the observed spectrum, the lightweight lines superposed on the observed spectrum are the standard spectrum, and the light lines underneath the observed and standard spectra are the residuals. The figure shows that the residual emission in LK Ca7 in this wavelength range is undetectable when its spectrum is compared to that of a main sequence star without excess emission. In contrast, when compared to LK Ca7, the veiled GG Tau spectrum has a ratio of excess continuum to photospheric emission, or r, equal to 0.3 and prominent residual emission lines.

The analysis of the He I emission lines in 31 CTTS (chapter 2) extracted as described above shows that the narrow and broad emission components apparent in the lines possess different kinematic properties. Intensity ratios in each component exhibit different distributions, lending support to the notion that these components arise from physically distinct regions, as suggested in the literature. The narrow component or *NC* is consistent with an origin close to the stellar photosphere near the accretion shock, in agreement with previous studies of the narrow He emission. A new result of this work is that the He I broad emission kinematics can be consistently interpreted as composite, including an accretion component whose properties are consistent with an origin in the funnel flow close to the accretion shock, and a wind component. Further, the wind and accretion components of the broad emission seem to bear a different relation to the *NC* emission region. The increase in the wind emission strength as the *NC* emission strength decreases is

due either to opacity effects or to a redistribution of the accretion flow in favor of the wind at the expense of the *NC* emission region. In either case, more than one source of continuum excess emission is called for in at least a subset of these objects with dominant *BC* emission but undetectable *NC* emission. The severe excitation conditions required by He restrict its origin to the inner disk/star region, where the accretion energy can be tapped to power the wind. The possibility that a wind is a common and a significant contribution of the He *emission* in CTTS means that further study of its properties may ultimately indicate the origin of the wind in these objects.

In chapter 3, analysis of 62 unblended Fe I and Fe II emission lines in the object DR Tau reveals that the kinematics of these lines can be consistently described in terms of narrow and broad components, which differ from their counterparts in He in that both of the Fe components are narrower by about a factor of 2, and the Fe *BC* is less blueshifted. From intensity ratios for selected pairs of lines, the Fe *NC* is found to be more optically thick and hotter than the Fe *BC*, consistent with an origin for the *NC* close to the accretion shock. The *BC* probably arises in the disk, close to the co-rotation radius, where the excess rotational energy of disk material is dissipated.

Of the sample of objects studied in this work, ~25% are known to be binaries. The significance of multiple systems in our understanding of mass accretion in Classical T Tauri stars is only now beginning to be realized. Of the two known spectroscopic binaries included in our sample, DQ Tau and UZ Tau E, there is orbital (Mathieu et al. 1997) and spectroscopic (Basri et al. 1997) information available only for DQ Tau. This object has an orbital period of 15.8 days, an orbital eccentricity $e = 0.556$ and a separation at periastron of 8 stellar radii, with a mass ratio between 0.7 and 1 (Mathieu et al. 1997). The object is inferred to

have a circumbinary disk from sub-millimeter and infrared excess emission and is known to become brighter and bluer, with (sometimes dramatic) increases in emission line strengths and continuum veiling as the system nears and passes through periastron. Therefore, it is remarkable that the accretion indicators for this object are so similar to those observed from single CTTS, as noted by Basri et al. (1997). Moreover, since the emission lines and continuum veiling are evident throughout the orbit, low-level accretion appears to occur at all times. The authors note that their observations are consistent with predictions from a model postulated by Artymowicz & Lubow (1996), where mass streams dislodged from the circumbinary disk at apastron can cross the central gap and land on the binary components, causing periodic accretion episodes at specific orbital phases. While the energy in the stellar magnetospheres is inferred to be adequate to power the outbursts and the stellar magnetospheres would be expected to interact at periastron, the larger level of continuum veiling and duration of the outbursts suggest to the authors that these are not powered exclusively by such interactions. Whether accretion from the circumbinary disk or interaction of the stellar magnetospheres is the dominant power source in this system, its significance for the understanding of CTTS is that mass accretion in these objects does not appear to require the presence of a stable circumstellar disk. The details of these interactions will have to be established if CTTS turn out to be mostly binary or multiple systems.

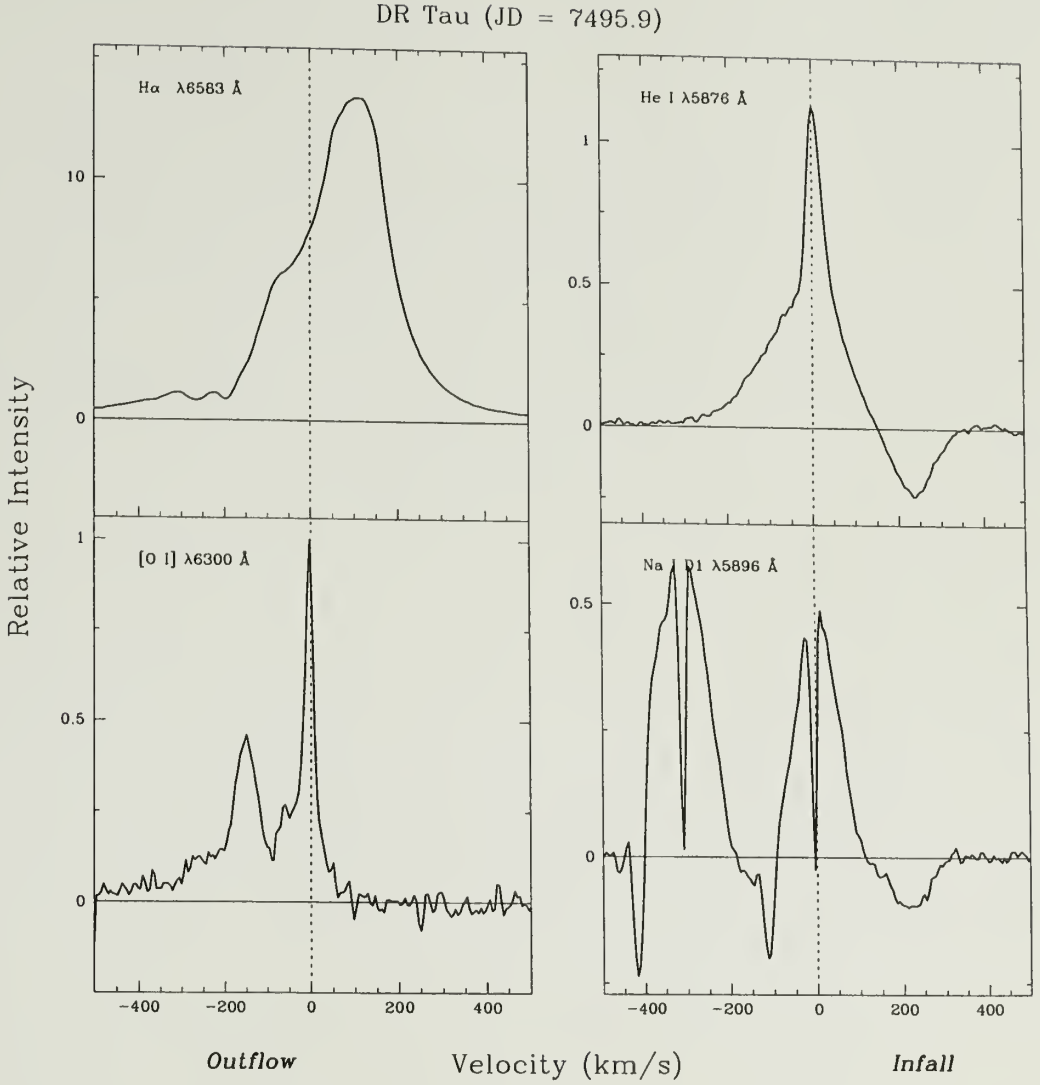

Figure 1. Simultaneous velocity profiles in DR Tau. Permitted line emission spans excitation energies from $\sim$ 2 eV for Na I to $\sim$ 23 eV for He I and show a velocity structure suggestive of origins in distinct regions. The line width and the multiple absorption components indicate high velocity motions including infall and outflow. The blueshifted component in [O I] λ6300 Å indicates a collimated, low density wind, while the sharp blueshifted absorption in Na I indicates a denser and cooler collimated wind. Redshifted absorption in He I and Na I show high speed infall. Intensities are units of the local continuum and velocities are with respect to the stellar photosphere.

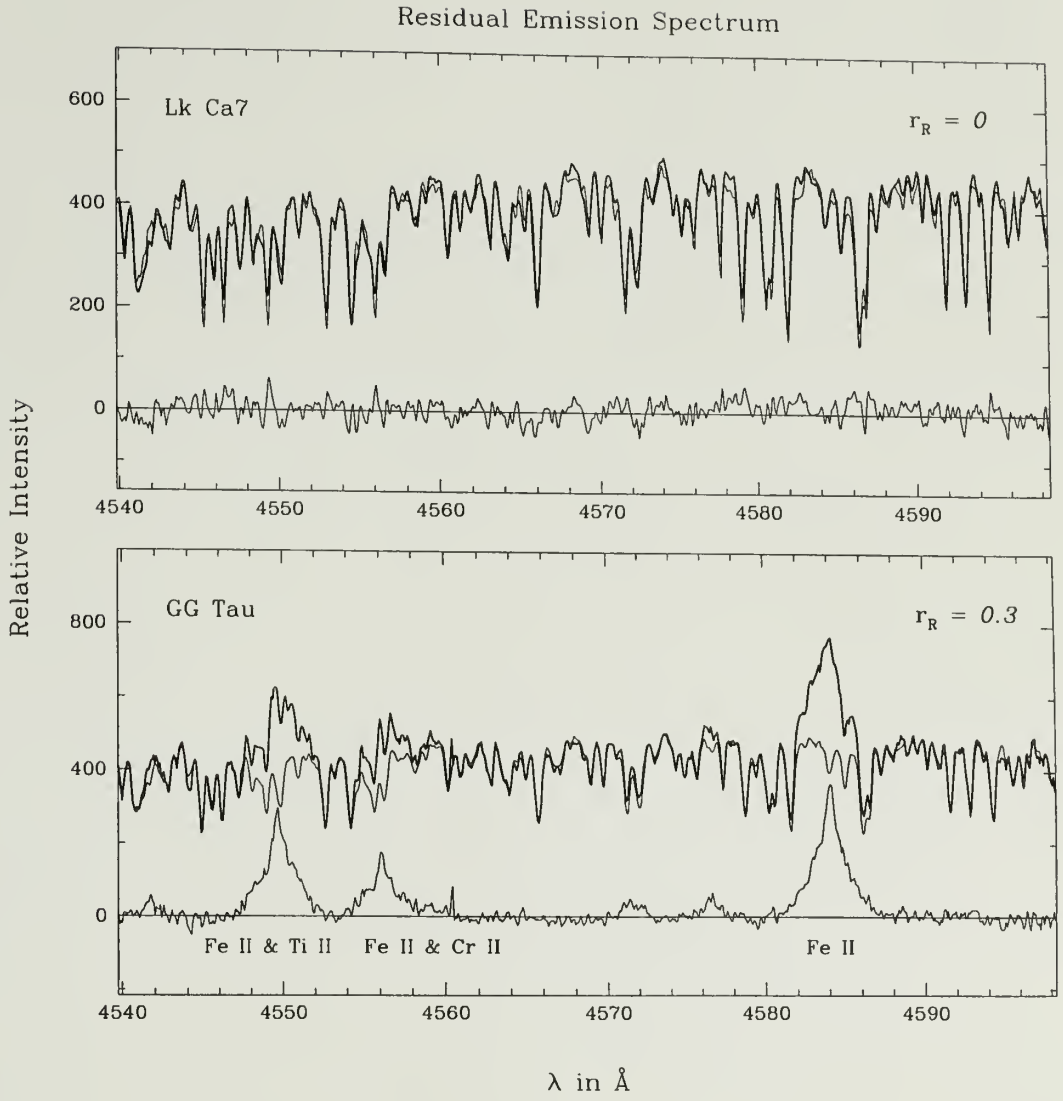

Figure 2. Emission lines like those in Figure 1 are obtained by comparing the observed spectrum of a CTTS (GG Tau, bottom) with that of a spectral standard (LK Ca7, top) without excess continuum emission. The standard is 'veiled' (light line) until the depth of its absorption lines match those of the object (heavy line). The residuals of the fit is the excess emission shown underneath the object spectrum. LK Ca7 has zero residuals when its spectrum is compared to that of a main sequence star without excess emission. In contrast, when compared to LK Ca7, GG Tau has a ratio of excess continuum to photospheric emission or r equal to 0.3 and prominent residual emission lines.

CHAPTER 2

HELIUM EMISSION IN CTTS

2.1. Helium Emission: an Overview of Results

The results of a comprehensive study are presented for the He optical emission in a sample of 31 CTTS spanning two orders of magnitude in the inferred mass accretion rate. The data is comprised of a series of high resolution echelle spectra over two discontinuous and non-simultaneous spectral ranges, $\approx \lambda\lambda$5000-6700 Å and $\approx \lambda\lambda$4000-4920 Å. The He I emission lines admit a description in terms of a narrow component (*NC*) and a broad component (*BC*), as found in previous studies. The *NC* kinematics are consistent with an origin in the postshock region in the magnetospheric accretion model, with FWHM $\leq$ 47 km s^{-1} for He I and $\sim$ 55 km s^{-1} for He II and centroid velocities that are slightly redshifted for both ions. In contrast to the *NC*, the *BC* kinematics for the triplet λ5876 line span a large range, with 128 $\leq$ FWHM $\leq$ 287 km s^{-1} and centroid velocities between -93 and +35 km s^{-1} .

For the 22 stars with detectable *BC* emission, the expected kinematics from an aligned axisymmetric magnetosphere are incompatible with the centroid velocities in 18% of the stars and with the maximum blue wing velocities in 41% of the stars. We argue that the bulk of the *BC* emission in these objects is formed

in a wind. In addition, for every one of these objects, the relative strength of the *BC*, *BC/NC*, is larger than 1, suggesting that the dominance of the *BC* in the observed profiles is due to the wind. The *BC* kinematics for objects with redshifted centroid velocities are consistent with emission from the magnetospheric funnel flow close to the accretion shock. Multiple observations for 7 of the objects with detectable *BC* emission suggest that the blueshifted emission is more variable than the redshifted emission. The *NC* equivalent widths decrease as the estimated the wind contribution to the *BC* increases. In contrast, the *NC* equivalent widths increase as the estimated accretion contribution to the *BC* increases. The *NC* is undetectable in AS 353A, CW Tau and HN Tau, which exhibit *BC* profiles we believe to be dominated by the wind. For these objects at least, a source of veiling other than the accretion shock is indicated to account for the detectable continuum emission.

Comparison of the *BC* emission with the singlet λ6678 line supports the conclusions reached from analysis of λ5876 and in addition suggests that *BC* emission from λ6678 is favored in the infall component. Equivalent width ratios for the *NC* and the *BC* in λ5876 and λ6678 suggest that physical conditions are nearly uniform in the *NC* but larger in the *BC*.

2.2. Introduction

The origin of the emission line spectra of Classical T Tauri stars remains a subject of debate. The line spectra suggest the presence of a complex circumstellar environment able to power transitions spanning a large range in excitation and ionization potentials where high speed infall and outflow motions may occur simultaneously. Emission lines due to H, Ca II and Mg II, He I, Na I, Fe II and Fe I and

other singly ionized and neutral metals, as well as lines of C III, C IV, Si III and Si IV are observable in the spectra of these objects. Often the most prominent optical line after Hα is due to He I λ5876. The present consensus is that CTTS are young stars of late spectral type undergoing magnetically controlled disk accretion. In this scenario the ionized disk component couples to a strong stellar magnetic and freely falls toward the star, creating a standing shock close to the stellar surface (Uchida & Shibata 1985; Camenzind 1990; Konigl 1991) that can, in principle, produce the short wavelength continuum excess. An efficient coupling of the stellar magnetic field to the disk beyond the corotation radius may regulate the angular momentum evolution of of the central object, resulting in the observed low rotational velocities of CTTS (Bouvier et al. 1993, 1995; Edwards et al. 1994).

The emission line spectra have been variously attributed to active chromospheres (Cram 1979; Calvet, Basri & Kuhi 1984; Calvet et al. 1985), winds (Kuhi 1964; Hartmann, Edwards & Avrett 1982; Hartmann et al. 1990; Natta & Giovonardi 1990; Calvet, Hartmann & Hewitt 1992; Mitskevich, Natta & Grinin, 1993) the boundary layers resulting from disk accretion onto the central object (Bertout, Basri & Bouvier 1988; Basri & Bertout 1989) and to magnetospheric accretion columns (Hartmann, Hewett & Calvet 1994; Muzerolle, Calvet & Hartmann 1998). While there is evidence to support the notion that magnetospheric accretion dominates the mass motion in CTTS, spectroscopic and other observational data remain that defy interpretation in terms of this model, as summarized by Edwards (1997). Among the unanswered questions in the problem of the origin of the emission lines are the geometry and velocity fields of the line emission region, and the sources of the short and long term variability in the emission lines.

The lines of neutral and singly ionized helium require a strong ultraviolet flux or a high temperature for excitation, as the first excited states lie $\sim$ 20 and 40 eV

above the ground, respectively. In the Sun, the He spectrum is thought to originate in the chromosphere and in the transition region and has been observed in quiescent prominences. If primarily due to collisional excitation in the transition region, temperatures between 25,000 and 90,000 K are required (Athay 1965; Avrett, Vernazza & Linsky 1976). If due to photoionization of chromospheric helium by the coronal radiation field followed by recombination and cascade (Goldberg 1939; Hirayama 1971), the excitation can take place at local kinetic temperatures between 8,000 and 15,000 K (Zirin 1975; Heasley, Mihalas & Poland 1974; Wahlstrom & Carlsson 1994). Therefore, the He I and He II lines in CTTS may arise very close to the central star and represent a potential diagnostic of physical conditions of the energetic inner accretion disk region.

Several observational studies of CTTS have employed selected He I and He II lines as diagnostics of the conditions of formation; however, no consensus has yet been reached about their origin. Schneeberger, Linsky & Worden (1978) measured the λ5876 and λ6678 lines in DF Tau and BP Tau and found the intensity ratios to be $\sim$ 3 for both objects. Ulrich & Wood (1981) carried out a study of the λ5876 and λ10830 lines in eight TTS in order to test the predictions of line formation under wind, chromospheric and nebular conditions. They concluded that the 10,830 line is optically thick in every case and found that half of their sample object profiles are compatible with chromospheric formation while the rest could be formed under wind or nebular conditions. In a comprehensive study of the emission lines of the star T Tauri, including the He II λ1640 line, Brown, Ferraz & Jordan (1984) obtained limits for the electron pressures and concluded that a two-component atmosphere is required to account for the range of spectral properties. Using the observed luminosity of the He II λ1640 line in RU Lupi and T Tauri, Lamzin (1989) argued that the He II λ4686 line should be optically thin in CTTS and computed

expected profile shapes for an expanding chromosphere, an accretion disk and disk chromosphere model.

Global properties of the metallic emission lines in CTTS were elucidated by Hamann & Persson (1992), who examined the spectra of 53 TTS at high resolution and found that the line profiles exhibit narrow ($\leq$ 40 km s^{-1}) and broad ($\geq$ 100 km s^{-1}) components, with the He I and He II lines often characterized by narrow cores. The narrow component, or *NC*, was attributed to an active stellar chromosphere and the broad component, or *BC*, to a turbulent, nonspherical envelope. Later studies of the He lines in CTTS at high resolution suggest that the relationship between the He emission properties and disk accretion indicators, such as veiling and the Hα intensity, is complex. In a study of the *NC* emission in λ5876 in a sample of 28 TTS, Batalha, Stout-Batalha, Basri & Terra (1996) found correlations between the *NC* and *NC* line strengths and the optical veiling, and proposed a "hot chromosphere" region where the shock accretion energy is reprocessed, as the formation site for the *NC*. In a variability study of DF Tau, Johns-Krull & Basri (1997) found no correlation between the He I λ5876 *NC* emission and the veiling. While the *BC* emission was found to be weakly correlated with veiling, the equivalent widths for the λ5876 *BC* and for Hα were uncorrelated and the Hα line showed no apparent relation to veiling. Observational evidence is now emerging that challenges the notion that the broad permitted emission lines can arise from magnetospheric accretion funnel flows. After examination of the permitted emission lines in 30 stars, Alencar and Basri (2000) conclude that while magnetospheric accretion probably does happen in CTTS, it is not the only important process for line formation. They found that only $\sim$ 20% of the *BC* profiles support the model predictions, as the broad emission components in He I and Ca II are most often symmetric, and sometimes redshifted. In addition, the *BC* line

strengths for different atomic transitions are not correlated as expected if they all arise in the funnel flow. Muzzerolle, Hartmann & Calvet (1998) found that the observed profiles of He I 5876 for some high veiling objects in a sample of eleven CTTS could not be reproduced by a non-rotating magnetospheric accretion model with dipole geometry.

In chapter 3 of this thesis (see Beristain, Edwards & Kwan 1998) the properties of iron emission in the object DR Tau are described and shown to be a valuable diagnostic of the line opacity, column density and the kinetic temperature in the inner accretion disk environment. The neutral and singly ionized iron optical spectra arise from levels below $\sim$ 6 eV from the ground state that are easily excited by inelastic collisions with thermal electrons at temperatures ($T \leq 10^4$). If predominantly collisional, their excitation requires local heating, which restricts their origin to the inner accretion disk where dissipation of rotational energy of the disk material takes place close to the corotation radius and at the post shock region on the stellar surface. The study of He I and He II optical emission allows the exploration of transitions which must necessarily represent conditions in a more energetic environment in CTTS, closer to where the final deposition of mass onto the star occurs or where the launching of the winds takes place.

In this chapter we present the results of a detailed study of the narrow and broad component emission for the helium optical lines in a sample of 31 CTTS, in order to determine the fundamental properties of the line emission region and provide further observational constraints for future modeling efforts. The analysis is based on the simultaneously observed He I triplet λ5876 and singlet λ6678 lines in the red and the simultaneously observed He I triplets λ4471 and λ4713 and the He II λ4686 line in the blue. The chapter is organized as follows: The atomic parameters for the observed unblended He lines, data reduction and selection of the reference

sample is in §3. The analysis of the narrow component (NC) for all detected He I and He II transitions is discussed in §4. Findings for the broad component (BC) in λ5876, discussed in §5, suggest that the BC itself is composite, including a wind and an accretion contribution. Evidence is presented that suggests the wind contribution of the BC increases as the NC emission decreases and is eventually undetectable, implying that more than one source of veiling continuum emission exists in CTTS. The BC emission in λ6678 is in §6, and yields results consistent with λ5876. Equivalent width ratios for simultaneously observed line pairs, presented in §7, differ between the NC and BC, and further suggest a composite BC. The discussion is in §8 and a summary of conclusions in §9.

2.3. Data Reduction

2.3.1. Line Identification

The He I spectrum contains a large number of optical transitions that take place between levels lying at $E_u \leq 24.5$ eV and $E_l \geq 19.8$ eV from the ground level. Unfortunately, the majority of lines in our spectra with wavelengths redward of λ4000 Å are blended with other metallic emission features, most notably Fe I and Fe II. The four unblended transitions include the most prominent optical line in CTTS after Hα, He I λ5876 ($A = 7.1 \times 10^7$ s^{-1}), and also λ4472 ($A = 2.5 \times 10^7$ s^{-1}), and λ4713 ($A = 1.1 \times 10^7$ s^{-1}), arising from the triplet levels 3^3D, 4^3D, and 4^3S, respectively, with energies at 23.07 eV, 23.73 eV and 23.59 eV above the ground level. The λ6678 singlet line ($A = 6.4 \times 10^7$ s^{-1}) arises from the 3^1D level at 23.07 eV and decays to the 2^1P level. The one He II transition observed, λ4686, ($A = 1.4 \times 10^8$ s^{-1}) arises from the n = 4 level at 50.80 eV above the ground

level. Given the large energy differences between the first excited states and the ground state in He I and He II , the most efficient way to populate these states is by electron capture and cascade following ionization.

The He I singlet and triplet spectroscopic terms do not mix via permitted transitions. This means that the crucial distinction between the singlet and the triplet line strengths, and specifically between the simultaneously observed λ6678 and λ5876 lines, derives from the nature of the radiative coupling of their lower levels with the ground state. The singlet n^1P levels, including the lower level for λ6678 2^1P, decay preferentially to the ground state by the strong permitted Lyman lines 1^1S-n^1P. In particular, the 2^1P level decays to the ground via a λ584 photon ($A = 18 \times 10^8$ s^{-1}). In contrast, the preferred decay paths for the triplet levels, including the λ5876 lower level 2^3P, all lead to the lowest triplet level, 2^3S, which is extremely metastable ($A = 1.3 \times 10^{-4}$ s^{-1}) and are radiatively coupled to the ground state only by forbidden transitions. The λ5876 lower level 2^3P decays to the ground state by a forbidden inter-system λ591 photon that violates the dipole selection rule for allowed spin changes between transitions.

Under conditions of low density where the Lyman resonance transitions are not very optically thick, emission in the triplet lines, including λ5876, will be favored over that in λ6678. The singlet λ6678 lower level population is quickly depleted by the resonance transition. Therefore enhancement of the λ6678 intensity over the pure recombination value by collisional excitation of its upper level from 2^1P or from the metastable level 2^1S is unlikely. At densities high enough to make the resonance transitions very optically thick, however, a larger population of the λ6678 lower level can be sustained. Collisional excitation from either 2^1P or 2^1S can then enhance the intensity of λ6678 over that arising from pure recombination. For the triplets, on the other hand, the metastability of their lowest level 2^3S allows the

buildup of population, and in turn makes collisional excitation of their upper levels more likely even at low densities. Collisional excitation from either 2^3S or 2^3P to the 3^3D, 4^3D and 4^3S levels can enhance the intensities of λ5876, λ4471 and λ4713 over their pure recombination values. An increased collisional coupling between the singlet and triplet levels as might occur at higher densities would allow the transfer of population between the two spin systems and drive the level populations towards their thermal equilibrium values.

The He II n = 4 level gives rise to three transitions, λ4686, the resonance λ243 line ($A = 2.05 \times 10^8$ s^{-1}) and λ1215.1 ($A = 1.35 \times 10^8$ s^{-1}). The latter line is only 0.6 Å away from the center of the Lyman α transition of hydrogen, expected to be very strong in CTTS. The resulting fluorescence of the n = 4 level may the most important factor affecting the observed intensity of He II λ4686 in CTTS.

2.3.2. The Sample and Parameter Fits

The echelle spectra used in this He I emission line study have formed the basis for two previous publications on the Balmer and forbidden lines in 32 cTTS and 10 weak emission T Tauri stars (EHGA and HEG). All spectra were taken with the 4 meter Mayall telescope at KPNO with a velocity resolution of $\sim$12 km s^{-1}. The spectra cover two wavelength regions, the red, with wavelength coverage $\approx$ $\lambda\lambda$5000-6800 Å and the blue, with wavelength coverage $\approx$ $\lambda\lambda$4000-4950 Å. These were observed non-simultaneously. The data reduction for these spectra, including determination of the veiling and discussion of how the residual emission profiles are obtained, is fully described in the two previously published papers. Every object in those studies is considered here, with the exception of RY Tau, the only object which exhibits an absorption profile at λ5876. Among the 31 remaining CTTS, 8 are known to be binary systems (DD Tau, DF Tau, DK Tau, DL Tau, DQ Tau,

GG Tau, UY Aur and UZ Tau E) and 9 are known to be single stars (AA Tau, BP Tau, DE Tau, DN Tau, DO Tau, DS Tau, GI Tau, GK Tau and GM Aur); see Leinert et al. 1993, Mathieu 1994, Mathieu et al. 1996, Mathieu et al. 1997, Simon et al. 1992, Simon & Prato 1995 and Simon et al. 1995. The multiplicity for the other stars is unknown. Among the binaries, DF Tau is a close binary (Thiébaut et al. 1995) and DQ Tau and UZ Tau E are spectroscopic binaries. Gullbring et al. (1998) note that the stellar luminosity of DF Tau is too large for its spectral type and suggest that a correction for the secondary component may be necessary.

Sixteen of the 31 CTTS were repeatedly observed in the red and 6 were repeatedly observed in the blue, from 2 to 5 times. The line profile in the majority of objects with repeat observations is variable, making it necessary to designate a single epoch (henceforth the 'reference sample') to be included in the study of the entire sample. The variability aspect will be addressed later. The first criterion for selecting the reference sample is to maximize the magnitude of the FWHM in the strongest line, λ5876 in the red and λ4471 in the blue. Among epochs with comparable profile morphology, the epoch with optimal S/N of the simultaneously observed weaker lines was selected for the reference sample. Finally, for a few objects observed in the blue, the selection criterion is modified to favor the epoch where λ4471 exhibits the smallest degree of blending from Ti II .

Among the observed unblended lines, λ5876 is detected in every object in the reference sample and is the most prominent optical line after Hα. For the purposes of this chapter, it shall be considered as the prototype of He I emission and constitutes the starting point for analysis. The most striking characteristic of the He I λ5876 profiles in the reference sample, immediately evident from Figures 3 and 4, is the range of morphologies presented. The profiles admit a classification into three types: broad (N= 3), composite (N = 19) and narrow (N = 9). Of the 10

WTTS observed, only three, displaying narrow profiles, have detectable emission in λ5876. Narrow profiles are symmetric and can be well fit by a Gaussian function; in contrast, broad profiles are generally asymmetric. A profile is considered composite if its overall shape is not Gaussian and if, in a two-Gaussian fit, its components differ in FWHM by at least a factor of 3.

Figure 5 shows a superposition of λ5876 profiles and the corresponding average in each of the morphological types. Objects within the narrow type exhibit a comparable width and centroid velocity. Further, the narrow profiles and the narrow cores of the composite profiles appear indistinguishable, as shown by the averages. On the other hand, both the broad profile average and the composite average wings display similar blueshifted asymmetry. The near uniform properties of the narrow profile/core, the distinct contrast and the large range in relative strength between the narrow profile/core and the broad profile/base, and the often simultaneous presence of both emissions indicate that the above characteristics are not due to line-of sight projection effects of a single emission region, but that at least two distinct regions, of widely differing kinematic properties, contribute to the He I line, as originally postulated by Hamann & Persson (1992).

In order to obtain a quantitative characterization of the profiles, the narrow and composite group members were fit with single and double Gaussian functions, respectively. The relative amplitude, width and centroid of each Gaussian are the undetermined parameters. Fits are optimized by minimizing the χ^2 statistic, and uncertainties in the parameter estimates are calculated by inverting the curvature matrix of the χ^2 function evaluated at the best fit parameter set (Press et al 1992). The resulting formal errors in the estimates rarely exceed 10% except in a few objects with weak emission and low S/N, where the errors may reach 20-30%. Unconstrained Gaussian fits yield adequate descriptions in the majority of

cases except for the objects UY Aur, RW Aur and DR Tau which can at times exhibit pronounced asymmetries. For these objects optimal fits required setting the centroid velocity of the narrower component to a value estimated by visual examination of the profile core. In these cases, the uncertainty in that centroid velocity is between 5 and 7 $\mathrm{km\,s^{-1}}$.

Results from the best Gaussian fits for each transition show that the parameter sets for the narrow profiles and for the cores of the composite profiles are indistinguishable within the errors of estimation, allowing a consistent definition of the narrow component, or *NC*, for each transition. The double Gaussian fits for a composite profile also yields parameter fits for the broad profile underlying the *NC*. As they are both much broader than the *NC*, the broad components in the composite profiles and the broad profiles are considered together as the Broad Component or *BC*. The near uniformity of the *NC* parameters and the small associated uncertainties allows the *NC* to be well characterized. This permits the subtraction of the best fitting *NC* parameters from each composite profile in order to obtain a residual *BC* profile that can be examined in greater detail (see §4). The latter is uncertain at velocities that underlie the *NC*; between -50 and +50 km/s; therefore, the residual *BC* profile is replaced by the best *BC* Gaussian fit. In our sample, the *NC* is detected in every He I line and in the He II line, while the *BC* is detected and free of blends only in He I λ5876 and λ6678.

The best fit profiles are superposed on the observed λ5876 profiles in Figure 3. A comparison between the *NC* and the *BC* best fit parameters for λ5876, illustrated in Figure 6, shows that they have clearly distinct distributions. The *NC* kinematics are discussed more fully in the following section. Here it is noted that the *NC* equivalent widths show no relation to the observed excess continuum emission, or 'veiling', contrary to expectation if the *NC* emission is due to the cooling of gas

heated in the accretion shock. Figure 7 shows the *NC* equivalent widths versus the observed veiling r_R for the reference sample. The figure suggests that the emission responsible for the veiling is a complex variable that may not be directly linked to the properties of the *NC* emission region. In contrast, the *BC* equivalent width distribution suggests a weak correlation with veiling. Indeed, in the section on the *BC*, evidence is presented to suggest that the *BC* is itself composite and that CTTS possess more than one source of veiling continuum emission.

In the following section, the results for the *NC* in the four He I lines and the He II line are described. The *BC* is considered in §4.

2.4. The Narrow Component

The *NC* FWHM and centroid velocity distributions found for each transition are shown in Figure 8 and their averages are listed in Table 1. Within a given transition, the *NC* exhibits a narrow range of the FWHM and centroid velocity. Among He I transitions, however, the stronger line displays the larger FWHM as noted by Hamann & Persson (1992). Thus He I λ5876 exhibits an average FWHM of 47 ± 7 km s^{-1} while the weaker He I λ4713 has an average FWHM of 34 ± 9 km s^{-1} . The He II λ4686 line exhibits a larger FWHM than the simultaneously observed He I lines, with average FWHM of 55 ± 10 km s^{-1} . The bulk of the He I centroids are at rest with respect to the stellar photospheres; however, a few objects show centroid velocities redshifted by ≤ 17 km s^{-1} . In contrast, most of the He II centroid velocities are slightly redshifted, by ≤ 19 km s^{-1} . These kinematic properties are in accord with earlier findings for the *NC* in samples including our program stars as well as other CTTs (Boesgaard 1984; Appenzeller, Jankovics & Jetter 1986; Appenzeller, Reitermann & Stahl, 1988; Hamann & Persson 1992;

Batalha et al 1996), and are consistent with an origin in the post shock region in the magnetospheric accretion model.

The somewhat smaller widths observed in the weaker He I may result from lower opacities in these lines, which arise from higher levels and possess smaller transition probabilities than does λ5876. The redshift of the line centroid from the stellar velocity is consistent with line-of sight projection for the small infall velocity (ranging from $\sim$ 80 to 0 $\mathrm{km\,s^{-1}}$) of the post-shock region. The larger widths and more redshifted centroid velocities for the He II line suggest that it may originate in the earlier part of the post-shock region where temperatures, ionization fluxes, and gas velocities are higher.

The *NC* is variable; however, its kinematic properties at the different epochs are still consistent with a postshock region origin. Table 2 lists the variation observed in the *NC* in objects with multiple observations and shows that the FWHM is observed to change by as much as 21% from its value in the reference sample. The centroid velocity varies by as much as 13 $\mathrm{km\,s^{-1}}$ from its value in the reference sample; however, centroid velocities remain centered on the stellar photospheric velocity or moderately redshifted.

2.5. The λ5876 Broad Component

In this section the properties of the *BC* in λ5876 are established and it is argued that the *BC* emission is itself composite, including contributions from at least two independent regions. The kinematics of the *BC* are presented first and confronted with the predictions from an axisymmetric magnetosphere aligned with the stellar rotation axis. The redshifted emission properties are found to be consistent with a magnetospheric origin, while the blueshifted *BC* emission properties indicate that

a wind origin is likely. The data further suggest that the redshifted and blueshifted emission in the *BC* each bear a distinct relation to the *NC* emission region and that a source of veiling other than the accretion shock must exist in at least the CTTS with dominant *BC* emission but undetectable *NC* emission.

2.5.1. Evidence for a composite *BC*: Kinematics

Figure 9 shows the residual profiles in decreasing order of *BC*/*NC*, extracted according to the procedure in §3. The *BC* was detected in 22 of the 31 objects in the reference sample. For the majority, the formal uncertainties in the best fit FWHM and centroid velocities are ≤ 5 km s^{-1} . Comparing objects with indistinguishable profiles at different epochs yields estimated uncertainties that are $\sim$5 km s^{-1} for the centroid velocities, ≤ 10 km s^{-1} for the FWHM, and between 25 and 50 km s^{-1} for the wing velocities at zero intensity.

The residual *BC* exhibits a range of morphologies, in marked contrast to the *NC*. In addition to the variety of emission profiles, five of the objects in the sample, RW Aur, DR Tau, YY Ori, GM Aur and GK Tau, exhibit redshifted absorption at some epoch of observation, suggestive of high velocity infall. The AS 353A profile may also suffer from redshifted absorption. For these objects the measured FWHM, centroid velocity, red wing velocity and equivalent width are most likely underestimates of the unattenuated emission properties.

The emission *BC* displays FWHM between 128 km s^{-1} and 287 km s^{-1} . The centroid velocities are blueshifted ($\mu_{BC} < 5$ km s^{-1}) in 12/22 of the objects and redshifted ($\mu_{BC} > 5$ km s^{-1}) in 5/22 of the objects, with the maximum blueshift as high as -93 km s^{-1} and the maximum redshift as high as 35 km s^{-1} (cf. Fig 6). For the remainder (5/22), the centroid velocities are at rest with respect to the stellar photosphere. The blue wing velocities at zero intensity range from -175 km s^{-1} to

-900 $\mathrm{km\,s^{-1}}$, with average -313 $\pm$ 162 $\mathrm{km\,s^{-1}}$ (N = 22). The wing velocities are <= $-300\,\mathrm{km\,s^{-1}}$ for 11 of the 22 stars, with 10 of these displaying velocities between -300 and -500 $\mathrm{km\,s^{-1}}$. The velocities lie between -200 $\mathrm{km\,s^{-1}}$ and -300 $\mathrm{km\,s^{-1}}$ for 36% (8/22) of the objects and are -175 $\mathrm{km\,s^{-1}}$ for DD tau, DE Tau and YY Ori. The red wing velocities at zero intensity for the majority are fairly uniform, with average 216 $\pm$ 78 $\mathrm{km\,s^{-1}}$ (N = 22). Only 5 objects (CW Tau, DG Tau, DL Tau and DO Tau) possess red wing velocities in excess of 200 $\mathrm{km\,s^{-1}}$ at zero intensity.

Among objects with detectable *BC* emission, DG Tau exhibits direct spectroscopic evidence for the presence of a wind in He I. In addition to prominent emission centered on the photospheric velocity, the *BC* displays asymmetric wings with more blueshifted than redshifted emission. Although the red wing is cut off by P Cygni absorption in the nearby sodium D2 line, the blue wing extends to -900 $\mathrm{km\,s^{-1}}$. Comparing the He I λ5876 blue wing morphology with the simultaneously observed Hα line at two epochs different from the reference epoch suggests that a wind is present. Figure 10 shows the superposition of the observed profiles in He I λ5876 and Hα at the three epochs when this object was observed. At two epochs the He I λ5876 blue wing displays a blueshifted feature between -175 $\mathrm{km\,s^{-1}}$ and -350 $\mathrm{km\,s^{-1}}$. In the simultaneous Hα profiles a spectral feature is found at the same velocity and with a similar morphology, suggesting that blueshifted absorption may be responsible for both. The DG Tau spectrum in Alencar & Basri (2000) exhibits a spectral signature at $\sim$-230 $\mathrm{km\,s^{-1}}$ in He I λ5876 that appears similar to absorption features at $\sim$ -200 $\mathrm{km\,s^{-1}}$ in both the simultaneous Hα and Hβ profiles. If due to blueshifted absorption, then this is direct evidence of outflowing gas. Alternatively, the blueshifted features in both He I and Hα may be due to a separate emission component. Its centroid velocity in He I λ5876, which lies between -235 $\mathrm{km\,s^{-1}}$ and -275 $\mathrm{km\,s^{-1}}$ for our DG Tau spectra, would then place it at the base

of the jet observed in the forbidden lines of DG Tau (HEG). If the absorption interpretation is correct, however, the centroid velocity for the unattenuated *BC* emission in DG Tau will be blueshifted. Rough estimates of the centroid velocity in this case can be obtained by fitting a Gaussian function to the He I λ5876 profile that exclude the region between ~ -250 km s^{-1} and ~ 50 km s^{-1} , the latter limit to avoid the uncertainty associated with the extraction of the residual *BC* from the observed profile. For the epochs with $r_R = 2$ and $r_R = 3$, such fits yield $\mu_{BC} = -68$ km s^{-1} and $\mu_{BC} = -56$ km s^{-1} , respectively. For the $r_R = 3.6$ epoch, which is displayed in Figure 9 as part of the reference sample, this technique can not be applied. The centroid velocities for DG Tau in Figures 11a and 11b are as measured from the residual *BC* profile, but marked with an arrow indicating that a more a blueshifted value is probable.

For the ensemble of 22 objects, the presence of both blueshifted and redshifted centroid velocities as well as the blueshifted wing velocities provide constraints to the origin of the *BC* emission. In what follows, the feasibility of the magnetospheric accretion model for producing the He *BC* emission is assessed by comparing the model predictions with the *BC* centroid velocity μ_{BC} and the maximum blue wing velocity.

In the magnetospheric accretion model the flow is coupled to the field, so that the poloidal velocity is parallel to the field lines (Ghosh, Lamb & Pethick 1977). For a dipolar stellar magnetic field that is aligned with the stellar rotational axis and corotating at the stellar angular velocity Ω_*, it can be shown that the poloidal velocity v_p at a polar angle θ is given by

$$v_p^2 = \frac{2GM}{R_*} \sin^2\theta_o \left(\frac{1}{\sin^2\theta} - 1\right) - \frac{R_*^2\Omega_*^2}{\sin^4\theta_o}\left(1 - \sin^6\theta\right),$$

where θ_o is the polar angle of the field line at the stellar surface, and M_* and R_*

are the stellar mass and radius respectively. This value follows by calculating the work done on a test particle by the gravitational and centripetal forces acting along a path determined by a dipolar streamline. With

$$v_z = v_p \frac{\left(3\sin^2\theta - 2\right)}{\left(1 + 3\cos^2\theta\right)^{1/2}},$$

it can be seen that the root of v_z is at $\theta = \arcsin\sqrt{\frac{2}{3}}$, so that a particle falling along a field line onto the star will have a positive v_z when it is at polar angle $\theta > 54.7^o$ and negative v_z at $\theta < 54.7^o$.

Previous work on the expected hydrogen Balmer and other metallic line emission including line strengths and velocity profiles has been carried out for non-rotating magnetospheric accretion (e.g., see Calvet & Hartmann 1992; Hartmann, Hewett & Calvet 1994; Muzerolle, Calvet & Hartmann 1998; Muzerolle, Hartmann & Calvet 1998). However, no published work is extant on the expected emission from a rotating magnetosphere. Maximum poloidal, v_z and line-of-sight infall velocities with and without rotation are presented for a typical set of CTTS parameters and for a range of magnetospheric sizes in Table 3. A stellar mass of $M_* = 0.5M\odot$, stellar radius of $R_* = 2.0R\odot$ (HEG; Hartmann et al. 1998), $P_{rot} \sim 8.5$ days (Edwards et al 1993) and inner disk hole or magnetospheric size between $5R_*$ - $7R_*$ (Konigl 1991) are the currently accepted typical values for CTTS. For these parameters the free-fall velocity is $\sim$309 $\mathrm{km\,s^{-1}}$, the stellar angular velocity is $\Omega_* \sim 8.6\times10^{-6}$ $\mathrm{rad\,s^{-1}}$ and the stellar rotational velocity $R_*\Omega_* \sim 12\,\mathrm{km\,s^{-1}}$. Table 3 shows that for magnetosphere sizes R_B between $2R_*$ and $5R_*$ the centripetal term has little effect on the velocities. For $6R_*$, however, the stellar rotation truncates the observed v_z and poloidal velocities to about half their size without rotation for $\theta > 54.7$, and for larger sizes still, there is a range of polar angles for which the centripetal term is dominant. For instance, at $R_B = 6.5R_*$, $7R_*$ and $8R_*$, a particle

starting at polar angle greater than 72.0^o, 63.7^o and 53.3^o, respectively, has such a large rotational kinetic energy that no infall can occur.

The emission from an aligned rotating magnetosphere can be thought of as arising from axisymmetric rings of successively smaller radius as the polar angle decreases from its value at the disk plane $\theta = \pi/2$ to its value at the stellar latitude, θ_o, where the dipolar field lines intersect the stellar surface. For an axisymmetric ring of emitting particles, the line profile is symmetric about a centroid velocity of $-v_z \cos i$ where v_z is the velocity of a particle along the z (symmetry) axis, and i is the inclination angle of the line of sight from the z axis (Kwan & Tademaru 1995). Thus an axisymmetric ring of particles will produce emission to the blue if v_z is positive and emission to the red if v_z is negative.

He I emission in the funnel flow is likely to be produced by recombination and cascade. Given the high UV flux needed for ionization, He I emission at $\theta < 54.7^o$ probably dominates that at $\theta > 54.7^o$. We propose that the emission in the magnetospheric funnel flow at $\theta < 54.7^o$ is largely responsible for the *BC* when it has a redshifted centroid velocity (e.g. DF Tau, DO Tau, DD Tau, YY Ori, DS Tau). The same argument will preclude the magnetospheric funnel flow from being responsible for the *BC* when it has a blueshifted centroid, as we now show.

Table 3 lists the maximum blueshifted centroid velocity (columns 3 and 4) and the maximum poloidal velocity (columns 7 and 8) that occur at each magnetospheric size. Blueshifted centroid velocities diminish rapidly as the magnetosphere size increases and infall starts at greater distances from the gravitational potential. The effect is more pronounced when stellar rotation is taken into account, so that, with the above parameters, the centroid velocity that would result is $v_z \sim -21$ km s^{-1} or redward for magnetospheric sizes larger than $5R_*$. At $R_B = 2R_*$ rotation has little effect and the largest centroid velocity is ~ -45 km s^{-1} . Similarly, with the

above parameters, emission in the magnetosphere cannot produce wing velocities blueward of -309 $\mathrm{km\,s^{-1}}$ or ~ -275 $\mathrm{km\,s^{-1}}$ if rotation is included. This range of centroid velocities and wing velocities is not consistent with the observations. Figure 11a shows the blue wing velocities at zero intensity plotted against the centroid velocity μ_{BC} for every object with BC detectable emission (N = 22). For objects with multiple observations, the starred object name refers to the epoch included in the reference sample; the unmarked object names denote observations of these objects at other epochs. The maximum predicted magnetospheric centroid and wing velocities are marked in the figure with dashed lines. As can be seen from the figure, 18% of the stars display centroid velocities blueward of -45 $\mathrm{km\,s^{-1}}$ and 41% of the stars exhibit blue wing velocities more blueshifted than -309 $\mathrm{km\,s^{-1}}$. Further, at an average inclination angle of 60^o, the predicted centroid velocities $-v_z \cos i$ are a factor of 1/2 times those in columns 3 and 4 and the predicted maximum poloidal velocities $v_{LOS} = -v_R \sin i - v_z \cos i$, for the cylindrical radial velocity v_R and v_z components, are as listed in columns 10 and 11 of Table 3. Thus the discrepancy between the values predicted by the magnetosphere and those observed is likely to be more severe than suggested by Figure 11a.

Consideration of the redshifted absorption expected to arise from the funnel flow when viewed along lines of sight that intersect the accretion shock does not help the case for the magnetosphere. Although redshifted absorption naturally produces emission that is blueward-asymmetric, restoration of the redshifted absorption signature to an observed profile cannot affect the position of a peak that is blueshifted.

Finally, as mentioned above, the excitation conditions probably do not favor emission at $\theta > 54.7^o$, due to attenuation of the ionizing radiation by the intervening column. Recent calculations of the emerging spectrum from an attenuated postshock and optically thin preshock regions (Calvet & Gullbring 1998) indicate

that the extent of the preshock region is $\leq 1\%$ of the stellar radius. Therefore photoionization from the accretion shock alone is unlikely to be a source of excitation of magnetospheric column gas at $\theta > 54.7^o$. In the absence of a nearby photoionization source, therefore, the *BC* emission for objects with blueshifted centroid velocities $\mu_{BC} >$ -45 $\mathrm{km\,s^{-1}}$ and wing velocities redward of -309 $\mathrm{km\,s^{-1}}$ (CI Tau, DQ Tau and GK Tau, see Figure 11a), while not kinematically incompatible with a magnetosphere origin, is not likely to arise there.

We conclude that a second component, besides the funnel flow, is required to produce most of the He I emission in at least those stars with *BC* centroid velocity blueward of -45 $\mathrm{km\,s^{-1}}$, and is needed to produce at least part of the He I emission in the stars that display *BC* wing velocities blueward of -309 $\mathrm{km\,s^{-1}}$. The v_z needed to produce a large blueshifted centroid velocity if the emission possesses axial symmetry, together with the speed necessary to produce the broad line width, suggest a wind as the source of the *BC* emission in these cases. Disk occultation of the receding part of the outflow can produce the blueshift. These considerations are summarized in Figure 11a, where the labels "WD" for "wind-dominated" and "AD" for "accretion-dominated" are applied to the objects with $\mu_{BC} \leq -45$ $\mathrm{km\,s^{-1}}$ and objects with $\mu_{BC} \geq 5$ $\mathrm{km\,s^{-1}}$, respectively.

2.5.2. Evidence for a composite *BC*: Line Strengths

The arguments presented above for the case of an accretion component and a wind component for the *BC* have been based solely on the relation between a line profile and gas kinematics. In this subsection, we define the strength of the *BC* relative to the *NC* as the ratio of the *BC* and *NC* equivalent widths or *BC*/*NC*, and then examine the relationship of this index to the *BC* centroid velocity μ_{BC}. Estimates of the equivalent width for the wind and accretion contributions to the

BC are obtained and related to the NC equivalent width. Together, all three lines of research lend further support to the notion that the nature of the BC, when redshifted, differs from that when it is blueshifted.

Figure 11b shows BC/NC plotted against μ_{BC} for every object in the reference sample. For the three objects with undetectable NC emission, AS 353A, CW Tau and HN Tau, upper limits for the NC equivalent widths were estimated by fitting a double Gaussian to the observed profiles, with one of the components set to the mean NC FWHM and centroid velocity from the 31 objects in the sample. Dotted lines connect the BC/NC values for each star observed on more than one epoch. It can be seen from the figure that when the BC is redshifted the range in BC/NC is small, between $\sim$0.4 and $\sim$1. In contrast, when the BC is blueshifted the range in BC/NC is much larger, between $\sim$0.6 (BP Tau) and $\sim$ 38 (DG Tau). In addition, the blueshifted BC accounts for most of the cases where the BC is dominant; significantly redshifted (i.e, with $\mu_{BC} > 5 \mathrm{km\,s^{-1}}$) and dominant BC emission is not observed in our sample.

With the interpretation of the BC redshifted emission as originating from $\theta < 54.7^o$ in the magnetospheric funnel flow, and the NC as arising from the post-shock region of the same flow, the small range of BC/NC for the redshifted emission is understandable in terms of a likely relationship between the emission from the two regions. In contrast, the much larger range in BC/NC when the BC centroid velocity is blueshifted suggests that the mechanisms of formation for the NC and the BC in this case are different, as is probable if the blueshifted emission arises in a wind that may not have a strong relation with the magnetospheric accretion. In addition, it can be seen from Figure 11a and 11b that every object with a centroid velocity more blueshifted than -45 $\mathrm{km\,s^{-1}}$ and with blue wing velocity at zero intensity more blueshifted than -309 $\mathrm{km\,s^{-1}}$ also exhibits a $BC/NC > 1$. These

velocity limits were identified above as the maximum blueshifted centroid velocity and wing velocity that can be generated in a magnetosphere. **Therefore, if the wind hypothesis for the origin of the blueshifted *BC* emission is correct, the dominance of the *BC* in the observed profiles is due to the wind.**

There are two objects in Figure 11 that deviate from the trend established by the majority, HN Tau and DG Tau. In HN Tau the *NC* is undetectable yet it exhibits the broadest *BC* FWHM and a centroid at the stellar velocity. In the above interpretation these properties imply that the *BC* emission arises from a spherically symmetric wind and is observed nearly edge on to the disk. In DG Tau, discussed above, the centroid velocity of the emission is blueshifted if the absorption interpretation of the blueshifted features shown in Figure 10 is correct. This would bring it into closer agreement with the other objects with dominant *BC* emission.

The trends exhibited by the reference sample in Figure 11b, namely that the blueshifted emission displays a larger range of *BC*/*NC* than the redshifted emission and that the *BC* tends to be blueshifted when dominant, are also suggested by an examination of the *BC* in objects with multiple observations. The time coverage was erratic and intermittent, rendering conclusions from this set of observations as only suggestive. Figure 12 shows a superposition of the observed profiles for every star with multiple observations. Except for BP Tau, CI Tau and GM Aur, every other object exhibits measurable changes in the profile. For the latter, the figure shows that when the *BC* decreases relative to the *NC*, it is the blueshifted emission that decreases in most cases (the exceptions are DG Tau and DL Tau each at one epoch). In contrast, the redshifted emission appears to vary less with respect to the *NC*. The paucity of blueshifted emission as the *BC* contribution decreases means the centroid velocity of the remaining emission is less blueshifted, consistent with the findings of Figure 11b for the reference sample. In other words, when the *BC*

relative strength increases to become the dominant contribution, the change (with respect to the *NC*) is most often achieved by increasing the blueshifted, rather than the redshifted emission. This is true for every object with significant profile changes, whether redshifted absorption is present or not, and suggests that the blueshifted emission is more variable than the redshifted emission. However, that notion can be validated only by contiguous time coverage.

Further support for the notion of a composite *BC* can be obtained by comparing estimates of the line strength for the *BC* wind and accretion contributions to the *NC* line strength. If our interpretation is correct, then the accretion component and the *NC* should show signs of a related origin. Given that these components are not resolved, the procedure for estimating the wind and accretion component equivalent widths has been approximated in two ways. In the integration method, the equivalent width of *BC* residual profiles is measured blueward of -200 $\mathrm{km\,s^{-1}}$ and redward of 0 $\mathrm{km\,s^{-1}}$ as crude estimates of the wind and accretion contributions, respectively. The -200 $\mathrm{km\,s^{-1}}$ limit follows from the maximum extent of the blue wing for objects with redshifted centroid velocities (DD Tau, DF Tau, DO Tau, DS Tau and YY Ori), for which we have argued that the *BC* is dominated by the accretion component (cf. Figures 11a,b). The average blue wing velocity at zero intensity for these is 210 ± 52 $\mathrm{km\,s^{-1}}$. Taking this as a representative of the accretion component, its contribution in every other object can be minimized by using only the extreme blue wing. The second or 'wind-fit' method for estimating the strength of the wind contribution is based on the shape of the blueshifted wing in the profiles of objects that we believe to be dominated by the wind, namely AS 353A, CW Tau and HN Tau. Using the Gaussian parameters that best describe the blue wing in these objects, the strength of the wind contribution in every other object with detectable *BC* emission can be estimated by calculating the best fitting

amplitude and equivalent width of such a Gaussian, using only the profile blueward of -200 $\mathrm{km\,s^{-1}}$ to constrain the fit. The accretion contribution follows by taking the difference of the latter estimate from the total *BC* equivalent width. For this purpose, the broad profile average presented in the uppermost left panel of Figure 5 including AS 353A, CW Tau and HN Tau was used as representative of the wind-dominated objects. In fact, the average profile that results is indistinguishable from that in Figure 5 if the UY Aur and DG Tau *BC* residual profiles, also believed to be dominated by the wind as argued above (cf. Figs 11a,b) are included in the average. The Gaussian parameters for the wind average profile have centroid velocity $\sim -56 \pm 4$ $\mathrm{km\,s^{-1}}$ and FWHM $\sim 272 \pm 4$ $\mathrm{km\,s^{-1}}$, by fitting it from -400 $\mathrm{km\,s^{-1}}$ to 100 $\mathrm{km\,s^{-1}}$.

Figure 13 shows the *NC* equivalent width plotted against the resulting estimates of the wind and the accretion line strengths, with the equivalent widths from the 'integration' method plotted in the upper panels and those obtained from the 'wind-fit' method plotted in the lower panels. It can be seen from the figure that both methods yield similar values for the equivalent width of each component. The most important result, however, is that the *NC* is distinctly related to the wind and to the accretion components. The *NC* equivalent widths tend to increase as the accretion component equivalent width increases. The suggested correlation of the *NC* line strength with the estimate of the *BC* accretion component provides support for the interpretation of the redshifted *BC* as emission from the funnel flow gas just before it reaches the accretion shock and emits as the *NC*. In contrast, although the number of objects with a measurable wind contribution (as defined above) is small, the *NC* equivalent widths decrease as the equivalent width of the wind component increases. Extreme examples are found in the objects AS 353A, CW Tau, and HN Tau, which have undetectable *NC* emission in λ5876 and in λ6678.

Non-simultaneous observations of these objects in the blue He I and He II lines indicate that when detectable, the emission is dominated by the *BC*. Although the λ4472 line is blended by Ti II at ~ -250 km s^{-1} , it is clearly dominated by the *BC* in the observed profiles of AS 353A, CW Tau and DG Tau. None of these objects has detectable emission in the He I λ4713 and He II λ4686 lines, which are otherwise dominated by the *NC* in the other objects observed in the blue.

The disappearance of the *NC* emission in these objects at least means that either the *NC* emission region is occulted by an increasingly stronger and more blueshifted *BC* emission region or that a redistribution of the accretion flow occurs in the wind dominated objects to favor the wind at the expense of the *NC*. For the *BC* to effectively occult the *NC*, it would have to be very optically thick at the photospheric velocities that characterize the *NC* centroid velocity. This is not likely to be the case for the wind component, but is likely for the redshifted *BC* identified as arising from the funnel flow. However, this component would have to be very spatially extended to completely cover the *NC* emission region. Moreover, the objects with redshifted *BC* emission are precisely those with the strongest *NC* emission among all the objects with detectable *BC*. The considerations suggest that the *NC* becomes intrinsically weaker as the *BC* emission grows, and, if the wind hypothesis is correct, becomes increasingly wind dominated. In any case, it is clear that more than one source of excess continuum emission must exist in at least those objects with undetectable *NC* emission. Independent sources of veiling emission in CTTS could account for the absence of a correlation between *BC*/*NC* and the veiling found in this study and between the NC equivalent widths and the veiling continuum emission, observed in this and other studies of CTTS (Johns-Krull & Basri 1997).

Summarizing, the *BC* kinematics and the likely conditions for its formation differ according to its centroid velocity. When redshifted, the *BC* is consistent with an origin in the funnel flow close to the accretion shock and its strength is comparable to or weaker than the *NC*. In contrast, it has been shown that when blueshifted, the *BC* kinematics in 41% of the stars with such emission are incompatible with a magnetospheric origin but consistent with a wind, and that the *BC* emission in every object that is thus excluded from arising in a magnetosphere also exhibits dominant *BC* emission, with $BC/NC > 1$. One of the objects in our sample, DG Tau, exhibits direct spectroscopic evidence for a wind in He I λ5876. The blueshifted *BC* relative strength ranges from dominant to weaker than the *NC*, suggesting that a variety of physical conditions are responsible for its emission. The *BC* in individual objects with multiple epoch observations is also blueshifted when dominant and the blueshifted *BC* exhibits a larger range of strengths relative to the *NC* than the redshifted emission. Together, these facts suggest that when it is the main contribution to an observed profile, the He I λ5876 *BC* is dominated by the wind. Significantly redshifted *BC* emission that is dominant in a profile is not observed in this study. Finally, the *NC* equivalent width decreases with estimates of the blueshifted emission that we have argued arises from the wind. This suggests that the processes that create the *NC* emission and the blueshifted emission in the *BC* are competitive in nature. Since *BC* is usually blueshifted when strong with respect to the *NC*, and probably wind-dominated, occultation of the *NC* by the *BC* as it becomes stronger and more blueshifted is not likely. For the three objects with *BC* emission only, a source of veiling continuum emission other than the accretion shock would seem to be required to account for the observed veiling emission but undetectable *NC* emission.

2.6. The λ6678 *BC*

In this section the *BC* emission in the λ6678 line is discussed. The λ5876 and λ6678 lines were simultaneously observed, allowing comparisons in kinematics and line strengths to extract further clues about the nature of the *BC*. The λ6678 profiles differ from those of λ5876, suggesting that differences in excitation conditions are responsible and supporting the notion of a composite BC in He I . The λ6678 *BC* was detected in thirteen of the objects in the reference sample. Estimated uncertainties are ≤ 10 km s^{-1} in the FWHM and ≤ 5 km s^{-1} in the centroid velocities for most objects. For GG Tau and CI Tau, however, these are probably as high as $\sim$50 km s^{-1} in the FWHM and ~ 20 km s^{-1} in the centroid velocities.

Figure 14 shows a superposition of the observed profiles in λ5876 and λ6678 arranged in decreasing order of the λ5876 *BC*/*NC*, from which an object-by-object comparison may be carried out. The figure shows that the observed profiles differ for the majority of objects with detections in both transitions, and are similar only in RW Aur, DD Tau and DF Tau. Where they differ, it is generally in the larger wing velocity for the blueshifted emission in λ5876 as in CW Tau and AS353A, or in the larger strength of the blueshifted emission relative to the *NC* in λ5876, as in DG Tau, DL Tau, DR Tau, GG Tau, UY Aur and CI Tau. Most of the profiles are similar in the red wing velocities and in the strength of the redshifted emission relative to the *NC*. The exceptions are AS 353A, for which the red wing is more extended in λ6678 than in λ5876, and GG Tau, DL Tau and DO Tau, for which the redshifted emission is weaker relative to the *NC* in in λ6678 than in λ5876.

Gaussian parameters for the λ6678 *BC* yield FWHM that range from 132 km s^{-1} to 284 km s^{-1} . Centroid velocities are between -74 km s^{-1} and +40 km s^{-1} , with blueshifts in 46% (6/13) of the stars, redshifts in 31% (4/13) of the stars and

velocities centered on the stellar photosphere for the remainder. Therefore, while both blueshifted and redshifted centroid velocities are observed for λ6678, the former are less blueshifted than in λ5876. The blueshifted centroid velocities and blue wing velocities at zero intensity in λ6678 are plotted against one another in Figure 15a. Object names marked with asterisks denote the epoch included in the reference sample; the unmarked object names denote observations of these objects at other epochs. For λ6678, only the objects RW Aur and UY Aur exhibit blueshifted centroid velocities close to or blueward of -45 $\mathrm{km\,s^{-1}}$; the rest have centroids between -10 $\mathrm{km\,s^{-1}}$ and -40 $\mathrm{km\,s^{-1}}$. Red and blue wing velocities at zero intensity are similar in λ6678, with mean values of 233 $\pm$ 68 $\mathrm{km\,s^{-1}}$ (N = 13) for the red wing velocities and -261 $\pm$ 96 $\mathrm{km\,s^{-1}}$ for the blue wing velocities (N = 13). For comparison, the λ5876 counterparts have values of 216 $\pm$ 78 (N = 22) $\mathrm{km\,s^{-1}}$ for the red wing velocities and -313 $\pm$ 162 (N = 22) for the blue wing velocities. Although average blue wing velocities are similar for the two transitions within the dispersion of the mean, a comparison of Figures 15a and 11a shows the blue wing velocities are smaller in λ6678 than in λ5876 for the majority of objects.

If the hypothesis of the wind origin for the blueshifted *BC* emission in λ5876 is correct, then the incidence of smaller blueshifted *BC* emission relative to the *NC* in 6/13 observed λ6678 profiles and the less extended blue wing velocities in 3/13 residual *BC* λ6678 profiles suggests that the wind component conditions are not as favorable to emission in λ6678. In contrast, the similar redshifted *BC* emission relative to the *NC* in 8/13 observed profiles and the comparable red wing velocities for 11/13 *BC* residual profiles in both transitions suggests that the infall component identified with the redshifted *BC* emission in λ5876 appears to be equally hospitable to emission from both transitions.

Examination of the behavior of the BC/NC index against the BC centroid velocity μ_{BC} yields the same general conclusions for λ6678 as it did for λ5876. However, from the above considerations one would expect that the BC/NC to BC centroid velocity relation will differ in detail from its counterpart in λ5876. Figure 15b shows the λ6678 BC/NC plotted against μ_{BC} for the 13 objects in the reference sample with detectable BC emission. Multiple observations of individual objects are joined by dotted lines. As for λ5876, objects with the largest BC/NC also display blueshifted or centered emission. However, unlike λ5876, significantly redshifted emission in λ6678 is observed with a range in BC/NC between 0.45 and 2.2. Including DG Tau at the $r_R = 2$ epoch, which has a centroid velocity of 11 $\mathrm{km\,s^{-1}}$, the BC/NC range for the redshifted BC extends to ~ 15. Nevertheless, aside from DG Tau, the λ6678 blueshifted BC emission exhibits larger BC/NC values and a larger BC/NC range than the most redshifted emission, as is the case for λ5876.

Figure 16 shows a superposition of profiles for these objects with multiple epoch observations that are included in Figure 15. These indicate that as BC/NC decreases in the individual objects, the amplitude of the blueshifted emission with respect to the NC decreases while the redshifted emission varies less or is indistinguishable at the various epochs. This is consistent with the multiple epoch findings for λ5876 and supports the notion that a larger range of physical conditions prevails for the blueshifted emission than for the redshifted emission in individual objects as well as in the reference sample. Therefore, the data support an interpretation for the λ6678 blueshifted BC emission as arising, at least partly, in the same wind component that gives rise to the blueshifted λ5876 BC emission. The similarity in the BC redshifted signatures for both lines suggests that the λ6678 emission also originates in the funnel flow for $\theta < 54.7°$. However, since BC/NC for the λ6678

redshifted emission spans a larger range and has a larger maximum value, than in λ5876, where $BC/NC_{red} \leq 1$, this suggests that the infall component favors emission in λ6678.

A comparison between the λ6678 and λ5876 profiles for the object DL Tau at the four epochs when it was observed supports the proposal that the λ6678 BC emission is favored by the accretion component. Figure 17 shows λ5876 in the left panels and λ6678 in the right panels, with best fits superposed on the observed profiles. The individual panels are labeled by the value of BC/NC, denoted by f due to restrictions of space. The figure shows that BC/NC for λ5876 decreased from $BC/NC \sim 9$ in the topmost profile to $BC/NC \sim 2$ at the bottom. The λ6678 BC/NC also decreased at the same epochs, and in addition, its centroid velocity μ_{BC} changed from centered on the stellar photospheric velocity to redshifted in the lower two panels. However, the λ6678 profiles in the last two rows changed little, in contrast to the noticeable decrease in the BC/NC displayed by the λ5876 profile. It was argued in §4 that when the BC dominates the λ5876 profiles, it is due to a wind contribution. With the available multiple epoch data, it has been shown that as BC/NC decreases, it is predominantly due to a decrease in the BC blueshifted component for both λ5876 and λ6678. Therefore a consistent interpretation of the profile changes in DL Tau is that when the wind contribution decreased in λ5876, the BC blueshifted emission in λ6678 could also decrease until the conditions in the wind were no longer favorable to emission in λ6678 (i.e., at the epoch with BC/NC = 4.6 in λ5876). Beyond this point, further decreases in the wind component in λ5876 could have no effect on the λ6678 emission, which must have originated primarily from a different region. This is suggested by the transition in the λ6678 BC centroid velocity from blueshifted to redshifted and the near insensitivity of its profile to the change exhibited by the λ5876 profile at the same epoch.

In summary, the *BC* emission from λ5876 and λ6678 show comparable gross properties. However, the difference in the velocity structure between λ6678 and λ5876 suggests strongly that the BC does not arise from a single region as might be expected if both lines originated from the funnel flow. The blueshifted component that tends to dominate the *BC* emission in both lines appears to be less favorable to emission in λ6678 in most cases, leading to a (comparative) deficit of λ6678 emission at the most blueshifted velocities. In contrast, the accretion component emission identified with redshifted centroid velocities in λ5876 seems to favor λ6678, so that comparable emission from both lines is observed at every redshifted velocity. If the blueshifted He I *BC* arises predominantly from a region with a large velocity range where the density decreases with increasing velocity, a deficit of singlet emission may result at the highest velocities, as observed. In contrast, if the emission with redshifted centroid velocities arises from a higher density region, both lines would be expected to have detectable contributions at every velocity, as observed. A rigorous test of this hypothesis must await detailed statistical equilibrium calculations of the line intensities. However, further insight into the nature of the *NC* and *BC* regions can be obtained by comparing the He I intensities to their values expected under conditions of nebular recombination, as is done in the following section.

2.7. Intensity Ratios

The helium optical emission spectrum can most easily be excited under conditions favorable to ionization followed by recombination and cascade. Level populations for pure recombination and cascade in the limit of very low electron densities ($10^2 \leq N_e \leq 10^6$ cm^{-3}) have been calculated by Brocklehurst (1972) and more recently, by Smits (1996). The calculations predict intensity ratios of $I_{\lambda5876}/I_{\lambda6678} = 3.5$ and

$I_{\lambda 4472}/I_{\lambda 4713} = 9.8$. Calculations that include the effects of intensity enhancement due to collisional excitation of the λ5876 and λ6678 upper levels from the metastable 2^3S and 2^1S levels (see §2.1) for $10^2 \leq N_e \leq 10^6$ cm^{-3} were carried out by Smits (1991). The results for the intensity ratios are insensitive to the electron density range considered and deviate from the pure recombination ratios only at $T_e = 20 \times 10^3$ K. Specifically, the $I_{\lambda 5876}/I_{\lambda 6678}$ ratio is raised to 5.1.

The results presented in this section are for simultaneously observed transitions. In the absence of flux calibrated spectra, we use the measured equivalent widths as proxy. It is assumed without proof that the veiling plus stellar continuum can be approximated by a 10^4 K blackbody, for which the difference in the continuum emission at 5876 Å and 6678 Å is $\sim 6\%$ and is even smaller among λ4472 Å, λ4713 Å and λ4686 Å. Therefore no corrections are applied to the ratios of equivalent widths. Formal errors of estimation for the *NC* and *BC* parameters yield uncertainties in the *NC* and *BC* equivalent widths that are smaller than the errors of measurement of the observed equivalent width. In addition, since errors of measurement in λ6678 and λ4713 are larger than in the stronger lines λ5876 and λ4471, uncertainties in the ratios are ultimately dominated by errors of measurement for the weaker lines. Figure 18 shows the *NC* and *BC* ratios for the λ5876 and λ6678 line pair displayed against the λ5876 *BC*/*NC* index for every object with detectable emission in at least one component in both lines. Objects included in the reference sample are marked with an asterisk. Tables 4 and 5 list the equivalent widths and their ratios for the red and blue lines, respectively.

2.7.1. The *NC*

The intensities for simultaneously observed transitions can be compared at the reference sample in 27 objects for the $\lambda\lambda$5876,6678 pair, in 12 objects for

$\lambda\lambda$4472,4713 pair and in 11 objects for the He I λ4472, He II λ4686 pair. For average values of the ratios, the error quoted is the dispersion of the mean.

As can be seen from the lower panel of Figure 18, the results for the *NC* $\lambda\lambda$5876,6678 pair show ratios that lie below the theoretical nebular recombination value in the great majority of objects. The values are insensitive to the system veiling. They range from $\sim$1 to $\sim$3 with an average value for the reference sample of $I_{\lambda5876}/I_{\lambda6678} = 2.0\pm$ 0.6 (N = 24). Of the objects with *NC* ratios compatible with the theoretical nebular recombination value the majority are subject to errors of measurement greater than 10% in both λ5876 and λ6678. That the *NC* ratios are smaller than the nebular recombination value suggests to us that the He I λ5876 line is becoming optically thick. Further, the nearly uniform distribution of *NC* ratios suggests that a fairly uniform range of physical conditions prevail in the *NC* emission region.

For the blue He I triplet pair, λ4472,λ4713, the uncertainties are larger than for the λ5876,6678 pair. About half of the objects (5/12) have ratios consistent with the theoretical nebular recombination value while the remainder are below it. The mean value for the *NC* λ4472,λ4713 ratios is 6.0 $\pm$ 3.4 (N = 11). For the He I λ4472 and He II λ4686 pair the observed *NC* ratios have a mean value of 1.7 $\pm$ 1.1 (N = 11). The nebular recombination value for this ratio is $I_{\lambda4472}/I_{\lambda4686} = 0.04(N_{He^+}/N_{He^{++}})$ (Osterbrock, 1974). Assuming that the lines are due purely to recombination and cascade, a range of $N_{He^+}/N_{He^{++}}$ between 19 (DR Tau) and 104 (UY Aur) would bring the theoretical ratios into agreement with the observed ones.

2.7.2. The *BC*

The *BC* intensities in the reference sample can be compared for the λ5876,λ6678 pair in 13 objects. The upper panel of Figure 18 shows that the *BC* ratios range

nearly over a factor of 7, suggesting that a variety of physical conditions may give rise to the *BC* emission.

Ratios for objects with multiple observations provide suggestive evidence of how variations in the *BC/NC* index affects the ratios. These show that variation in *BC/NC* can occur without concomitant changes in the strengths of the lines, as in UY Aur, GG Tau and one epoch in DG Tau. They also show that for some objects, the *BC* ratio is higher when *BC/NC* is lower in λ5876 and λ6678, as in DR Tau, RW Aur and two epochs in DG Tau. It was shown in §4 and §5 that as *BC/NC* decreases in objects with multiple observations, it is predominantly due to a decrease in the blueshifted *BC* emission relative to the *NC*. Therefore the larger ratios for smaller *BC/NC* observed in DR Tau, RW Aur and DG Tau are predominantly due to a deficit of blueshifted emission in λ6678 relative to λ5876. For DG Tau at the epoch with the largest ratio ($r_R = 2$), the blueshifted emission in λ6678 became undetectable at velocities blueward of -150 $\mathrm{km\,s^{-1}}$. In contrast the λ5876 line at the same epoch showed detectable emission extending to velocities of -500 $\mathrm{km\,s^{-1}}$ (See Figures 12 and 16). Although the multiple epoch observations do not by any means constitute an adequate sample, these results support the notion advanced at the end of the previous section, that the wind component is less dense than the infall component and that a decreased wind contribution can sustain λ5876 emission better than it can λ6678 emission.

Finally, the ratios for the object DL Tau (discussed in the previous section), illustrate what happens to the line strengths when the blueshifted emission component no longer dominates the profiles and the *BC* emission from the redshifted component is comparable to the blueshifted component. As the λ5876 *BC/NC* decreased from $\sim$9 to $\sim$5, comprising 3 of the 4 epochs of observation, the ratios showed no change (these epochs correspond to the top three panels of Figure 17). However,

as BC/NC decreased in λ5876 from $\sim$5 to 2, and in λ6678 from 2 to $\sim$1, the ratio decreased by a factor of 1.8 (these epochs corresponding to the bottom two panels of Figure 17). At the latter epoch the observed profiles of λ5876 and λ6678 are no longer BC dominated and are indistinguishable, as shown in the bottom-most panels of Figure 17. As can be seen in the Figure, at the epoch with lowest BC/NC in both lines the blueshifted emission (relative to the NC) decreased to its lowest observed level in λ5876 and the λ6678 profile became insensitive to the change in λ5876. The fact that the BC ratio is lowest at this epoch is consistent with the hypothesis that the blueshifted emission arises in a wind that is less dense than the infall region associated with the infall component. Within this hypothesis, when the wind contribution ceases to dominate the emission the infall component provides more nearly similar emission in both transitions, moving the ratio closer to unity.

2.8. Discussion

An important result of this work is that the He I BC emission is composite, including the contributions from a wind component and an accretion component. That a wind component should have been found in He I is not surprising given the prevalence of winds in permitted and forbidden transitions in these objects. Published He I λ5876 spectra for objects in our sample that have been included in previous studies (Hamann & Persson 1992; Batalha et al. 1996; Muzerolle et al. 1998; Alencar & Basri 2000) reveal that despite the extreme variability for which CTTS are known, the properties of the He I λ5876 BC emission found by other investigators is similar to those established by this study. The published data support the relation between the BC centroid velocity and the relative strength of the BC

(cf. Fig 11), and the trend of larger *BC* variability in the blueshifted emission than in the redshifted emission shown by our multiple epoch observations of individual objects (cf. Fig 12). Of particular interest are the published profiles of the objects CW Tau and AS 353A, which in this study show wind-dominated signatures in the one epoch of observation available. In published work, CW Tau exhibits *BC* dominated profiles and shows variations in its *BC* centroid velocity, from -150 $\mathrm{km\,s^{-1}}$ (Muzerolle et al. 1998), to -87 $\mathrm{km\,s^{-1}}$ (this study), to -58 $\mathrm{km\,s^{-1}}$ (Alencar & Basri 2000), all consistent with wind-dominated conditions. Similarly, AS 353A shows *BC* dominated profiles with blueshifted centroid velocities (Hamman & Persson 1992; Alencar & Basri 2000), suggesting that the dominance of wind-dominated emission is not a transient phenomenon in these objects. The object for which there is a significant difference between ours and published spectra is the spectroscopic binary DQ Tau (Basri et al. 1997), for which the λ5876 profiles have been observed to be blueward or redward asymmetric, depending on orbital phase of the binary.

Given the identification of a wind origin for the bulk of the He I λ5876 blueshifted *BC* emission, it is timely to investigate whether it shows any relation to the [OI] jet emission observed in CTTS (See Figure 5 of HEG). Among the 31 CTTS, N = 13 display [OI] emission with a separate blueshifted peak, N = 4 exhibit blueward asymmetry and blueshifted centroid velocities, N = 9 exhibit blueward asymmetry and centroid velocities centered near zero $\mathrm{km\,s^{-1}}$, and N = 5 exhibit profiles with symmetric profiles centered near zero $\mathrm{km\,s^{-1}}$, or redshifted asymmetric profiles. Of the 13 stars with a separate blueshifted peak in the [OI] emission, 10 possess He I $BC/NC > 1$ (AS 353A, CI Tau, CW Tau, DG Tau, DL Tau, DR Tau, GG Tau, RW Aur, DE Tau & UZ Tau E), including all but one star with the most prominent and blueshifted peaks in [OI]. The latter group includes 8 stars with blueshifted He I *BC* centroid velocities and 2 stars with He I *BC* centroid velocities near zero

$km\,s^{-1}$ (DE Tau & UZ Tau E). The 3 other stars with a separate blueshifted peak in the [OI] emission are DF Tau and DO Tau, with redshifted He I *BC* centroid velocities and $BC/NC < 1$, and DK Tau, with undetectable He I *BC* emission. Among the stars with no separate blueshifted [OI] peak, 4 have He I $BC/NC > 1$ (HN Tau, UY Aur, DQ Tau, & GM Aur), 6 have He I $BC/NC \lesssim 1$ (AA Tau, BP Tau, DD Tau, DS Tau, GK Tau, & YY Ori), and 8 have no detectable emission in the *BC* (CY Tau, DN Tau, FM Tau, FP Tau, GI Tau, HK Tau, LK Ca8 & V836 Tau). In summary, the majority of stars with dominant *BC* emission in He I also possess jet emission in [OI] while the majority of stars with weak or undetectable *BC* emission in He I show no sign of [OI] jet emission. However, the association of strong [OI] jet emission with no detectable wind emission in He I and of strong He I wind emission with no obvious jet signatures suggests that the winds probably originate from different regions.

While a wind has been invoked to explain the kinematics of He I emission in the objects DQ Tau (Basri et al. 1997) and CW Tau (Muzerolle et al. 1998), a significant wind contribution in the blueshifted He I λ5876 *BC* emission for at least 14 of the 31 objects in this sample suggests that a He I wind is common in CTTS. Since He I requires high temperatures or large ionization fluxes for its excitation, this emission can only originate in the most energetic of CTTS environments, and is very likely a direct probe of the accretion energy, whether it is dissipated at the stellar surface or close to the star/accretion disk interface. Calculation of the wind luminosity, including the UV resonance lines, would yield a lower bound to the energy required to generate it.

The wind interpretation for the blueshifted emission in He I λ5876 predicts P Cygni or blueshifted absorption signatures in transitions where the line optical depth is expected to be substantial, such as the λ10830 line which arises from the

metastable 2^3S level and the ultraviolet resonance lines 1^1S-n^{1}P λ584, λ537, etc. In a study of non-simultaneously observed λ5876 and λ10830 for 8 CTTS, Ulrich & Wood (1981) found that λ10830 emission is observable when λ5876 emission is present; however, only for the CTTS T Tau was there blueshifted absorption in λ10830, centered at -160 km s^{-1} . For two of their stars that overlap with our sample, the observed equivalent widths are comparable between the two lines, with $I_{10830}/I_{5876} \sim 1$ for DF Tau and $I_{10830}/I_{5876} \sim 1.2$ for RW Aur. While their measurements refer to the total observed profile, the published λ5876 profiles are very similar to ours. For DF Tau, the λ10830 line is broader than the λ5876 line by a factor of $\sim$3.8, with a λ10830 FWHM of 170 km s^{-1} and a centroid velocity of -10 km s^{-1} . For comparison, the centroid velocity for the λ5876 profile in DF Tau is +15 km s^{-1} . For RW Aur the λ10830 line is also broader than the λ5876 line by a factor of 1.6, with a λ10830 FWHM of 410 km s^{-1} . The centroid velocity is -225 km s^{-1} , which if real, as the authors believe, indicates a wind origin for this line. The RW Aur centroid velocity for the λ5876 line is +15 km s^{-1} . The authors attribute the large difference in centroid velocity between λ5876 and λ10830 to time variability or to a difference in the formation processes for the two lines. These observations are consistent with the kinematic characterization for the λ5876 found in this work, where the He I *BC* emission appears dominated by the accretion component in DF Tau and has a significant contribution from the wind component in RW Aur.

A second important result of this investigation is that the *NC* decreases as the strength of the *BC* wind component increases and suggests that formation of strong and predominantly blueshifted *BC* emission interferes with the formation of the *NC* emission region. As mentioned above, blueshifted emission at photospheric velocities is not likely to be very optically thick. However, the spatial relation of

narrow and broad component emission in CTTS has been discussed by Hamann & Persson (1992) for the Ca II infrared triplet λ8498, λ8542 and λ8662. These lines were found to be optically thick in all their sources except YY Ori. From chomospheric models, the authors place a lower bound to the column density required to achieve an optical depth of unity in the weakest triplet line λ8494 Å, which is of order $N_{H+HII} \approx 10^{21}(V_{Turb}/50 \text{ kms}^{-1})$ cm^{-2}, where V_{turb} depends on the source of broadening of the profile and can range from $\sim$10 km s^{-1} to $\sim$50 km s^{-1} . Based on the absence of detectable narrow components in the Ca II lines, the deep blueshifted absorptions in Ca II K, Hβ and Hγ in AS 353A and estimates of the size of the Ca II *BC* emission region for AS 353A and DG Tau, the authors concluded that the Ca II *BC* emission region could occult the star and its close environment in these two objects. For the remainder of their sample, the authors concluded that the narrow and broad component regions forming these lines lie adjacent, rather than on top, of one another. These results would be applicable to the He I lines only if the derived Ca II *BC* column densities imply an optical depth of unity or larger in He I . With the possible exception of DG Tau, none of the objects in our sample exhibit blueshifted absorption in the He I λ5876 *BC*, suggesting that its opacity is not very large. Then the disappearance of the *NC* emission may signal a redistribution of the accretion flow to favor of the wind at the expense of the infall component. In either case, the undetectability of the *NC* in *BC* dominated objects implies that more than one source of excess continuum emission or veiling is required in at least these stars. Independent sources of veiling in CTTS could account for the lack of correlation between the *NC* line strengths and veiling found in this work and in a study of DF Tau by Johns-Krull & Basri (1997). If the stellar magnetosphere is crushed against the star by the disk, the accretion shock producing the *NC* emission would be deactivated and a boundary

layer would form, producing excess continuum emission and the wind, as originally postulated by Lynden-Bell & Pringle (1974).

Recent work on the spectral energy distribution of the expected continuum emission emanating from the accretion shock (Calvet & Gullbring 1998) suggests that in fact, a source of continuum veiling other than the accretion shock is required to account for the observations in a set of 15 CTTS that overlap with stars in our sample. When confronting their model calculations with observations, the authors found that approximately half of their program stars exhibit Balmer jumps in excess of the maximum predicted amount by their grid of models and conclude that an additional source of Balmer continuum emission, not included in their model, must be present in these objects.

2.9. Summary

In this chapter the He I and He II optical emission in a sample of 31 CTTS and 10 WTTS has been analyzed, with the aim of elucidating the kinematic and physical properties of the emission regions producing the lines. The sample represents a range of two orders of magnitude in the mass accretion rate. The data is comprised of a series of high resolution echelle spectra over two discontinuous and non-simultaneous spectral ranges, $\approx \lambda\lambda$5000-6700 Å, including the red He I λ5876 and λ6678 lines and $\approx \lambda\lambda$4000-4920 Å, including the blue He I λ4472, λ4713 and the He II λ4686 lines. Of the 31 objects, 16 were repeatedly observed, over 2-5 epochs. Since the profiles are variable, the principal criterion used to select the epoch for inclusion in the sample representing the entire range of inferred mass accretion rates was to maximize the FWHM of the strongest line, λ5876 in the red and λ4472 in the blue. For this sample, our findings follow.

1) The He I profiles can be classified into broad, composite and narrow. Gaussian fits for the composite profiles yield parameters for the line core that are consistent for all the objects in the sample and are indistinguishable from those for the narrow profiles. The resulting narrow component or *NC* has average widths between 32 ± 9 and 47 ± 9 km s^{-1} for He I and 55 ± 10 km s^{-1} for He II. The He I *NC* centroid velocities are centered on the stellar photosphere for the majority of objects or moderately redshifted with velocities ≤ 35 km s^{-1} . The He II *NC* centroids are redshifted for the majority of objects, with velocities ≤ 20 km s^{-1} . These properties are consistent with origin in the post shock region close to the stellar photosphere postulated in the magnetospheric accretion model.

2) The *NC* were subtracted from the composite profiles to examine the residual profiles, which exhibit comparable kinematics to the broad profiles and are analyzed together as the Broad Component, or *BC*. For He I λ5876 the *BC* parameters present full widths between 128 and 287 km s^{-1} . Centroid velocities are most often blueshifted (12/22), but also redshifted (5/22) and centered on the stellar photosphere (5/22), with the largest blueshift and redshift observed to be $\geq$ -93 km s^{-1} and ~ 35 km s^{-1} , respectively.

3) Comparison of the observed kinematics of the *BC* with those expected from an axisymmetric, rotating magnetosphere argue against such an origin for all of the *BC*. Instead we find that the kinematics properties in 18 % of the stars with detectable *BC* emission are excluded as arising from the magnetosphere on the basis of their centroid velocity ($\mu_{BC} < -45$ km s^{-1}), and that 41% of the stars with detectable *BC* emission are excluded on the basis of their blue wing velocity (< -309 km s^{-1}). Emission in these cases at least is best accounted for by a wind. In contrast, the redshifted *BC* is compatible with origin in a magnetospheric funnel flow close to the accretion shock.

4) The BC strength relative to the NC or BC/NC, exhibits a range between $\sim$0.6 and $\sim$38 when the BC centroid velocity is blueshifted, and a smaller range, between $\sim$0.4 and $\sim$1, when the BC centroid velocity is redshifted. The BC emission in objects with multiple observations show that when the BC relative contribution decreases, it does so predominantly in the blueshifted emission while the redshifted emission varies less or is indistinguishable at the various epochs. In addition, objects with BC kinematics incompatible with a magnetosphere, i.e., with centroid velocity blueward of -45 $\mathrm{km\,s^{-1}}$ and with blue wing velocity at zero intensity blueward of -309 $\mathrm{km\,s^{-1}}$, also possess $BC/NC > 1$, suggesting that the dominance of the BC in the observed profiles is due to the wind.

5) The NC equivalent widths decrease as estimates of the wind line strength increases and increase as estimates of the accretion component increases. In addition, the NC equivalent widths are undetectable in wind dominated objects. These findings suggest that the wind dominated BC emission interferes with the formation of the NC and that the NC emission and accretion BC emission are physically related. Whatever the cause for the decrease of the NC, a source of veiling continuum emission other than the accretion shock must exist in at least those objects with dominant BC and undetectable NC emission. Independent sources of veiling emission could account for the lack of correlation between the NC line strengths and the observed veiling found in this and previous studies.

6) Analysis of the BC emission in λ6678 lines supports the conclusions reached from analysis of λ5876 and suggests that BC emission from λ6678 is favored in the infall component.

7) Ratios of equivalent widths for the NC and the BC in λ5876 and λ6678 display distinct distributions, with the bulk of NC ratios lying below the nebular recombination value while the BC ratios present a large dispersion. These facts

suggest that the range of physical conditions characterizing the BC emission is larger than that for the NC. The distribution of ratios against BC/NC for objects with multiple epoch observations further suggest that the wind component favors λ5876 emission over λ6678 emission.

The severe excitation conditions required by He restrict its origin to the inner disk/star region, where the accretion energy can be tapped to power the wind. Such emission is not surprising in these systems, which possess spatially resolved collimated jets in forbidden and permitted line emission. The possibility that a wind is a common and a significant contribution of the He emission in CTTS means that further study of its properties may ultimately indicate the origin of the wind in these objects.

Table 1
He I, He II *NC* Parameter Averages.

ID	λ (Å)	N	$\mu \pm \sigma$ (km/s)	FWHM $\pm \sigma$ (km/s)
He I	5876	28	5 ± 6	47 ± 7
	6678	26	7 ± 6	37 ± 6
	4472	12	6 ± 3	37 ± 6
	4713	13	6 ± 4	34 ± 9
He II	4686	13	10 ± 5	55 ± 10

Table 2

λ5876 *NC*, *BC* Variation.

	NC					*BC*					
Object	[a]$\Delta\delta$	[b]$\Delta\mu$		[c]$\Delta\mu$		[a]$\Delta\delta$	[b]$\Delta\mu$		[c]$\Delta\mu$		[d]
AA Tau	-21	c→r	9	c→r	+12	...	...	...	...	...	
BP Tau	15	c→c	1	c→c	-2	2	b→c	17			
CI Tau	5	c→c	-8			7	b→c	4			
DF Tau	19	r→r	2	r→r	-4	32	r→r	11	r→r	43	*
DG Tau	4	r→r	-5			-17	c→b	-16			
DL Tau	-10	c→c	3	c→r	7	-9	b→c	18			
DQ Tau	4	c→c	-7			-22	b→c	47			
DR Tau	-19	r→c	-3	r→c	-4	-8	b→b	6	b→b	23	*
FM Tau	<1	c→c	1			...	...	...	...	...	
GG Tau	4	c→c	3			5	b→b	-16			
GM Aur	<1	c→c	1			10	b→b	-5			
LK Ca8	-9	c→c	1			...	...	...	...	...	
RW Aur	10	r→c	-3	r→b	-13	36	b→b	11	b→c	48	*
UY Aur	-21	c→r	9	c→r	12	40	b→r	75			
V$_{836}$Tau	14	c→c	3			...	...	...	...	...	

Note.— The variations in the FWHM and centroid velocities are with respect to the epoch included in the reference sample, for objects with at least *NC* detection at more than one epoch. The blanks in columns 5-6 and 10-11 correspond to objects observed at only 2 epochs. The dots refer to objects for which only the *NC* was detected. Columns 3, 5, 8 and 10 list the sign of centroid velocity at the epoch included in the reference sample and at the epoch of variation, with 'b' referring to blueshifted ($\mu < -5$ km/s), 'c' to centered and 'r' to redshifted ($\mu > 5$ km/s) centroid velocities with respect to the stellar photosphere. Other column headings are as follows:

[a] Maximum *percent* change in the FWHM.

[b] Sign and magnitude of the centroid velocity variation in km/s, corresponding to the epoch used in (a).

[c] Sign and magnitude of the largest centroid velocity variation in km/s, not necessarily corresponding to the epoch used in (a,b).

[d] The asterisk denotes that the epoch for which the maximum *BC* FWHM variation was observed does not correspond to the epoch for which the maximum *NC* FWHM variation occurs.

Table 3

Magnetospheric Velocities for $M_* = 0.5M_\odot$, $R_* = 2R_\odot$.

R_B	θ_o	$-v_z$ max $\theta \sim 71.4^o$		v_{pol} max $\theta \sim 71.4^o$		v_{pol} max $\theta = \theta_o$		i	$v_{los}(60^o)$ $\theta = \theta_o$	
2	45.0^o	-44.7	-44.0	74	73	218	217	72^o	214	213
3	35.3^o	-36.5	-34.7	60	57	252	250	54^o	251	249
4	30.0^o	-31.6	-27.7	52	46	267	263	46^o	260	256
5	26.6^o	-28.3	-21.0	47	35	276	270	41^o	261	254
6	24.1^o	-25.8	-12.1	43	20	282	273	37^o	259	251
6.5	23.1^o	-24.8	-2.5	41	4	284	273	35^o	256	247

Note.— Velocities listed (in km s^{-1}) are for a particle falling onto the star along a dipolar streamline that is rotating at the stellar angular velocity $\Omega_* \sim 8.6 \times 10^{-6}$ rad s^{-1}. For each velocity the gravitational term only is included in the first column and both the gravitational and the centripetal terms are included in the second column. Note that for magnetospheric sizes less than $5R_*$, the centripetal term has a negligible effect on v_{pol} and v_z while for larger sizes the centripetal term becomes dominant in some range of θ. For $R_B = 6.5R_*, 7R_*$ and $8R_*$, a particle starting at polar angle greater than 72.0^o, 63.7^o, and 53.3^o, respectively, has such a large rotational kinetic energy that no infall can occur. Such instances are denoted by dots. The reason that $v_{LOS}(60^o)$ first increases and then decreases as the magnetosphere gets larger is the result of two effects. While infall from larger distances leads to larger velocities, an observer looking at 60^o from the symmetry axis views the system at angles that differ increasingly from that at which the maximum poloidal velocity would result. Column 1: The size of the dipole field line, in units of the stellar radius. Column 2: The polar angle at which the dipole streamline intersects the stellar surface. Columns 3,4: The largest blueshifted centroid velocity occurs for $\theta \sim 71.3^o - 71.5^o$ and would be observed at inclination angle $i = 0^o$. Columns 5,6: The poloidal velocity for $\theta \sim 71.3^o - 71.5^o$. Columns 7,8: v_{polmax} is the poloidal velocity attained by an infalling particle just before intersecting the stellar surface. Column 9: The inclination angle at which v_{polmax} would be observed. Columns 10,11: $v_{los}(60^o)$ is the maximum poloidal velocity observed at an inclination angle of $i = 60^o$ to the line-of-sight, where $v_{los} = -v_R \sin i - v_z \cos i$.

Table 4

NC and *BC* W_λ Ratios for λ5876 and λ6678.

[a]r_R	*Object* W_λ(5876)	[b]α	W_λ(6678)	[c]α	[d]R(NC)	[e]$R(BC)$	[f]
	AA Tau						
0.6	2.04 (0.17)	1.0	0.65 (0.16)	<0.1	1.55 (0.46)	... ...	*
0.2	0.61 (0.16)	<0.1	0.15 (0.06)	<0.1	4.07 (1.95)	... ...	
0.3	1.68 (0.08)	<0.1	0.79 (0.11)	<0.1	2.13 (0.31)	... ...	
	AS 353A						
5.1	0.95 (0.16)	>32	0.94 (0.11)	>24	... ...	1.06 (0.22)	*
	BP Tau						
0.4	1.25 (0.16)	0.6	0.43 (0.22)	<0.1	1.79 (0.99)	... ...	*
0.6	1.16 (0.19)	0.6	0.33 (0.06)	<0.1	2.18 (0.70)	... ...	
0.6	1.19 (0.17)	<0.1	0.42 (0.06)	<0.1	2.83 (0.57)	... ...	
	CI Tau						
0.5	2.52 (0.35)	3.0	0.52 (0.14)	<0.1	1.21 (0.75)	... ...	
0.4	2.04 (0.17)	2.5	0.75 (0.19)	1.4	1.90 (1.29)	3.30 (1.47)	*
	CW Tau						
1.7	3.08 (0.39)	>51	0.55 (0.29)	>17	... ...	5.92 (3.39)	
	CY Tau						
0.2	0.89 (0.25)	<0.1	<0.02 ...	...	... ...	... ...	*

Continued on Next Page

Table 4 Continued

[a]r_R	*Object* W_λ(5876)	[b]α	W_λ(6678)	[c]α	[d]R(NC)	[e]$R(BC)$	[f]
	DD Tau						
2.9	5.99 (0.32)	1.1	2.07 (0.30)	0.8	2.38 (0.67)	3.55 (1.22)	
	DE Tau						
0.6	1.42 (0.26)	2.5	0.34 (0.10)	<0.1	1.18 (0.84)	... ...	
	DF Tau						
1.6	4.43 (0.23)	0.8	1.44 (0.10)	<0.1	1.71 (0.20)	... ...	
0.7	3.64 (0.27)	1.1	1.22 (0.17)	0.7	2.79 (0.88)	3.18 (1.01)	*
0.5	3.53 (0.21)	0.8	0.68 (0.10)	<0.1	2.82 (0.52)	... ...	
	DG Tau						
2.0	5.31 (0.52)	15.1	0.86 (0.12)	>15.4	... ...	5.79 (1.11)	
3.0	2.73 (0.25)	11.5	1.13 (0.23)	8.2	1.83 (1.5)	2.49 (0.62)	
3.6	3.52 (0.30)	38.1	1.11 (0.14)	17.6	1.67 (2.0)	3.27 (0.52)	*
	DK Tau						
0.5	1.32 (0.09)	<0.1	0.55 (0.07)	<0.1	2.40 (0.35)	... ...	*

Continued on Next Page

Table 4 Continued

[a]r_R	*Object* W_λ(5876)	[b]α	W_λ(6678)	[c]α	[d]R(NC)	[e]$R(BC)$	[f]
	DL Tau						
2.4	3.96 (0.23)	4.6	1.19 (0.18)	2.1	1.82 (1.03)	4.01 (0.94)	
2.1	2.52 (0.73)	2.0	1.12 (0.13)	1.4	2.18 (2.06)	2.28 (1.06)	
1.1	6.63 (0.50)	9.3	1.83 (0.37)	5.1	2.13 (3.11)	3.92 (1.00)	*
1.4	6.15 (0.47)	8.8	1.72 (0.31)	4.7	2.07 (2.65)	3.89 (0.91)	
	DN Tau						
0.1	0.66 (0.05)	<0.1	0.29 (0.09)	<0.1	2.28 (0.73)	... ...	*
	DO Tau						
4.7	4.55 (0.25)	0.6	1.72 (0.17)	0.4	2.39 (0.39)	3.22 (1.18)	*
	DQ Tau						
0.2	0.97 (0.22)	3.7	<0.02 ...	...	... ...	... ...	*
0.2	1.40 (0.18)	0.5	0.48 (0.07)	<0.1	1.92 (0.47)	... ...	
	DR Tau						
20	3.86 (0.18)	8.0	1.98 (0.28)	4.1	1.10 (0.92)	2.16 (0.40)	*
10	5.30 (0.14)	5.8	1.95 (0.15)	2.6	1.50 (0.51)	3.16 (0.35)	
6.4	2.63 (0.09)	3.3	0.96 (0.06)	1.7	1.77 (0.40)	3.35 (0.37)	i
9.2	3.50 (0.20)	3.4	1.39 (0.20)	2.0	1.68 (0.83)	2.95 (0.68)	

Continued on Next Page

Table 4 Continued

[a]r_R	*Object* W_λ(5876)	[b]α	W_λ(6678)	[c]α	[d]R(NC)	[e]$R(BC)$	[f]
	DS Tau						
1.0	1.40 (0.17)	0.4	0.51 (0.08)	<0.1	1.92 (0.45)	... ...	*
	FM Tau						
3.0	2.34 (0.27)	<0.1	0.82 (0.16)	<0.1	2.79 (0.62)	... ...	*
3.2	2.25 (0.31)	<0.1	<0.02 ...	...	... ...	... ...	
	FP Tau						
0.1	1.09 (0.10)	<0.1	<0.20 (0.49)	<0.1	... ...	... ...	
0.1	0.41 (0.16)	<0.1	<0.02 ...	...	... ...	... ...	
	GG Tau						
0.5	1.58 (0.27)	8.9	<0.02 ...	...	... ...	... ...	
0.3	2.07 (0.21)	7.2	0.42 (0.12)	2.5	2.08 (1.0)	6.07 (2.0)	*
0.1	1.48 (0.19)	6.1	0.27 (0.13)	2.1	2.33 (0.7)	6.68 (3.7)	
	GI Tau						
0.2	1.24 (0.07)	<0.1	0.58 (0.09)	<0.1	2.14 (0.35)	... ...	*
	GK Tau						
0.2	0.61 (0.10)	0.7	0.24 (0.05)	<0.1	1.46 (0.52)	... ...	*, i

Continued on Next Page

Table 4 Continued

[a]r_R	*Object* W_λ(5876)	[b]α	W_λ(6678)	[c]α	[d]R(NC)	[e]$R(BC)$	[f]
	GM Aur						
0.2	1.28 (0.27)	1.3	0.60 (0.16)	<0.1	0.93 (0.51)	... ...	*, i
0.2	1.14 (0.19)	1.2	0.56 (0.24)	<0.1	0.93 (0.52)	... ...	i
	HK Tau						
1.1	1.85 (0.47)	<0.1	0.67 (0.18)	<0.1	2.76 (1.02)	... ...	
	HN Tau						
0.8	3.78 (0.39)	>47	1.31 (0.79)	>25	... ...	2.96 (1.90)	*
	LK Ca8						
0.2	0.73 (0.17)	<0.1	0.24 (0.10)	<0.1	3.04 (1.45)	... ...	*
0.2	0.56 (0.06)	<0.1	0.19 (0.10)	<0.1	2.95 (1.58)	... ...	
0.1	0.67 (0.14)	<0.1	0.17 (0.05)	<0.1	3.94 (1.42)	... ...	
0.1	0.71 (0.14)	<0.1	0.22 (0.06)	<0.1	3.23 (1.09)	... ...	
	RW Aur						
2.0	2.09 (0.15)	4.8	1.53 (0.31)	10.0	2.57 (2.0)	1.24 (0.29)	*, i
1.8	2.35 (0.22)	2.5	1.19 (0.12)	4.0	2.79 (0.5)	1.77 (0.32)	i
1.8	1.70 (0.21)	2.1	0.84 (0.10)	1.6	1.69 (0.84)	2.27 (0.61)	i
1.7	2.42 (0.17)	1.9	1.26 (0.11)	1.6	1.75 (0.54)	2.05 (0.37)	i

Continued on Next Page

Table 4 Continued

[a]r_R	*Object* $W_\lambda(5876)$	[b]α	$W_\lambda(6678)$	[c]α	[d]R(NC)	[e]$R(BC)$	[f]
	UY Aur						
1.3	3.30 (0.21)	2.9	1.10 (0.18)	1.6	2.00 (0.99)	3.66 (1.03)	*
0.6	1.87 (0.15)	1.1	0.56 (0.04)	<0.1	1.57 (0.29)	... ...	
0.3	1.64 (0.11)	1.2	0.58 (0.12)	0.5	1.95 (0.68)	4.33 (1.5)	
0.2	1.59 (0.08)	<0.1	0.68 (0.07)	<0.1	2.34 (0.27)	... ...	
0.4	1.48 (0.11)	1.1	0.57 (0.15)	<0.1	1.26 (0.38)	... ...	
	UZ Tau E						
0.7	2.62 (0.42)	1.4	0.49 (0.16)	<0.1	2.20 (1.12)	... ...	*
	V836 Tau						
0.1	0.18 (0.04)	<0.1	<0.02 ...	<0.1	... ...	... ...	
0.1	0.06 (0.03)	<0.1	<0.02 ...	<0.1	... ...	... ...	
0.1	0.17 (0.04)	<0.1	<0.02 ...	<0.1	... ...	... ...	
	YY Ori						
0.1	1.31 (0.19)	0.8	0.52 (0.13)	<0.1	1.44 (0.51)	... ...	*, i

Note.— Equivalent Widths (in Å) for the observed profile are with respect to the total continuum. Uncertainties for these and for the ratios are in parenthesis. The dots indicate non-detections.

[a] The ratio of continuum to photospheric flux or veiling, at 5200Å.

[b] Note: $\alpha = BC/NC$ for λ5876

[c] Note: $\alpha = BC/NC$ for λ6678

[d] Note: $R(NC) = NC(5876)/NC(6678)$

[e] Note: $R(BC) = BC(5876)/BC(6678)$

[f] The asterisk denotes the epoch included in the reference sample, and 'i' indicates that redshifted absorption below the continuum was detectable at that epoch.

Table 5

$W_\lambda(NC)$ Ratios for He I λ4472, λ4713 and He II λ4686.

[a]r_B	*Object* [b]W_λ(4472)	[b]W_λ(4713)	[b]W_λ(4686)	[c]R(He I)	[d]R(He I,II)	[e]
	AA Tau					
0.2	0.42 (0.22)	0.18 (0.07)	0.48 (0.07)	2.33 (1.55)	0.87 (0.48)	*
0.2	0.53 (0.29)	0.13 (0.06)	0.24 (0.08)	4.04 (2.89)	2.19 (1.40)	
	BP Tau					
1.0	0.65 (0.20)	0.12 (0.05)	0.48 (0.24)	5.42 (2.74)	1.36 (0.80)	
0.8	0.45 (0.20)	0.13 (0.12)	0.48 (0.20)	3.46 (3.54)	0.94 (0.57)	
0.6	0.67 (0.18)	0.09 (0.05)	0.50 (0.10)	7.42 (4.95)	1.33 (0.45)	*
	DF Tau					
9.1	0.39 (0.08)	0.12 (0.03)	0.19 (0.06)	3.26 (0.95)	2.06 (0.80)	
7.5	0.67 (0.06)	0.12 (0.05)	0.20 (0.06)	5.59 (2.29)	3.35 (1.12)	
7.3	1.00 (0.16)	0.16 (0.04)	0.24 (0.06)	6.26 (1.89)	4.18 (1.24)	
4.3	1.38 (0.11)	0.28 (0.07)	0.45 (0.07)	4.95 (1.25)	3.08 (0.54)	
1.8	1.21 (0.10)	0.26 (0.06)	0.49 (0.12)	4.65 (1.07)	2.47 (0.64)	*
	DK Tau					
0.6	0.54 (0.23)	0.12 (0.05)	0.61 (0.07)	4.49 (2.60)	0.88 (0.39)	*

Continued on Next Page

Table 5 Continued

[a]r_B	[b]W_λ(4472)	[b]W_λ(4713)	[b]W_λ(4686)	[c]R(He I)	[d]R(He I,II)	[e]
	Object					
	DL Tau					
5.7	0.29 (0.11)	0.23 (0.05)	0.51 (0.12)	1.27 (0.55)	0.57 (0.25)	*
	DN Tau					
0.1	0.62 (0.17)	0.07 (0.04)	0.24 (0.06)	8.79 (5.92)	2.56 (0.93)	*
0.1	0.54 (0.20)	<0.05 (0.06)	0.23 (0.08)	... ...	2.37 (1.21)	
0.3	0.61 (0.20)	<0.04 (0.06)	0.27 (0.14)	... ...	2.26 (1.38)	
	DR Tau					
13.2	0.26 (0.09)	0.13 (0.02)	0.45 (0.04)	1.99 (0.73)	0.57 (0.20)	
8.9	0.34 (0.10)	0.41 (0.11)	0.46 (0.07)	0.82 (0.33)	0.73 (0.24)	
8.1	0.41 (0.05)	0.14 (0.02)	0.53 (0.08)	2.93 (0.58)	0.77 (0.15)	*
	DS Tau					
1.9	0.71 (0.16)	0.13 (0.04)	0.42 (0.05)	5.46 (2.19)	1.69 (0.43)	*
	GG Tau					
0.3	0.10 (0.07)	<0.07 (0.05)	<0.06 (0.04)	... ...	... ...	*
	GK Tau					
0.3	0.76 (0.18)	0.09 (0.06)	0.36 (0.06)	8.46 (6.25)	2.11 (0.63)	*

Continued on Next Page

Table 5 Continued

[a]r_B	[b]W_λ(4472)	[b]W_λ(4713)	[b]W_λ(4686)	[c]R(He I)	[d]R(He I,II)	[e]
	Object					
	GM Aur					
0.1	0.45 (0.32)	0.06 (0.05)	0.27 (0.11)	7.50 (8.22)	1.67 (1.37)	*
	RW Aur					
4.3	0.14 (0.62)	... ...	0.23 (0.07)	... ...	0.63 (2.70)	
3.3	... ...	0.12 (0.03)	0.44 (0.07)	... ...	... ...	*
3.0	... ...	0.13 (0.03)	0.34 (0.05)	... ...	... ...	
2.7	... ...	0.13 (0.05)	... ...	... ...	... ...	
	UY Aur					
0.5	1.04 (0.14)	0.08 (0.03)	0.25 (0.04)	13.0 (4.73)	4.16 (0.88)	

Note.— Objects listed show unblended, detectable emission in at least one of the three lines. Omitted from this list are AS 353A, CW Tau and DG Tau, for which λ4472 is blended with Ti II, and λ4714 and λ4686 are undetectable. Equivalent widths for λ4713 and λ4686 are the total observed, since these lines are narrow. The W_λ(4472) is for the *NC* only, as the *BC* is compromised by a Ti II blend. Uncertainties are in parenthesis. The dots are for cases where one of the lines used in the ratio was either blended or undetected.

[a] The ratio of continuum to photospheric flux or veiling, measured at λ4500 Å.

[b] The equivalent width with respect to the total continuum, in Å.

[c] Note: $R(\mathrm{HeI}) = NC(4472)/NC(4713)$

[d] Note: $R(\mathrm{HeI,II}) = NC(4472)/NC(4686)$

[e] The asterisk denotes the epoch included in the reference sample.

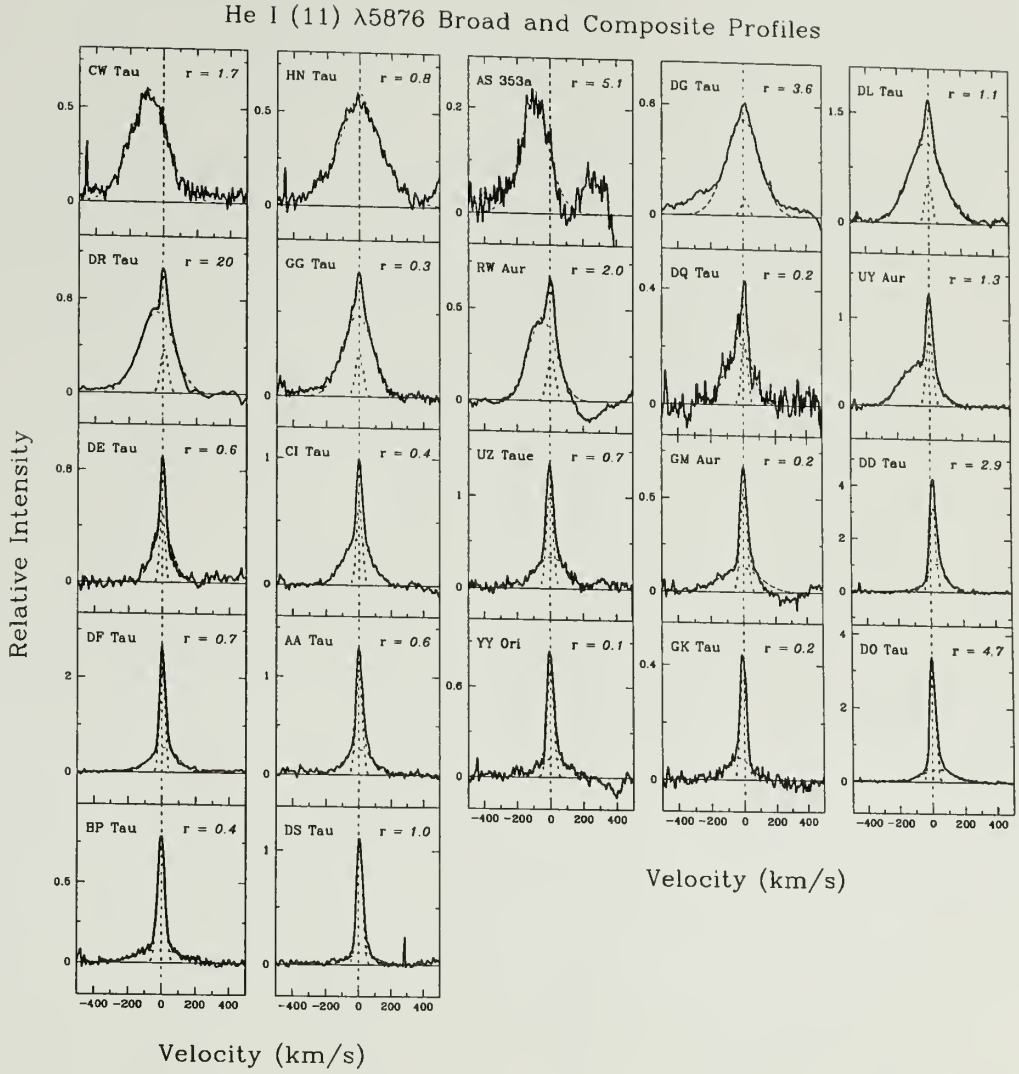

Figure 3. Observed broad and composite He I profiles. The profiles of He I λ5876 can be classified into broad (N = 3), composite (N = 19) and narrow (N = 9). The profiles are shown in order of decreasing relative strength of the broad component, or *BC*, to the narrow component, or *NC* (Figure 4), labeled by the ratio of excess continuum to photospheric emission or veiling r, at 5200Å. Best Gaussian fits are superposed on the composite profiles. The objects CW Tau, HN Tau and AS 353a have no detectable *NC* emission. Intensities are in units of the observed local continuum level and velocities are with respect to the stellar photosphere.

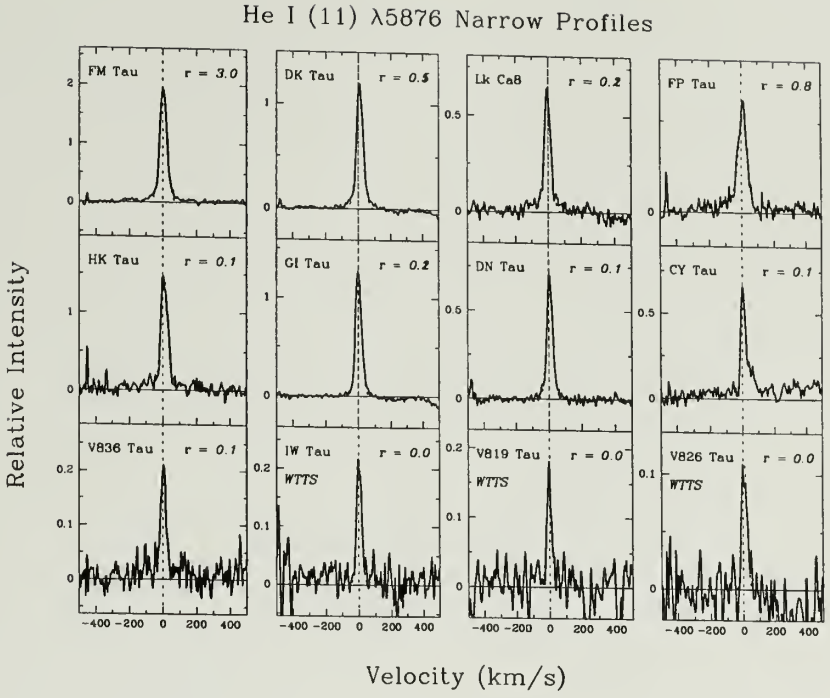

Figure 4. Observed narrow He I profiles. The observed profiles of He I λ5876 can be classified into broad, composite and narrow morphologies. This figure displays the narrow profiles with detectable emission in the *NC* only (N = 9). The profiles are labeled by the ratio of excess continuum to photospheric emission or veiling r, at 5200Å. Intensities are in units of the local continuum level and velocities are with respect to the stellar photosphere.

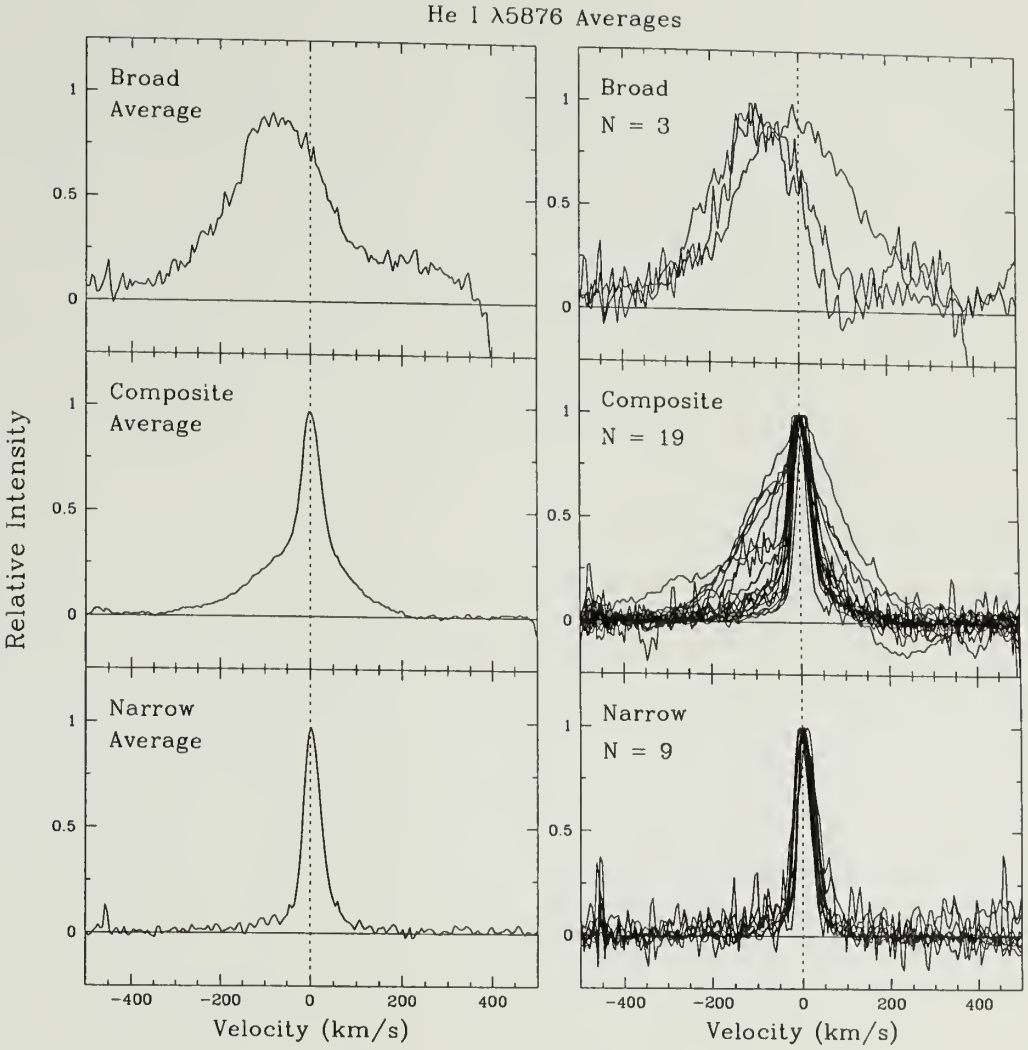

Figure 5. Comparison of the broad, composite and narrow profiles for He I λ5876. The profiles in each group were normalized to their peak value to allow a comparison of morphology. Arithmetic averages for each group are shown in the left panels. A superposition of observed profiles included in the group averages are in the right panels. The cores of the composite profiles and the narrow profiles are all similar, suggesting a common origin.

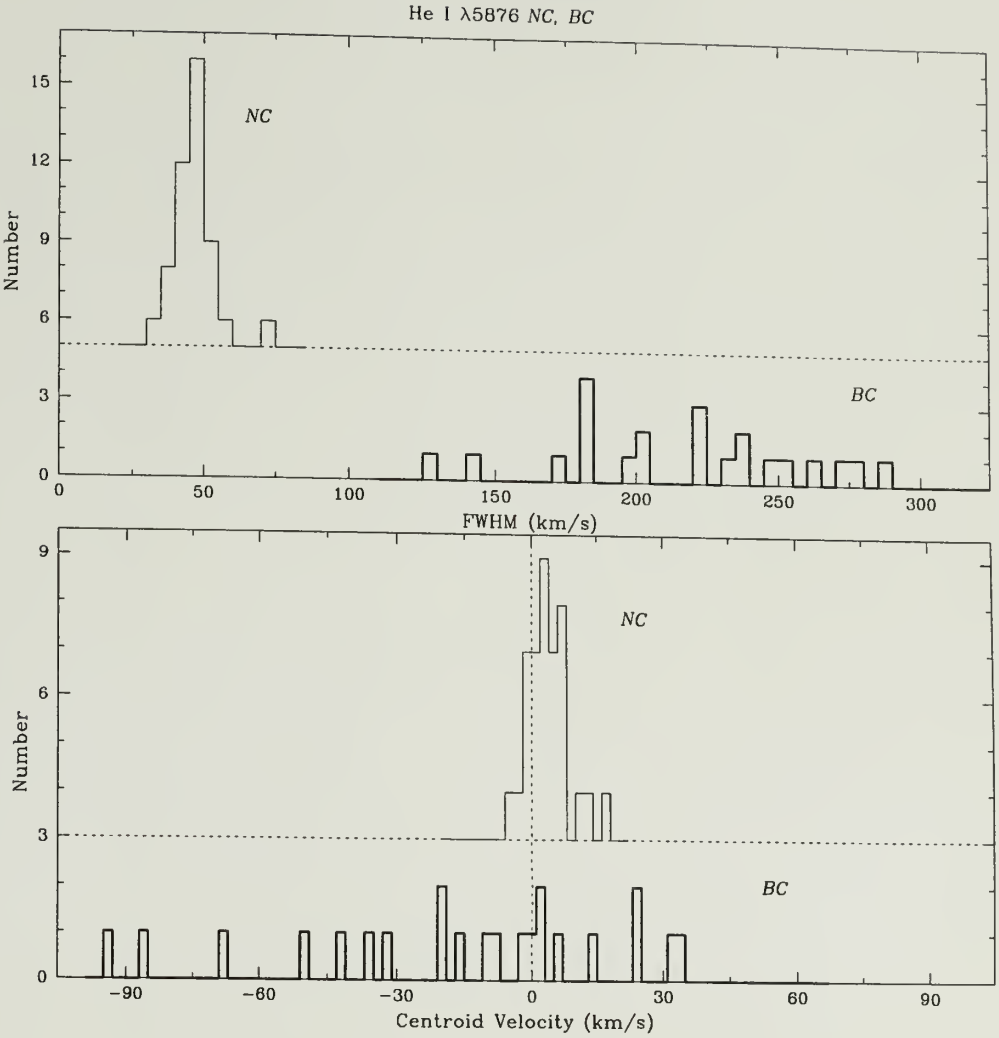

Figure 6. Best fit parameters for the Narrow component or *NC* and Broad component or *BC* for He I λ5876. Parameters for the *NC*, detected in N = 28 objects, are shown in the top subpanels and those for the *BC*, detected in N = 22 objects, in the bottom subpanels. The FWHM for the *NC* are distributed about 47 $\mathrm{km\,s^{-1}}$, while for the *BC*, the FWHM range from 128 to 287 $\mathrm{km\,s^{-1}}$. The centroid velocities for the *NC* cluster about the photospheric velocity. In contrast, the *BC* is predominantly blueshifted with velocities as high as -93 $\mathrm{km\,s^{-1}}$. A few objects show redshifted centroid velocities of up to +35 $\mathrm{km\,s^{-1}}$.

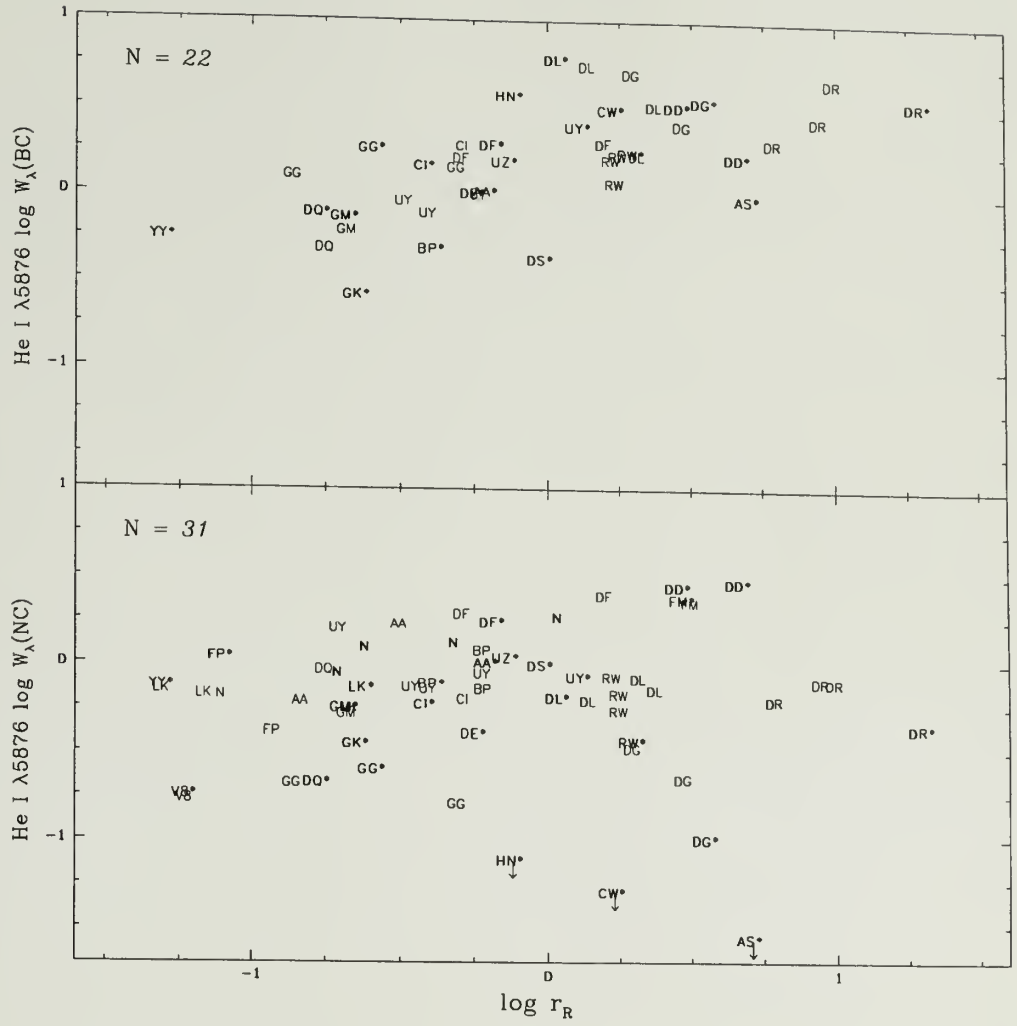

Figure 7. The He I λ5876 equivalent widths for the *NC* and *BC* versus veiling. Equivalent widths, or W_λ, for the *BC* (detected in 22 objects) are in the top panel and those for the *NC* (detected in 28 objects) are in the bottom panel. The W_λ for the *BC* appear weakly correlated with veiling while the W_λ for the *NC* show no apparent relation to veiling, contrary to what is expected if the *NC* arises close to the postshock region at the stellar surface in the magnetospheric accretion model. Labels for objects in the reference sample are marked with an asterisk and shown in bold; unmarked labels denote multiple epoch observations of these objects.

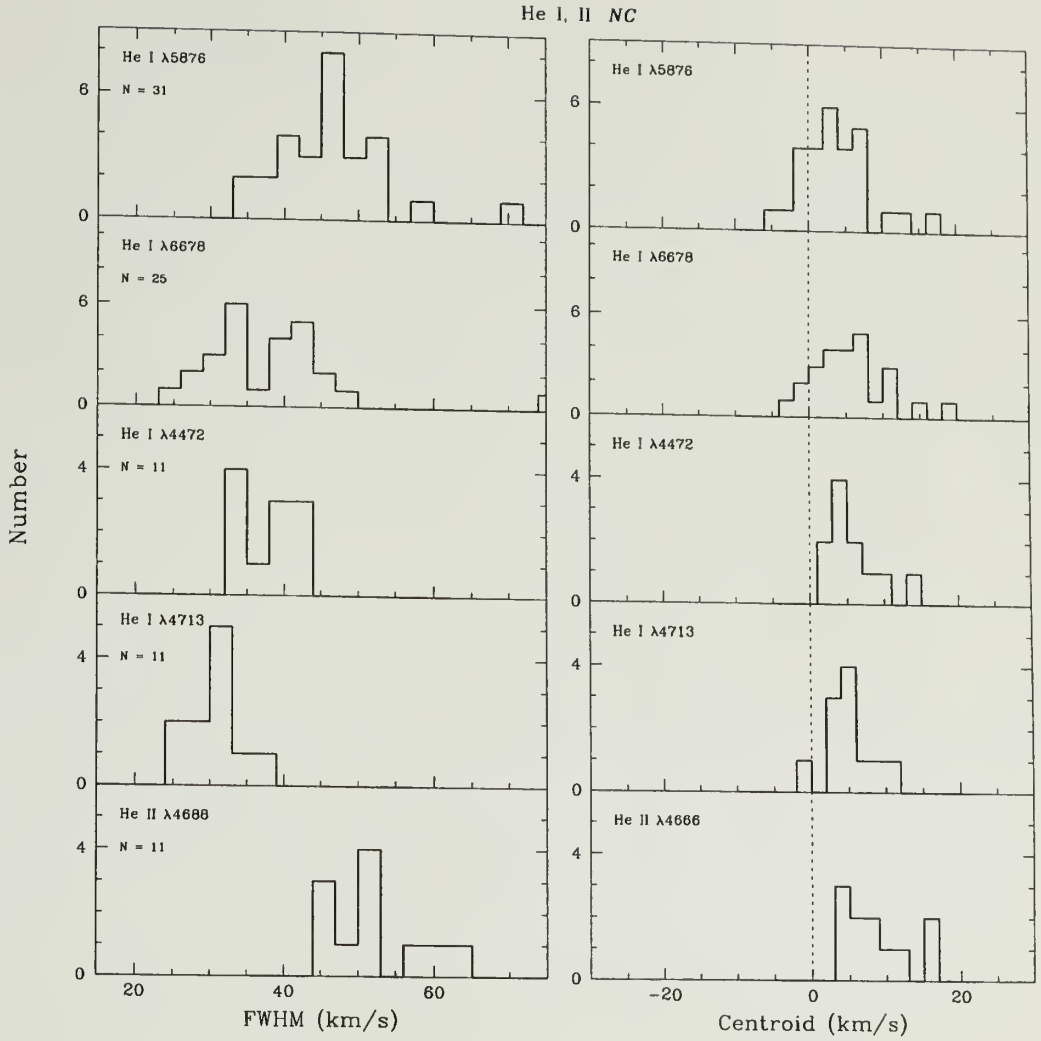

Figure 8. The *NC* kinematics for He I λ5876, λ6678, λ4472, λ4713 and He II λ4686. The strongest line, λ5876, is at the top. The He II line is at the bottom. As the line strength decreases, so does the FWHM, from an average of 47 ± 7 km s^{-1} for λ5876 to 34 ± 9 km s^{-1} for λ4713. The He II average is 55 ± 10 km s^{-1} . The centroid velocities are either centered on the stellar photosphere or redshifted for He I and are redshifted for every object with He II emission. In both ions, the centroid velocities are redshifted by ≤ 20 km s^{-1} . The *NC* kinematics are consistent with an origin close to the stellar photosphere, in the postshock region of the accretion shock.

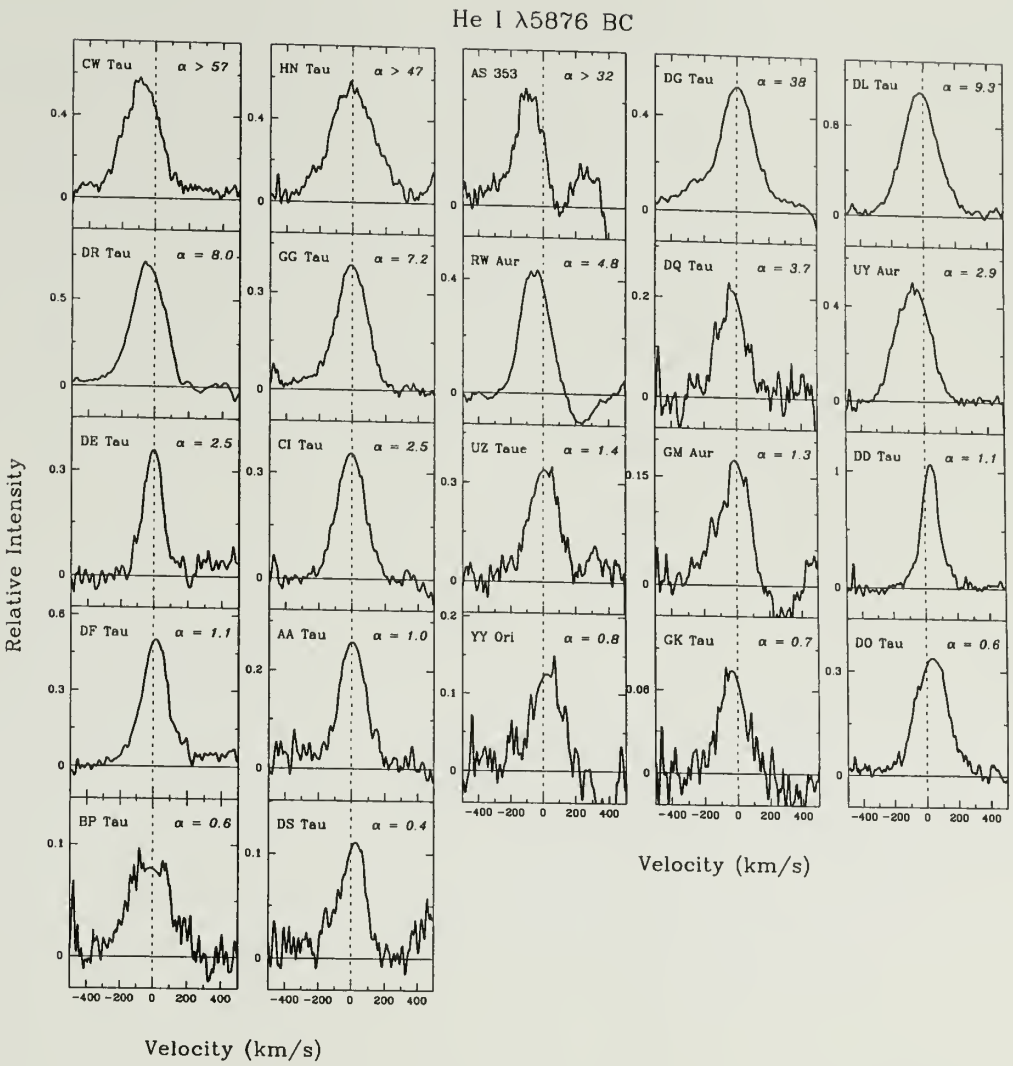

Figure 9. The *BC* Residual Profiles for λ5876. The *BC* residual profiles (obtained after subtracting the best *NC* fits from the each individual observed profile) are shown in decreasing order of $\alpha = BC/NC$, the ratio of *NC* to *BC* equivalent widths. Objects with dominant *BC* emission are at the top. In addition to the variety of morphologies exhibited in emission, four objects (RW Aur, GM Aur, GK Tau and YY Ori) exhibit redshifted absorption at velocities $\geq$100 km s^{-1} , indicative of mass infall.

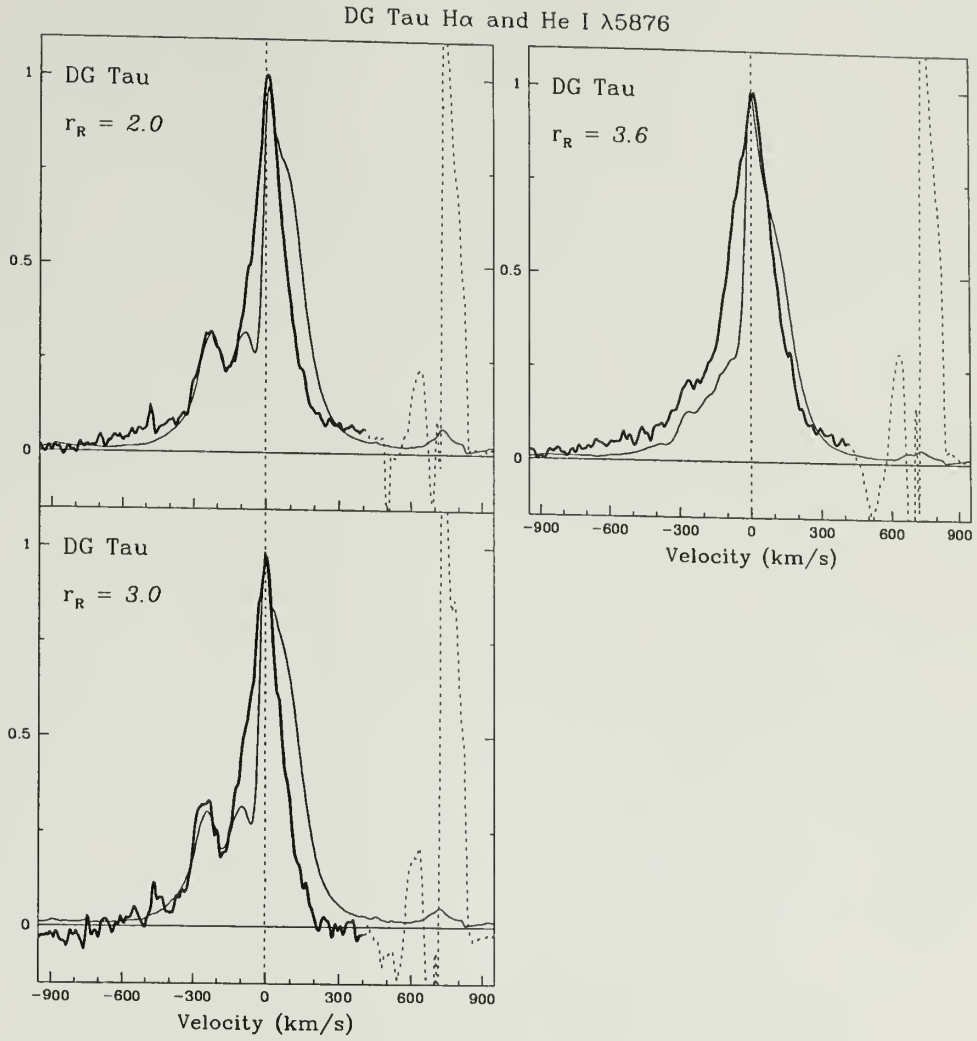

Figure 10. Comparison of He I λ5876 and Hα in DG Tau. Simultaneous λ5876 (heavy line) and Hα (light line) profiles are superposed at the 3 epochs of observation. At each epoch, a blueshifted feature of comparable morphology is found near velocities of -250 km s^{-1} in both transitions. Since Hα is thought to be optically thick, the correspondence suggests blueshifted absorption due to a wind. In this case, the centroid velocity of the *BC* emission in DG Tau is blueshifted. Estimates of the latter for the profiles which exhibit the most pronounced dip in the blue wing (left panels) are μ_{BC} = -68 km s^{-1} and -56 km s^{-1} , respectively.

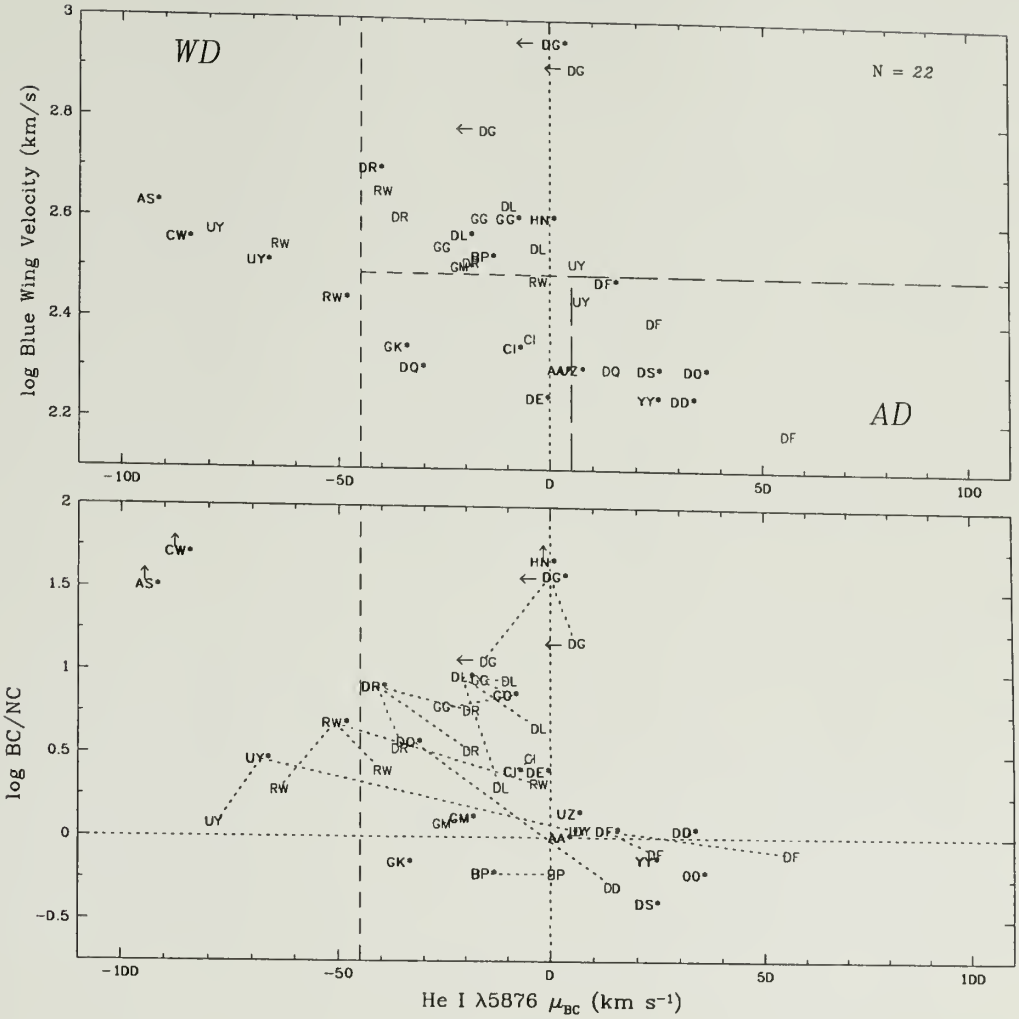

Figure 11. The λ5876 *BC* blue wing velocities at zero intensity (top) and *BC/NC* (bottom), each versus the *BC* centroid velocity, μ_{BC}. Emission with $\mu_{BC} \leq$ -45 km s^{-1} and blue wing velocities $\leq$ -309 km s^{-1} cannot arise in a magnetosphere but is consistent with a wind. For these objects *BC/NC* > 1 suggesting that the dominance of the *BC* is due to the wind. Emission with $\mu_{BC} > 5$ km s^{-1} can arise in the funnel flow close to the accretion shock. Arrows in μ_{BC} for DG Tau indicate the real values are likely to be more blueshifted than shown. Arrows in in *BC/NC* are lower limits when the *NC* is undetectable. Bold object labels with an asterisk comprise the reference sample; unmarked labels denote multiple epoch observations.

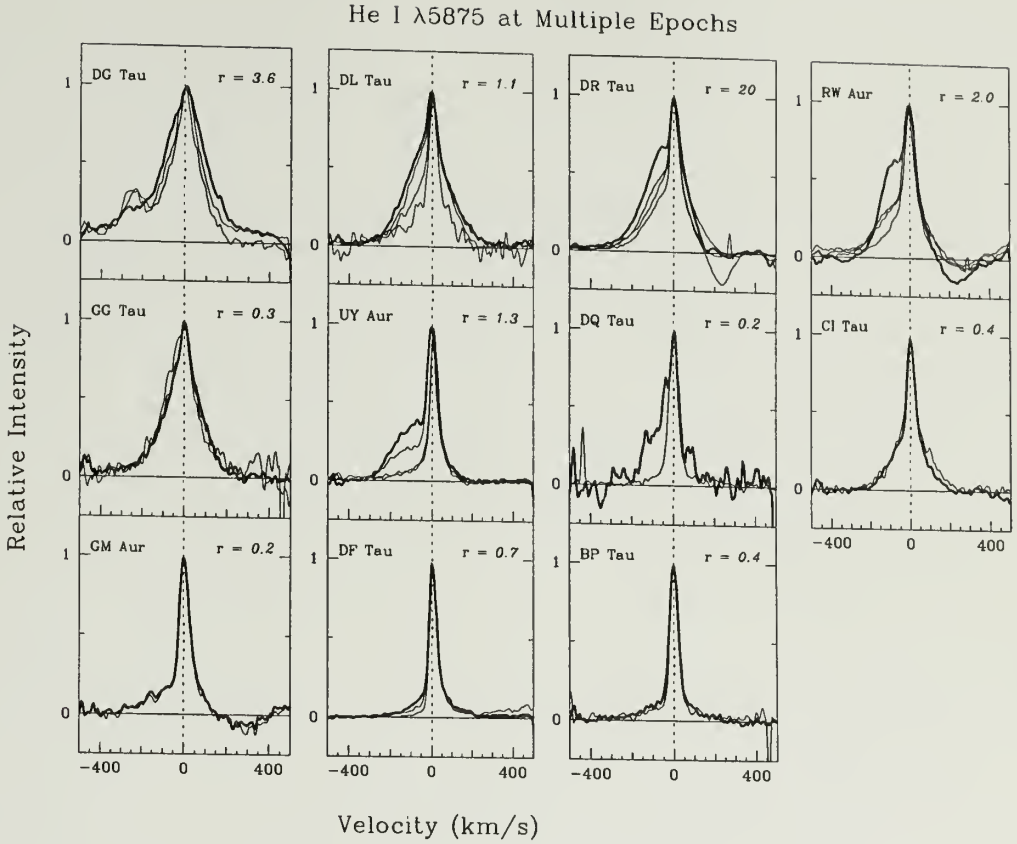

Figure 12. Observed profiles for λ5876 at multiple epochs. A superposition of observed profiles normalized to their peak value is shown for every object with multiple observations. When the contribution of the *BC* relative to the *NC* decreases, it does so predominantly in the blueshifted emission. Thus the *BC* emission tends to be blueshifted when dominant. In contrast, the redshifted emission varies less or is indistinguishable in most objects. The paucity of blueshifted emission as the *BC* amplitude decreases means the centroid velocity of the remaining emission is less blueshifted, consistent with the results of Figure 11b for the entire sample.

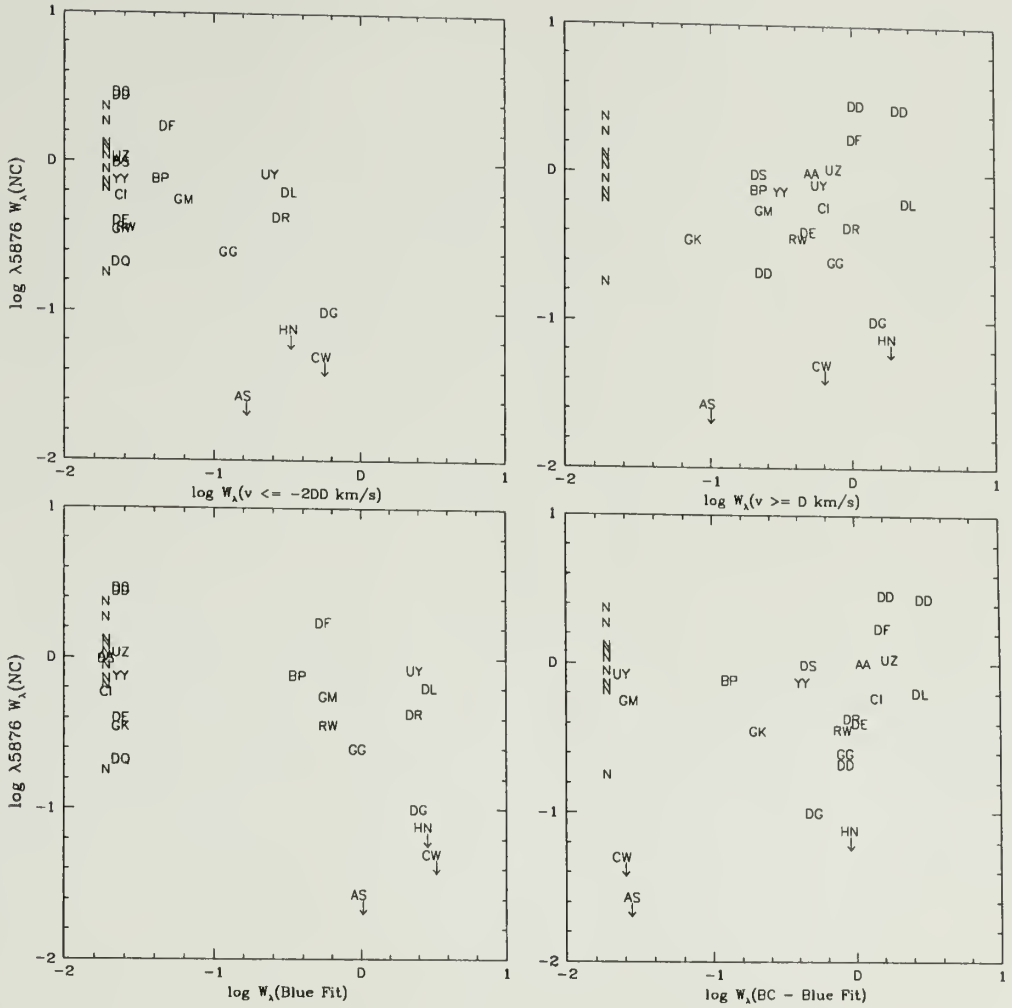

Figure 13. The *NC* equivalent widths versus equivalent widths for the *BC* wind and accretion contributions, estimated by the integration method (top) and by the wind-fit method (bottom). Both methods yield similar results and show that the wind and the accretion components are distinctly related to the *NC*. The distribution for the wind component suggests an inverse correlation with respect to the *NC*. In contrast, the accretion component appears to increase as the *NC* equivalent width increases, as expected if the former originates in the funnel flow close to the accretion shock.

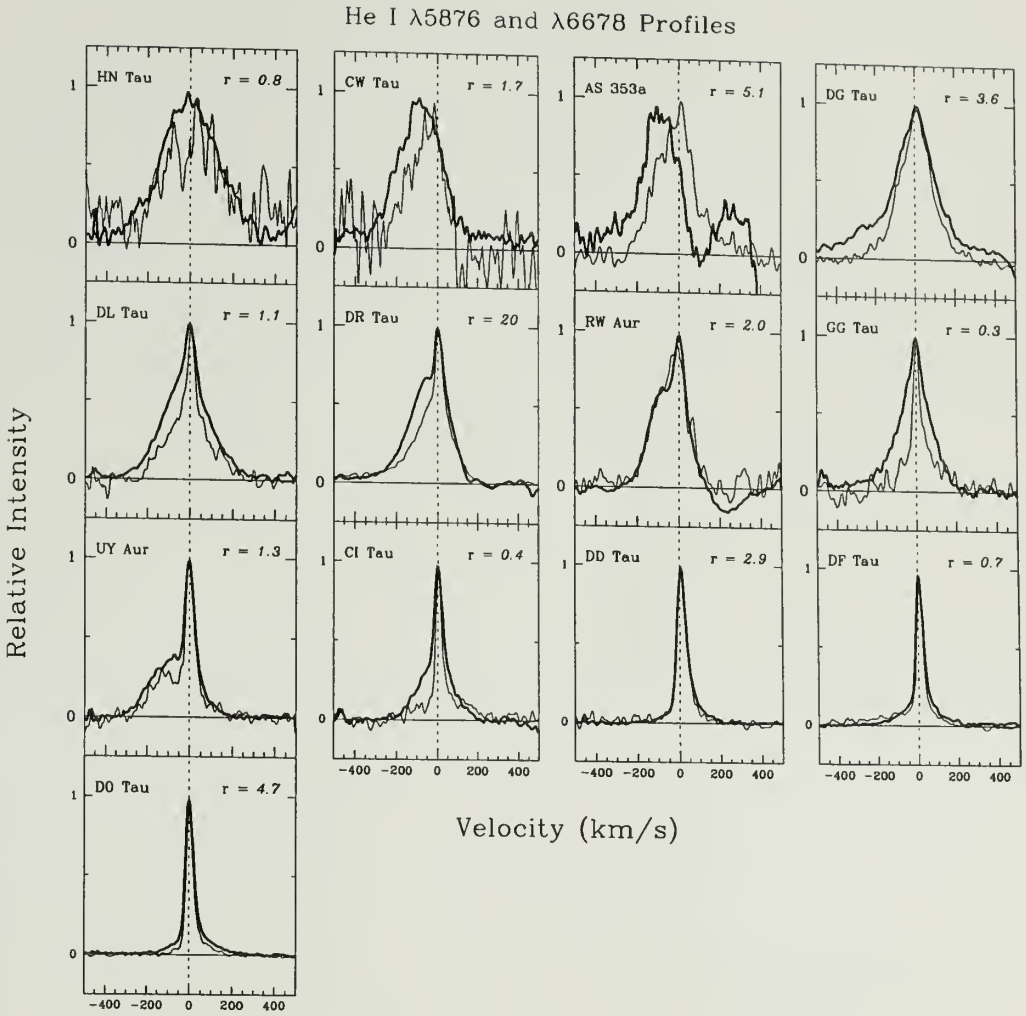

Figure 14. Comparison of λ5876 and λ6678. Profiles normalized to their peak value are superposed for the 13 objects with *BC* detectable emission in λ5876 and λ6678. They differ for objects with dominant *BC* emission and are similar for objects with dominant *NC* emission in both lines. About half of the remaining objects show a smaller *BC* to *NC* in λ6678 than in λ5876. The difference occurs predominantly in the blueshifted emission.

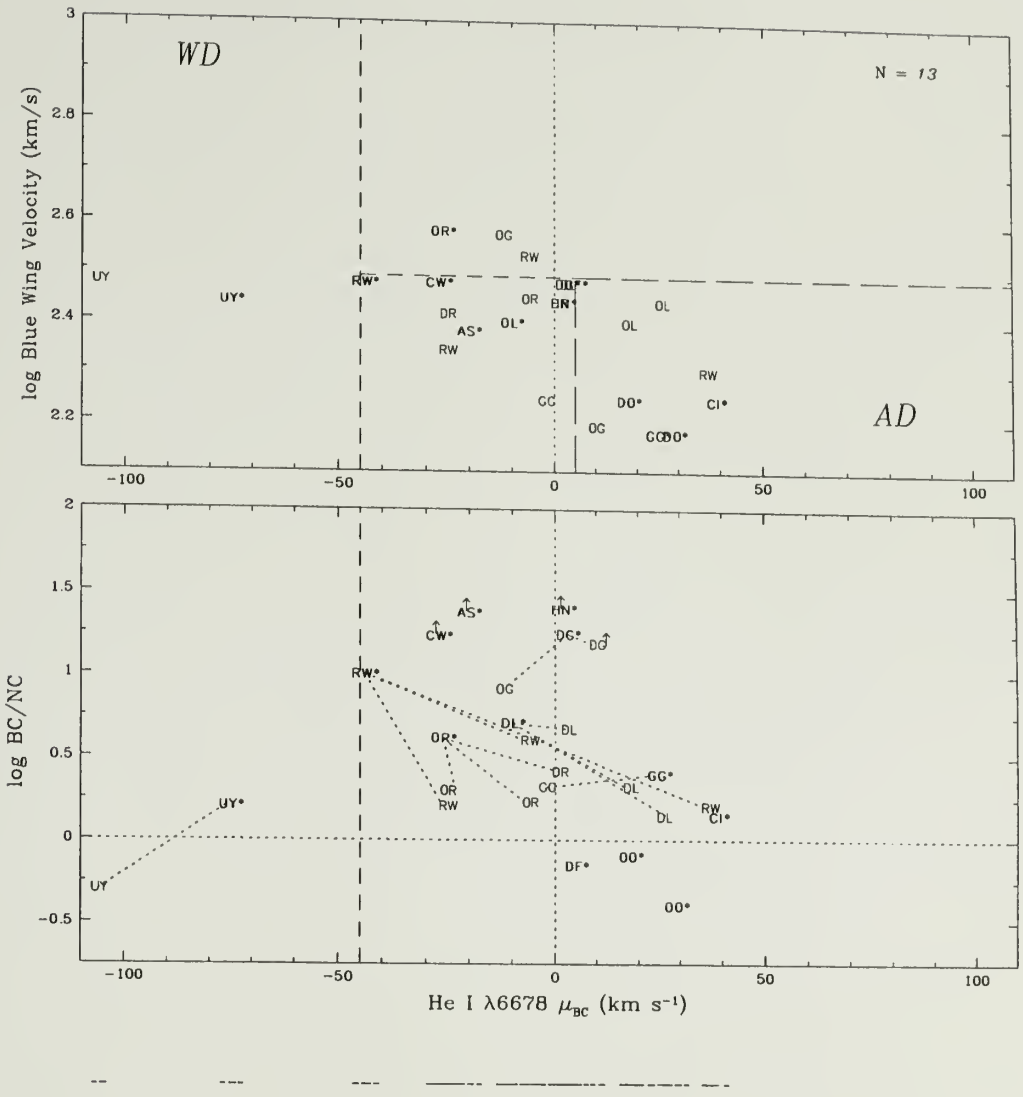

Figure 15. The λ6678 *BC* blue wing velocities at zero intensity (top) and the *BC/NC* (bottom), each versus the *BC* centroid velocity. The centroid velocities and blue wing velocities are less blueshifted for λ6678 than for λ5876 (see Figure 11a,b). As for λ5876, the *BC* in λ6678 tends to be blueshifted when dominant and redshifted as *BC/NC* decreases. However, the presence of significantly redshifted centroids for $BC/NC \leq 2$ in λ6678 suggests that the infall component associated with redshifted centroid velocities in λ5876 favors the λ6678 *BC* emission.

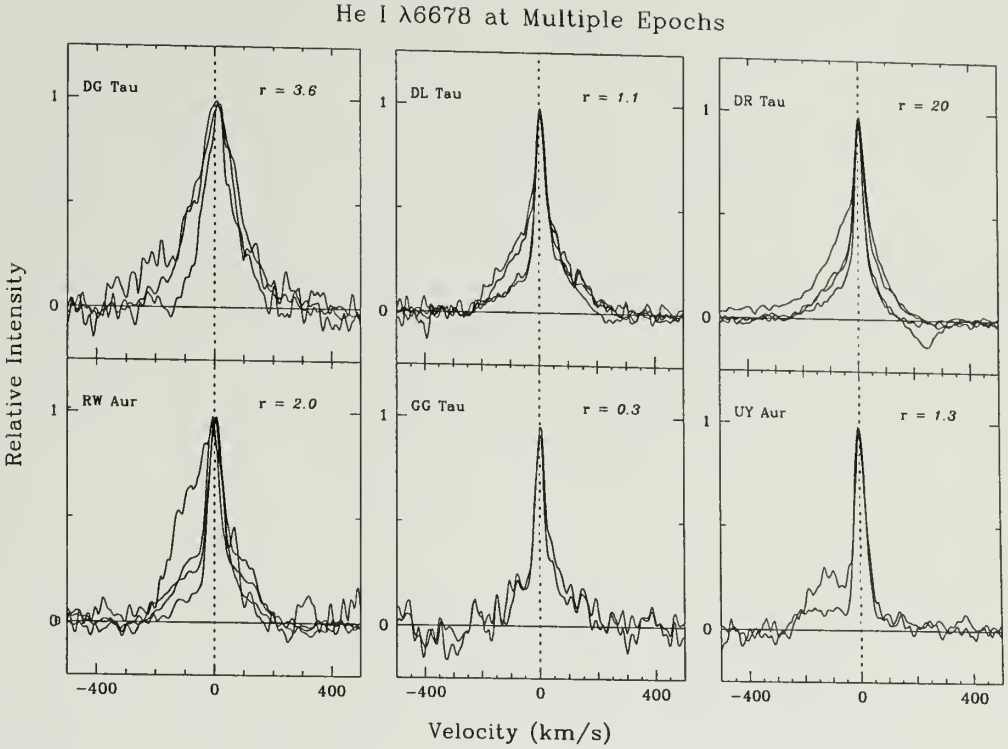

Figure 16. Profiles for λ6678 at multiple epochs. A superposition of observed profiles normalized to their peak value is shown for every object with multiple observations. As for the λ5876 profiles (Figure 12), the contribution of the *BC* relative to the *NC* decreases predominantly in the blueshifted emission, while the redshifted emission varies less or is indistinguishable in most objects. This is consistent with the results for the entire sample of objects in Figure 11b for λ5876 and Figure 15b for λ6678.

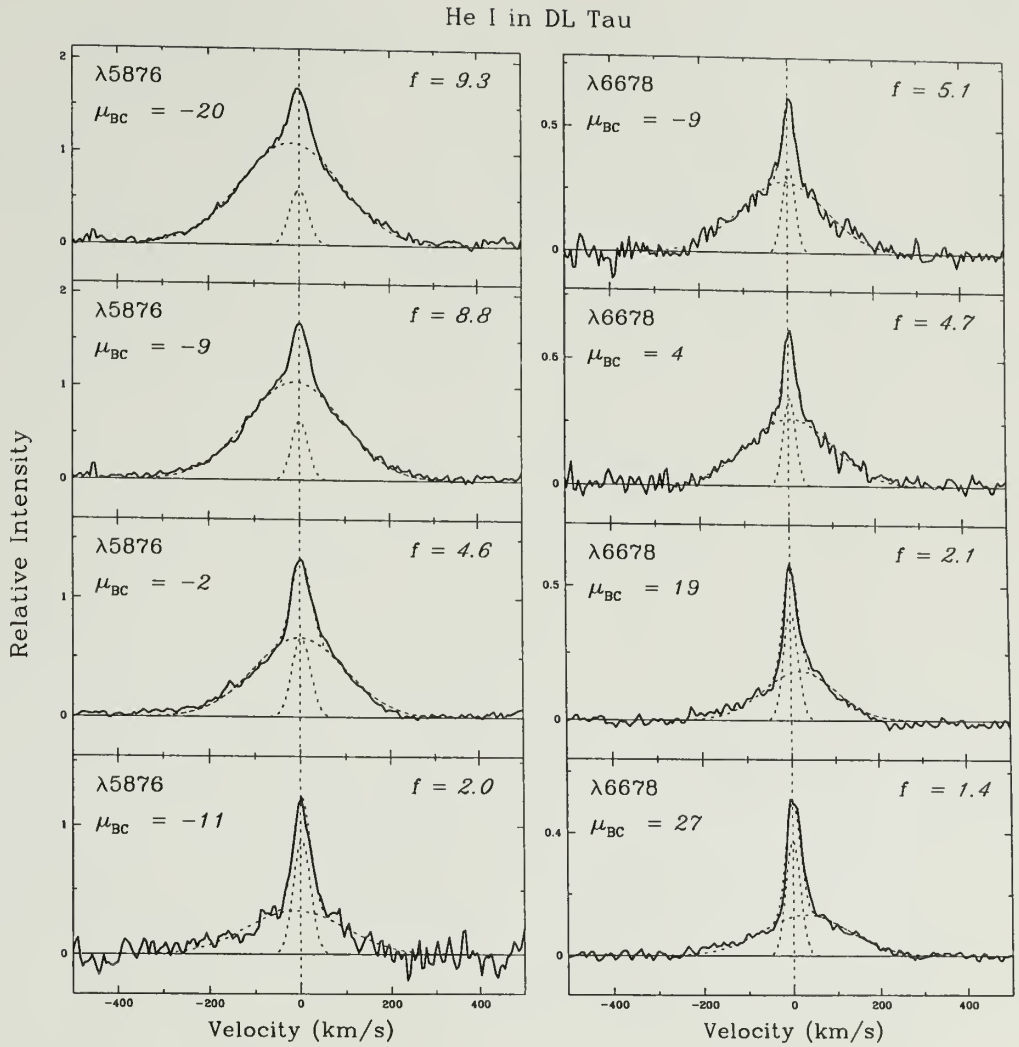

Figure 17. A comparison of λ5876 and λ6678 *BC* emission in DL Tau. Profiles for λ5876 (left panels) and for λ6678 (right panels) are shown at the four epochs of observation, in order of decreasing $f = BC/NC$. As the λ5876 BC/NC decreases below 8.8, the λ6678 *BC* becomes redshifted ($\mu_{BC} > 5$ km s^{-1}) and its BC/NC is less sensitive to changes in the λ5876 BC/NC (lower two panels). At the lowest λ5876 BC/NC level, the λ6678 *BC* may have originated primarily from the accretion component (bottom panels).

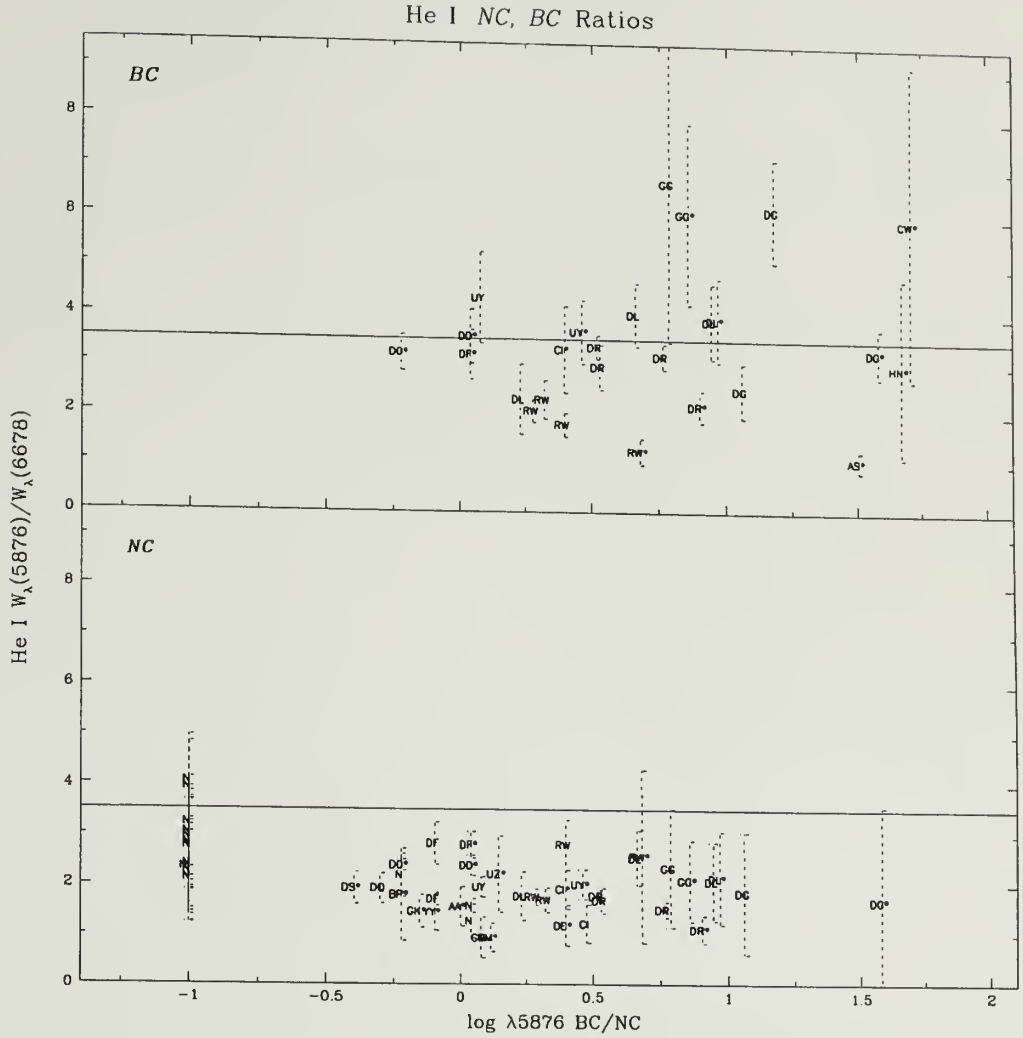

Figure 18. Equivalent width ratios for the *BC* (top) and *NC* (bottom) in simultaneously observed λ5876 and λ6678 lines. The solid line is the value expected under conditions of optically thin or nebular recombination. Ratio distributions differ between the *NC* and *BC*. The tight distribution in the *NC* suggests that uniform conditions prevail in this region. In contrast, the dispersion in the *BC* ratios suggests that a variety of physical conditions can produce *BC* emission. Uncertainties are dominated by errors of measurement in the λ6678 line. Object labels marked with asterisks denote the reference sample; unmarked labels denote multiple epoch observations.

CHAPTER 3

DR TAU

3.1. DR Tau: an Overview of Results

In this chapter the results of a study of permitted emission lines of Fe I and Fe II in the spectrum of the high accretion rate classical T Tauri star DR Tau are presented. Echelle spectra collected at the 4m Mayall telescope at KPNO between 1988 and 1992 include 4 epochs with red spectral coverage (~5000Å - 6800Å) and 3 with blue spectral coverage (~4000Å - 4950Å). A total of 62 unblended Fe I and Fe II lines are identified, their profiles are examined, and ratios of line pairs that are sensitive to column density or temperature are analyzed.

The unblended Fe profiles exhibit a systematic behavior, with FWHM increasing from 20 to $\sim 90\,\mathrm{km\,s^{-1}}$ as the equivalent width increases from 0.05 Å to several Å. The range of morphologies can be resolved in terms of a narrow component (NC) that dominates the weakest lines, and a broad component (BC) that dominates the strongest lines. The NC has FWHM $\sim 20\,\mathrm{km\,s^{-1}}$ and a radial velocity at rest with respect to the photosphere, while the BC has FWHM $\sim 100\,\mathrm{km\,s^{-1}}$, and a tendency to be blueshifted by $\leq 10\,\mathrm{km\,s^{-1}}$.

Estimates of opacities and column densities are obtained by comparing observed intensity ratios of lines from a common upper level with values expected from a

local escape probability calculation. We find (1) opacities in the NC exceed those in the BC by factors of 2-4; and (2) for the BC, $N_{FeI} \gtrsim 10^{17} - 10^{18}\,\mathrm{cm}^{-2}$ and $N_{FeII} \gtrsim 10^{18} - 10^{19}\,\mathrm{cm}^{-2}$ for kinetic temperatures in the range to 4000 to 10,000K. Ratios of NC/BC emission from a pair of Fe I lines which are insensitive to opacity suggest that the kinetic temperature in the NC exceeds that in the BC by several thousand degrees.

The centroid velocity and width of the NC in Fe I and Fe II are comparable to those from photospheric lines, suggesting a thermal or turbulent origin further broadened by stellar rotation. In the context of a magnetospheric accretion model, the NC is consistent with an origin in the post-shock gas close to the stellar surface. In contrast, the BC is likely to be broadened by bulk motion, such as infalling gas in the accretion funnel or rotation in the region coupling the inner disk to the stellar magnetic field.

3.2. Spectral Lines for CTTS

The permitted emission lines in the spectra of classical T Tauri stars (CTTS) contain a wealth of untapped information on the complex region where the stellar magnetosphere interacts with the accretion disk. Historically one of the defining characteristics of CTTS is a distinctive set of optical emission lines, cited as resembling the spectrum of the solar chromosphere (Joy 1945, Herbig 1962). The most prominent lines are from the hydrogen Balmer series and Ca II H & K, accompanied by a rich array of metallic features including permitted lines of Fe I , Fe II , He I, He II, Ti II, Na I, Ca I, plus forbidden lines of [O I], [S II] and [N II]. In the last decade, studies of the Balmer and forbidden lines have elucidated some of the kinematic activity in these accretion disk systems.

The Balmer profiles in CTTS suggest the presence of magnetic funnel flows, created as the stellar magnetosphere truncates the inner disk and redirects the accretion flow along magnetic trajectories terminating in accretion shocks on the stellar surface (Bertout 1989, Königl 1991, Edwards et al. 1994[EHGA], Hartmann, Hewett & Calvet 1994[HHC], Muzerolle, Calvet & Hartmann 1998[MCH]). At the same time, the blueshifted absorption features commonly seen at Hα indicate high speed winds which must originate from either the star or the very inner accretion disk. By tens of AU the outflows become highly collimated into jets, which radiate in shock-excited forbidden lines (Kwan & Tademaru 1988, Hartigan, Edwards & Ghandour 1995[HEG], Hirth, Mundt & Solf 1997).

The stellar magnetosphere is also implicated in spinning down the central star, thereby accounting for the small angular velocities which characterize CTTS photospheres (Edwards et al. 1993, Bouvier et al. 1993, Bouvier et al. 1995). Together these phenomena have been interpreted as indicating that the stellar magnetosphere mediates the disk accretion process and plays a fundamental role in the angular momentum evolution of the star/disk system (Königl 1991, Ostriker & Shu 1995, Ghosh 1995, Li, Wickramasinghe & Ruediger 1996, Armitage & Clarke 1996, Paatz & Camenzind 1996). Considerable ambiguity remains with this interpretation, however, where key unresolved issues include how the stellar magnetosphere is coupled to the disk, how stellar spin-down is achieved, and whether open field lines from the stellar magnetosphere or from a disk magnetosphere are the primary agent launching the outflows (Shu et al. 1994, Najita & Shu 1994, Camenzind 1997, Safier 1997).

This work provides additional insight into the complex star/disk interaction region, where funnel flow and outflow presumably originate. This chapter examines the plethora of permitted Fe I and Fe II lines in the optical spectrum of one high

accretion rate star, DR Tau, with the goal of elucidating any systematic behavior of the line profiles, and providing estimates of physical conditions, including optical depth, column density, and kinetic temperature, in the Fe line formation region.

Iron emission in CTTS was first mentioned by Joy (1945), who noted the similarity to the solar chromospheric spectrum, which is dominated in the optical by Fe I lines. The complex term structure of the Fe atom due to the incomplete 3d shell and the mixing of states caused by the frequent departures from any pure coupling scheme conspire to produce a rich array of emission lines at ultraviolet, optical and infrared wavelengths. In neutral and once ionized iron, the large number of low-lying ($\lesssim 6$ eV), closely spaced ($\lesssim 0.05$ eV) energy levels within spectroscopic terms of alternating parity allows a large number of permitted transitions to be excited by collisions. This fact and the relatively low energy needed for collisional excitation make Fe I & Fe II emission an important cooling agent at low temperatures ($T \lesssim 10^4$ K).

The strength of Fe I (43) fluorescent emission led Herbig (1962) to include it as one of the defining characteristics of a CTTS. An early analysis of the fluorescent Fe lines identified Ca II H or Hϵ as the pumping transition and established the range of electron densities that favor fluorescent Fe emission in an optically thin envelope (Willson 1974, Willson 1975). Later, the fluorescent Fe I lines in the CTTS RU Lup were used to estimate hydrogen and electron densities under LTE conditions with an escape probability approximation (Lago 1982).

While Fe emission is in principle a promising diagnostic of physical conditions and a potential probe of the inner disk environment, the study of iron in CTTS is also beset with a number of difficulties which have hindered past investigators. Factors that complicate the analysis include the photospheric spectrum underlying the emission lines, the severity of line blending from neighboring metallic features,

and the relative weakness of many of these lines. Furthermore, until recently, large uncertainties in atomic transition probabilities hampered detailed analyses of Fe in astrophysical spectra.

Many of these problems are surmounted in this investigation, where (1) we use the most recent compilations of Fe transition probabilities, with uncertainties $\lesssim 10\%$ in Fe I and $\lesssim 25\%$ in Fe II (Nave et al. 1994, Giridhar & Arellano Ferro 1995); (2) we employ high resolution echelle spectra from the CTTS samples described in EHGA and HEG which have the stellar photospheric features and continuum veiling removed, leaving uncontaminated residual line profiles; and (3) we focus on DR Tau, a CTTS which displays a rich metallic spectrum dominated by Fe I & Fe II lines but whose Fe lines are half as broad as those of other highly veiled objects in the spectroscopic sample, thereby minimizing blends due to overlapping line wings and allowing many more transitions to be analyzed. One drawback to the current data set is the non-simultaneity of our 3 blue ($\sim \lambda\lambda$4000-4950 Å) and 4 red ($\sim \lambda\lambda$5000-6800 Å) spectra, so that some of the potentially most sensitive line ratio diagnostics cannot be employed. Nevertheless, we explore here the possibilities inherent in the study of Fe lines as diagnostics of CTTS accretion, and urge that new data be obtained that will fully utilize the information available from these lines.

The star selected for the first phase of this study, DR Tau, is one of the brightest and most frequently observed CTTS. Its optical continuum veiling, which is attributed to luminosity from an accretion shock at the stellar surface, is large and variable, with values in the literature ranging from ~ 0.7 to 20 times the stellar continuum flux (Basri & Batalha 1990, Guenther & Hessman 1993,HEG,Hessman & Guenther 1997). Corresponding mass accretion rates are somewhat uncertain due to the difficulty in assessing the extinction to this source and its significant

variability, but are always at the high end of accretion rates derived for CTTS, with estimates ranging from $\dot{M}_{acc} \sim 10^{-7}$ to 10^{-5} $M_\odot$ yr^{-1} (Bertout, Basri & Bouvier 1988, Basri & Bertout 1989, Kenyon et al. 1994,HEG). Spectroscopic evidence for magnetospheric funnel flows, in the form of inverse P Cygni profiles in upper Balmer lines, Na D, He I and Fe II are also commonly reported in studies of DR Tau (Bertout et al. 1977, Appenzeller et al. 1980, Krautter & Bastian 1980, Guenther & Hessman 1993, EHGA, HHC, Smith et al. 1997). Additionally, the near infrared spectral energy distribution of DR Tau was one of the earliest CTTS to be modeled by a magnetospherically truncated inner disk, with a hole size of ~ 5 R_* (Bertout, Basri & Bouvier 1988, Kenyon et al. 1994).

The spectroscopic data for DR Tau and the identification of 62 unblended Fe I and Fe II lines are presented in §3.3. An empirical examination of the unblended Fe profiles is presented in §3.4, elucidating the basic kinematics of the Fe line formation region. Pairs of lines which share a common upper level are identified in §3.5, and they are used to derive physical conditions via application of an escape probability analysis. A discussion of the results is presented in §3.6 and the conclusions are presented in §3.7.

3.3. The Spectra

The 7 echelle spectra of DR Tau used for this study are taken from a data set which was the basis for two previous publications focussed on Balmer and forbidden lines in 32 CTTS and 10 weak emission T Tauri stars (EHGA and HEG). All the spectra were taken with the 4 meter Mayall telescope at KPNO with a velocity resolution of $\sim$12 km s^{-1}. The spectra cover two wavelength regions, which are taken non-simultaneously; the 4 red spectra were obtained on Jan 7 & 10, 1988,

Nov 30, 1988 and Jan 17, 1990, with a wavelength coverage from $\lambda\lambda$5000-6800 Å and the 3 blue spectra were obtained on Nov 20, 1988, and Dec 1 & 2, 1992, with a wavelength coverage from $\lambda\lambda$4000-4950 Å. The grating settings vary somewhat among the runs and are tabulated explicitly in Table 6. The data reduction for these spectra, including evaluation of the residual emission line profiles and determination of the veiling, is fully described in the two previously published papers.

Determination of the residual emission line profiles begins with the selection of a photospheric template of similar spectral type (K7/M0 for DR Tau), and the CTTS spectrum is then simulated by adding a constant monochromatic flux to the template over a small (about 80 Å) region, until the depths of the artificially veiled photospheric features match those of the T Tauri star. Residual profiles result from the subtraction of the artificially veiled template from the observed T Tauri star spectrum, revealing emission lines free of distortion by the underlying photosphere. This procedure gives unprecedented sensitivity in defining weak emission features in T Tauri spectra, allowing us to study Fe line profiles with equivalent widths as low as 0.1 Å. The weakest lines measurable in the spectra depend on the S/N, which ranges from 50 to 75 in the continuum, with resultant detection limits in equivalent width of $\sim$ 0.02 to 0.05 Å.

The optical continuum veiling flux is also determined by this procedure. It is parameterized by r_λ, the ratio of veiling emission to photospheric radiation at $\lambda = 5700$ Å (r_R) for our red spectra and at $\lambda = 4500$ Å (r_B) for our blue spectra. Measured veilings for the 7 spectra studied here range from $6 \leq r_R \leq 20$ and $8 \leq r_B \leq 13$, and were originally reported in EHGA and HEG. Table 6 identifies the date and corresponding veiling for each observation of DR Tau; we refer to each spectrum by r_λ rather than the date, since the time coverage is infrequent and intermittent.

3.3.1. Identification of Unblended Iron Lines

The strongest lines in our optical spectra of DR Tau are from the hydrogen Balmer series, with equivalent widths 1.5 to 2 orders of magnitude larger than those of other lines. After Hα, the next strongest lines in the red spectra are from He I λ5876 and λ6678. Then follow Fe II (42), the Mg I (2) triplet and the Na I doublet, and [OI] λ6300. The red spectra also include numerous lines of Fe II and Fe I , plus [OI] λ5577 and other forbidden lines from [SII] and [NII]. In the blue spectra, after the Balmer lines, Fe II (42) are the strongest features, followed by numerous lines of Fe II and Fe I , He I, Ti II, Cr II, Ni I and He II. The most abundant optical features, however, are from Fe. The optical Fe lines share upper levels with many UV lines, which are expected to be very strong. As a group the Fe lines likely constitute an important coolant in CTTS.

The total number of Fe lines we identified in DR Tau is approximately 150, with 70 Fe I and 30 Fe II transitions identified in the red and 27 Fe I and 25 Fe II lines in the blue. No Fe III or forbidden line transitions are observed.

The full suite of ~150 Fe I and Fe II lines are characterized as follows:

- Fe I lines in the red spectra arise from 14 multiplets (1, 15, 16, 36, 37, 62, 66, 111, 168, 169, 207, 268, 686, 816) spanning excitation energies that range from 2.4 to 5.6 eV above ground. Most concentrate in 3 clusters at $\sim$ 3.3, 4.4, and 5.6 eV. The largest oscillator strengths are from transitions in multiplets 686 & 816 with Einstein $A_{ij} \sim 10^7$ - 10^8 s^{-1}.

- Fe I lines in the blue spectra arise from 6 multiplets (2, 39, 41, 42, 43, 68) with excitation energies from 2.8 to 5.0 eV above ground. Again, most concentrate in 3 clusters at 2.8, 4.4 and 5.0 eV. The largest oscillator strengths are from transitions in multiplets 41, 42 and 43, with A_{ij} values of $\sim 10^7$ s^{-1}.

- Fe II lines in the red spectra arise from 8 multiplets (40, 41, 42, 46, 48, 49, 55, 74) with upper levels at energies between 4.8 and 5.8 eV above ground. Among them the strongest transitions occur in multiplets 42 and 49, with A_{ij} of $10^6 - 10^7$ s^{-1}.

- Fe II lines in the blue spectra arise from 5 multiplets (27, 28, 37, 38 & 42) with upper levels at energies 5.4 and 5.6 eV above ground. The strongest transitions occur in multiplets 27, 38 and 42 with A_{ij} values of $10^6 - 10^7$ s^{-1}.

- The majority of the observed Fe I transitions decay to metastable levels between 0.0 and 2.6 eV, except for those from multiplets 686 and 816, which decay to non-metastable levels between 3.3 and 3.7 eV above ground.

- The Fe II lines decay to metastable levels between 2.6 and 3.9 eV above the ground state.

Unfortunately the majority of the ~150 Fe lines in our spectra are blended with neighboring features, rendering them ineffective as probes of the kinematic and physical conditions in DR Tau's Fe line formation region. After careful examination, we identified a total of 62 unblended Fe lines for further study; they are listed in Tables 7 and 8. The identification of blends is straightforward when the overlapping transition is resolved, in which case the resultant distorted profiles are readily distinguished. The identification of unresolved blends is more laborious, and requires use of the solar photospheric spectrum as a reference (Moore, Minnaert, & Houtgast 1966). Additional transitions from the parent multiplet of the suspected blending line can be found from the solar spectrum and those with comparable or larger A_{ij} as the suspected blend are used to estimate the blend's relative contribution in the CTTS spectrum. If such transitions are too weak to be detectable in the CTTS spectrum, the blend contribution is deemed to be unimportant. The most

common blends, in order of decreasing incidence, are due to Fe I , Fe II , Ti II, Cr II, Ti I, Cr I and Ni I.

The final identification of 62 unblended Fe features include 35 red Fe I lines (from multiplets 15, 16, 37, 62, 111, 168, 169, 207, 268, 686 & 816), 9 red Fe II lines (from multiplets 42, 46, 48, 49, 55 & 74), 9 blue Fe I lines (from multiplets 2, 39, 41, 42, 43 & 68) and 9 blue Fe II lines (from multiplets 27, 37, 38 & 42). The 62 unblended lines are tabulated in Tables 7 and 8, along with their atomic parameters and observed emission equivalent widths. These unblended lines still include a wide range of Einstein A_{ij} values and excitation potentials, and will form the basis for the rest of this chapter.

3.3.2. Comparison with other Line Profiles

It is informative to compare the profiles of the Fe lines with those exhibited by other strong emission features at the same epoch. Figure 19 presents simultaneous profiles of Hα, He I λ5876, Fe II (49) λ5276 and Fe I (15) λ5397 from the red spectra and Figure 20 presents simultaneous profiles of Hβ, Hγ, Fe II (37) λ4629 and Fe I (43) λ4064 from the blue spectra.

The Balmer lines, some of which appear in EHGA, are typical of those observed in DR Tau (Krautter & Bastian 1980, Hartmann 1982, Mundt 1984, Aiad et al. 1984, Appenzeller, Reitermann & Stahl 1988, Isobe, Norimoto & Kitamura 1988, Hessman & Guenther 1997). They are characterized by broad wings ($\pm$ 500 km s^{-1}), blueshifted absorption features arising in outflowing gas, and occasional inverse P Cygni (IPC) structure in the upper Balmer lines arising in infalling gas, presumably in the magnetic funnel flow. A deep central absorption feature, whose origin is not yet known, is also prominent in the upper Balmer series (see Kwan 1997 for recent thoughts on this component).

In contrast to the hydrogen lines, the helium and other metallic profiles in DR Tau are several hundred km s^{-1} narrower than the Balmer lines, and they lack the multiple absorption components (note a factor of two change in velocity scale between the Balmer and metallic lines in Figures 19 and 20). However, the metallic lines themselves display an array of profile types, most notably a variety of line widths, as illustrated by the decreasing widths from He I λ5876 to Fe II (49) λ5276 to Fe I (15) λ5397 in Figure 19. Several authors have characterized the metallic profiles as composite, consisting of a narrow central peak (the narrow component; NC) and a broad pedestal (the broad component; BC) (Appenzeller, Reitermann & Stahl 1988, Hamann & Persson 1992, Batalha et al. 1996, Edwards 1997). In some lines, such as He I, these two components are quite distinctive, but in others, such as Fe I , they can combine to produce a triangular-shaped profile.

We observe IPC structure in several metallic lines in one of our red epochs and in two of our blue ones. In the red, at the lowest veiling state, $r_R = 6$, IPC features are seen in He I, Mg I, Na I and the strongest lines of Fe II (multiplets 42, 48 & 49). In the blue, at $r_B = 8$ & 13, IPC structure is observed in the upper Balmer and the strongest Fe II lines (multiplets 27, 38 & 42; not shown in Figure 20). The vast majority of the Fe emission lines do not show redshifted absorption features, although the broad component is often slightly blueshifted, as would be expected from magnetospheric infall.

In order to interpret the metallic line profiles in CTTS spectra, it is imperative to quantify their morphology, and to determine whether the apparent composite structure of these lines arises in two distinct regions, as suggested by Hamann & Persson (1992) and Batalha et al. (1996), or whether the profiles result from the geometrical projection of velocity vectors from a single region, such as a funnel flow (Hartmann, Hewett & Calvet 1994).

3.4. Fe Profile Morphology in DR Tau

This section quantitatively explores kinematic structure for Fe I and Fe II profiles in DR Tau, and provides support for the interpretation that permitted metallic lines in CTTS arise in two physically distinct emission regions. This analysis can be extended to more lines in DR Tau and more CTTS, as seen in chapter 2.

The most obvious difference among Fe line profiles in any given spectrum of DR Tau is the range of line widths. Closer inspection reveals a relation between the Fe profile width and the strength of that line. A similar effect has been previously reported for Fe lines in CTTS RU Lup (Boesgaard 1984). This is illustrated in Figure 21, where 4 Fe I profiles from the $r_B = 8$ spectrum are displayed. As the equivalent width progresses from 0.03 Å to 0.9 Å the FWHM increases from 26 to 67 km s^{-1}. Figure 22 shows this behavior as characteristic of all the unblended Fe lines in our spectra. The figure plots the FWHM of an Fe line against its equivalent width and demonstrates that as the W_λ progresses from $\sim$ 0.05 to $\sim$ 0.5 Å, the FWHM increases by more than a factor of three, from $\sim$20 to between 70 to 90 km s^{-1}, and remains roughly constant thereafter, up to the strongest line ($W_\lambda \sim 1$ Å in red or $\sim$ 3 Å in blue). Weaker Fe lines display a different profile morphology than stronger Fe lines. This is clearly demonstrated by fitting each profile with a single function. The fitting procedure uses a chi-squared minimization to evaluate the best definition of the profile according to 3 fitting parameters: shape (β), width (δ), and velocity centroid (μ). The fitting function is:

$$f(x) = e^{-\ln 2\,(|x-\mu|/\delta)^\beta}.$$

When functions of this form are fit to the unblended Fe profiles, we find that the shape parameter evolves from Gaussian (e^{-x^2}; $\beta = 2$) to exponential (e^{-x}; $\beta = 1$) as the line increases in W_λ from < 0.1 Å up to several Å.

The large line widths of Fe likely arise from bulk kinematic motions. Then the dissimilarities in Fe line widths and profile shapes suggest that more than one kinematic regime may exist, with the emitting gas characterized by differing Fe I/Fe II abundance ratio and physical conditions. This possibility leads us to try the next simplest fitting procedure and to separate each line into two components to see if the variety of line profiles can be more succinctly described. Accordingly, we fit each line profile with two Gaussian components ($\beta = 2$), and iterate to find the component widths (δ_1 and δ_2) and velocity centroids (μ_1 and μ_2) which produce the best fit. In this case the fitting function has the form:

$$f(x) = \alpha\, e^{-\ln 2\,(|x-\mu_1|/\delta_1)^2} + (1-\alpha)\, e^{-\ln 2\,(|x-\mu_2|/\delta_2)^2}$$

where α gives the relative peak amplitude of the two components.

A comparison of both fitting procedures, a single component fit with a "free" shape parameter and a two component fit with forced Gaussian shapes, is illustrated in Figure 23 for an Fe I line with a FWHM of 30 km s^{-1} and an W_λ of 0.3 Å, and an Fe II line with a FWHM of 59 km s^{-1} and an W_λ of 0.4 Å. Both lines are fit equally well by either a single function with an exponential form or by the sum of two Gaussian components. Note that the two Gaussian components naturally define a narrow and a broad component (NC & BC), but that the relative contribution of the two components differs between the Fe I and Fe II profiles. The relative amplitudes of the two components in each profile are given by α, and 1-α, which we rename α_{NC} and α_{BC} for clarification. In this comparison, $\alpha_{NC} = 0.6$ for the Fe I line and $\alpha_{NC} = 0.35$ for the Fe II line.

While both approaches yield equally good fits for any individual line, what distinguishes the two component Gaussian fitting procedure is that the derived parameters of each component (width and velocity centroid) are found to be highly

consistent, not only for all the Fe lines in a given spectrum but also among all observing epochs. This uniform set of parameters for the *NC* and *BC* is illustrated in width of an Figures 24 and 25. The widths of both the *NC* and *BC* are displayed as a function of line strength for all 7 observing epochs in Figure 24. Remarkably, the FWHM found for the *NC* averages $22 \pm 4\,\mathrm{km\,s^{-1}}$ for all Fe profiles among 6 of the seven observing epochs. (The one exception, which will be discussed below, is from the spectrum $r_B = 9$). The *BC* is not detectable in the weakest lines, which are best fit by single Gaussian, but for $W_\lambda > 0.1$ Å the *BC* is described by a FWHM which averages $102 \pm 7\,\mathrm{km\,s^{-1}}$ in 6 of the 7 observing epochs (the exception is the same spectrum, $r_B = 9$, discussed below).

The centroid velocities for each component, illustrated in Figure 25, also display a remarkable uniformity among all the lines and all but one observing epoch ($r_B = 9$). The *NC* is always centered on the photospheric velocity to within $\pm$ 5 km s^{-1}. Most of the time the *BC* is slightly blueshifted, by 5 to 10 km s^{-1}, and at any epoch the *BC* centroid velocity shifts are found to be similar among all Fe lines in the spectrum.

The exception to the uniform set of parameters derived for the *NC* and *BC* is from the blue spectrum with $r_B = 9$. This spectrum is unique in that the Fe lines are a factor of two stronger in W_λ than those from the other two blue epochs. While the formal chi-squared search for a two component fit yields *NC* and *BC* widths a factor of 1.5 to 2 times greater than those for the 6 other observing epochs, we attribute this to a very small contribution from a 20 km s^{-1} wide *NC* at this epoch. Indeed, if we force the *NC* to a width of 20 km s^{-1} and center it on the line peak, a search for the best parameters for the *BC* not only produces acceptable fits to the profiles but results in *BC* widths averaging 110 $\pm$ 10 km s^{-1} among all the Fe lines in this spectrum. Although no photospheric lines are detected in this heavily veiled

spectrum, the resultant BC centroids lie within -4 ± 3 km s^{-1} of the NC centroids. These BC parameters are fully consistent with the parameters derived for the other observing epochs, and we attribute the failure of the chi-squared search to find the same parameters to the very small contribution from the NC at this epoch. This is illustrated in Figure 26, where both the free and the constrained NC fits for two representative lines from the $r_B = 9$ epoch are shown. It can be seen that the NC and BC parameters derived for the other 6 observing epochs are consistent with the data, but the weakness of a 20 km s^{-1} wide NC ($\alpha_{NC} \sim 0.2$) for the $r_B = 9$ spectrum leads the chi-squared search to a different solution space. We thus adopt the interpretation that the parameters describing the NC and BC apply at all 7 observing epochs.

The consistent set of profile parameters for NC and BC emission supports the notion that there are two distinct regions of Fe emission in DR Tau. We have made no attempt to fit the occasional IPC redward absorption that is sometimes present in the strongest Fe II lines. Typically this feature is redward of BC emission wings, and the consistency in the fit parameters found among the entire set of unblended Fe lines suggests that the two-component fit is a reasonable approximation to the Fe emission profiles.

In the next section, we use the different ratios of NC to BC emission found among unblended Fe lines to estimate the extent to which the physical conditions in these two regions differ. To obtain a consistent determination of the relative amplitudes and equivalent widths for the two components for this analysis, we have refit each line with the following restrictions: (1) the NC width is set at 20 km s^{-1} and a velocity at rest with respect to the line peak; and (2) the BC width is set at 100 km s^{-1}, and its centroid velocity is a free parameter. In all cases, the normalized peak amplitude of one of the two Gaussian components is also a free parameter

($\alpha_{NC} + \alpha_{BC} = 1$). In the remainder of this chapter, the peak amplitudes and the equivalent widths of the two kinematic components will refer to those derived from these "forced" fits, rather than the unconstrained fitting shown in both Figures 24 and 25.

The observed behavior of the Fe profiles, with a systematic relation between the strength of a line and its width and profile morphology, is thus accounted for by differing amplitudes of the *NC* and *BC* among lines of differing excitation and ionization. The nature of this relation is illustrated in Figure 27, where the two Gaussian component fits are shown for 4 Fe I lines from the $r_B = 8$ spectrum. There is a progression in the proportion of *NC* to *BC* emission, from the weakest line, dominated by the *NC* ($\alpha_{NC} = 1.0$), to the strongest and broadest line with the smallest proportion of *NC* to *BC* emission ($\alpha_{NC} = 0.3$). This trend is characteristic of all of our 62 unblended lines for all observing epochs, as shown in Figure 28, which plots the *NC* amplitude, α_{NC} (evaluated with the "forced" fits), as a function of line strength. The weakest lines have $\alpha_{NC} \sim 1.0$, and as line strength increases α_{NC} decreases, so that the strongest lines are typically characterized by $\alpha_{NC} \sim 0.3$, except in the $r_B = 9$ spectrum, where the strongest lines have $\alpha_{NC} \sim 0.1$.

We see no link between the Fe profile morphology and the continuum veiling. In our red spectra, the veiling varies by a factor of 3, but it is fairly constant in our blue spectra. The Fe profile morphology for any given line varies by $< 40\%$ in the ratio of *NC* to *BC* equivalent widths, although the total emission equivalent widths for a given line vary by a factor of 2 or more in our spectra. The lack of any correlation between the Fe lines and the veiling is consistent with the recent study of Hessman and Guenther (1997), who find that the line flux in CTTS varies independently of the veiling.

3.5. Derivation of Physical Quantities from Fe Lines

For Fe, the availability of transitions originating from the same upper level provides an opportunity to compare the intensities of these lines without concern for how their common upper level is populated. This eliminates the need to perform excitation calculations and allows one to draw conclusions without the uncertainties inherent in adopting input parameters, such as collisional cross sections. In this section we use the intensity ratios of such lines to evaluate the optical depth, column density, and kinetic temperature in the Fe line formation region and to search for physical differences between the two kinematic components. We begin by comparing observed line ratios with their optically thin values, and then employ the Sobolev LVG approximation to interpret the observed differences between *NC* and *BC* emission. While the method described here is in principle an excellent diagnostic of the physical conditions in the Fe line formation region of DR Tau, restrictions of the current data set limit the extent to which we can draw firm conclusions.

3.5.1. Relative Line Opacities From Line Pairs with a Common Upper Level

The intensity ratio of two lines originating from the same upper level gives a direct measure of line opacity. Each common upper level pair comprises a weak and a strong member, a label which refers to the relative magnitude of their spontaneous emission or A_{ij} rates. By examining intensity ratios from such line pairs, comparisons can be made of the relative optical depth of the two kinematic components.

An ideal pair to use for this type of analysis would be Fe I (41) λ4405 and Fe I (168) λ6394, with an A_{ij} ratio of 42 and W_λ's $\sim$ 0.5 and 0.05 Å, respectively.

Unfortunately the members of this pair fall on two different grating settings with the KPNO echelle, and thus were not observed simultaneously by us. Although the non-simultaneity invalidates their use in our analysis, we show the profiles of each pair member in Figure 29 in order to illustrate how different the proportion of NC to BC emission can be between lines from a common upper level. The contrast between the profiles is dramatic, with the NC dominating the profile of the weaker transition (Fe I (168) λ6394; α_{NC} ~0.9) and the BC dominating the profile of the stronger transition (Fe I (41) λ4405; α_{NC} ~0.2). This distinction can be further quantified by the ratio of NC/BC equivalent width for each line, which differs by approximately an order of magnitude between the weak and the strong line. This contrast is inherent in the Fe line formation region, and cannot be attributed to time variability, as demonstrated by the near constancy of the profile morphology of each line over all observing epochs.

The current dataset requires restricting the comparison of common upper level lines to pairs that are simultaneously observed in either the red or blue spectral region. In spite of the large number of unblended lines, the number of pairs meeting this criterion is limited to 6. Five pairs are from Fe I , with 3 from Fe I (15) in the red, 1 from Fe I (168) in the red, and 1 from Fe I (43) in the blue. The fluorescent condition of the Fe I (43) multiplet does not affect this analysis since the mode of exciting the upper level is not relevant. The single Fe II pair is in the blue, formed of lines from two multiplets, one from Fe II (27) and one from Fe II (38).

The proportion of NC to BC emission among these 6 pairs follows the pattern we have seen for the 62 unblended Fe lines and for the non-simultaneous Fe I (41)- Fe I (168) pair, with the BC emission becoming increasingly dominant in the stronger lines. The profiles for these 6 pairs are shown in Figures 30 and 31, with pair members in adjacent panels.

Unfortunately, several factors impose limitations when using these 6 pairs for our analysis. (1) The ratios of the spontaneous transition rates only span factors of 7 to 17 among the 6 pairs, limiting their sensitivity as discriminants of physical conditions such as optical depth and column density. (2) As a result of the modest range of A_{ij} ratios, the contrast in the profile morphology between the weak and the strong line in a pair is less dramatic than that in the non-simultaneous pair discussed above. (3) The small total W_λ of the weak line in each pair results in low S/N in the line wings and makes the extraction of the BC equivalent width somewhat uncertain. Hence, while the method we describe is in principle an excellent diagnostic, the limitations from this particular data set mean that our analysis should be considered illustrative rather than definitive.

We can quantify the comparison between the weak and strong lines in a pair by evaluating the NC/BC equivalent width ratio for both lines. This is illustrated in the upper panel of Figure 32 for the cases where both kinematic components could be reliably extracted for both the weak and strong line. In the figure the ratios $W_\lambda(NC/BC)_{weak}$ and $W_\lambda(NC/BC)_{strong}$ are plotted as a function of A_{ij}, with members of a pair joined by a dashed line. A larger ratio of NC to BC emission for the weaker transition is seen in most pairs, although the maximum contrast is typically a factor of two, rather than the order of magnitude found for the non-simultaneous blue/red Fe I pair with an A_{ij} ratio of 42.

Under optically thin conditions, the intensity ratio of the weak to the strong line in the pair should be proportional to the ratio of their respective A_{ij} values. In the absence of spectrophotometric data, we will substitute equivalent width ratios for intensity ratios. Although some pair members can be separated from each other by several hundred Å, adopting a 10^4 K blackbody to model the heavily veiled continuum of DR Tau incurs errors of $< 5\%$ when using equivalent width rather

than flux ratios. In the lower panel of Figure 32 we compare the equivalent width ratios between pair members, taken separately for the *NC* and *BC*. It can be seen that (1) for most pairs the ratio of the weak to the strong line in both the *NC* and the *BC* exceeds the optically thin value, indicating that in both components at least the stronger line is optically thick; (2) in most cases, the ratios of the weak to the strong lines for the *NC* exceed those for the *BC*, suggesting a greater opacity in the *NC* lines.

3.5.2. Line Opacities and Fe Column Densities from the LVG Approximation

To quantify the opacity and column density of the Fe line formation region, and to determine whether these differ for the *NC* and *BC*, the Sobolev large velocity gradient (LVG) approximation is employed in order to calculate the line opacity and local escape probability. Further, noting that the majority of our Fe I and Fe II lines have metastable lower levels, it is possible to transform the line optical depths into column densities by assuming the metastable levels to be in thermal equilibrium with the ground state and neglecting the population in the non-metastable levels.

The LVG approximation is probably appropriate for describing the *BC* emission, with a FWHM of $\sim$ 100 km s^{-1}. However, for the *NC* emission, with a FWHM $\sim$ 20 km s^{-1}, the LVG approximation may be less applicable. In this case it is likely to give a lower bound to the opacity, since the scaling of the local escape probability with line opacity is similar in the LVG and the static case, but in the static case the intensity ratio of two lines is not a simple ratio of their local escape probabilities.

In the Sobolev approximation, the intensity ratio of two transitions arising from the same upper level is given by:

$$f_{ws} = \frac{\nu_w A_w \beta_w}{\nu_s A_s \beta_s} \tag{3.1}$$

where A is the spontaneous emission rate, β is the escape probability, ν is the transition frequency, and the 'w' and 's' subscripts refer to the weaker and stronger transition in each pair.

If the velocity gradient is isotropic, the escape probability averaged over all directions has the form

$$\beta = \frac{1 - e^{-\tau}}{\tau} \tag{3.2}$$

and the line opacity in the Sobolev approximation is

$$\tau = \frac{hc}{4\pi} \frac{(n_l B_{lu} - n_u B_{ul})}{dv/dl}, \tag{3.3}$$

where n_u, n_l are the upper and lower level population, B_{lu} and B_{ul} are the Einstein stimulated absorption and emission coefficients, and dv/dl is the velocity gradient. Neglecting the upper level population with respect to the population in the lower metastable level, and assuming a thermal distribution in the metastable levels, we obtain:

$$\tau \approx \frac{hc}{4\pi} B_{lu} g_l \frac{e^{-E_l/kT}}{U(T)} \frac{ndl}{dv}, \tag{3.4}$$

where $U(T)$ is the partition function from the metastable levels, n is the total ion number density and E_l is the lower level excitation energy.

The intensity ratio f_{ws} is then a function of two unknowns, the velocity modified column density, $\mathcal{N} = ndl/dv$, and the kinetic temperature T. The left panels of Figures 33 and 34 plot the predicted f_{ws} ratios as a function of $\mathcal{N}$ for T between 4,000 - 20,000 K for each of our 6 common upper level pairs. Comparison of the observed f_{ws} intensity ratio, measured separately for the BC and NC, with the

predicted relations then yields a locus of $\mathcal{N}$, T values which are compatible with the observations.

The theoretical dependence of the flux ratio on $\mathcal{N}$ at a fixed T is governed by the dependence of the escape probability on line opacity (cf. eqs. 1 and 2). In the optically thin limit the escape probabilities for both the weak and strong lines will be unity and f_{ws} will be a constant independent of $\mathcal{N}$ or T. As $\mathcal{N}$ increases the strong line becomes optically thick first, causing f_{ws} to increase. As long as the weak line remains optically thin, f_{ws} will increase as the opacity in the strong line increases, creating the steeply rising part of the curve. Eventually $\mathcal{N}$ increases to the point where the weak line becomes optically thick and f_{ws} again becomes independent of $\mathcal{N}$. The shape of these curves of growth depends only on the line opacities, the effect of temperature being merely to displace the curves along $\mathcal{N}$. As shown in the left panels of Figures 33 and 34, the observed f_{ws} typically falls on the near-linear regime of the curve where the stronger line of each pair is optically thick and the weaker line is optically thin. The observed f_{ws} can thus be translated into an opacity independent of the actual values of $\mathcal{N}$ and T.

In Figure 35 we plot the optical depths derived by this method for each kinematic component against the A_{ij} values. It can be seen that the opacities range from about 0.1 to 10 among the lines observed. However, as explained below, we have reason to doubt the applicability of these values to the blue Fe I (43) multiplet, which may have opacities considerably higher than indicated. The figure also suggests that the optical depth of the *NC* exceeds that of the *BC* by a factor of 2-4 in each line, consistent with the trend inferred from the comparison of the observed line ratios with their optically thin values shown in Figure 32.

Estimating the column density, which is more sensitive to temperature, proceeds as follows. An observed f_{ws} dictates a theoretical locus of $\mathcal{N}$ and T values, as shown

in the middle panels of Figures 33 and 34. In the allowed loci, $\mathcal{N}$ initially decreases, then increases, with increasing kinetic temperature, so that a given $\mathcal{N}$ corresponds to two possible values of the temperature T. This behavior occurs because a given f_{ws} on the rising portion of the curve of growth fixes the opacity in the strong line, as explained earlier, so that Equation 4 simplifies to $\mathcal{N} \propto U(T)/e^{-E_l/kT}$. While the partition function $U(T)$ increases with T, the factor $1/e^{-E_l/kT}$ decreases with T and dominates at low temperatures. Therefore, as the temperature initially increases from 4000 K, $\mathcal{N}$ decreases until T is high enough (at a value dependent on E_l) that $U(T)$ dominates the temperature dependence, after which $\mathcal{N}$ increases with increasing T.

The $\mathcal{N}$-T locus which accounts for the observed f_{ws} ratio can be converted to a column density-temperature relation through $N = ndl \approx \mathcal{N}\Delta v$. We adopt a Δv of 100 km s^{-1} for the BC and a Δv of 20 km s^{-1} for the NC, and display the N-T loci corresponding to our observed intensity ratios in the rightmost panels of Figures 33 and 34. In the conversion from the velocity modified column density to a standard column density, the application of the differing Δv for the two components shifts what were distinctly lower values of $\mathcal{N}$ for the BC to values of N that are essentially comparable between the two components. Thus for the temperature regime between 4,000 and 20,000 K, we find no significant difference in the column densities of the two kinematic components, with the caveat that the small linewidth of the NC probably compromises the LVG approximation, so the N we derive provides only a lower bound on the column density of the NC region.

The magnitude of the derived column density depends on the kinetic temperature. However, at all temperatures, we consistently find that the column densities for Fe II are at least an order of magnitude larger than those for Fe I , indicating that Fe II is the dominant ionization state. A discrepancy exists, however, in

the Fe I column densities derived from two different multiplets. Specifically, the column densities from the red Fe I (15) multiplet are consistently an order of magnitude greater than those derived from the blue Fe I (43) multiplet. For example, at temperatures $\sim$ 8,000-10,000 K, the corresponding $N_{FeII} \sim 10^{18}\,\mathrm{cm}^{-2}$, while $N_{FeI(15)} \sim 10^{17}\,\mathrm{cm}^{-2}$ and $N_{FeI(43)} \sim 10^{16}\,\mathrm{cm}^{-2}$. This discrepancy between the two Fe I column densities is far too large to be accounted for by observational uncertainty in the Fe I line ratios. It cannot be attributed to the non-simultaneity of the blue and red spectra, since the discrepancy persists over the 4 red and 3 blue epochs, and similar profile morphology is displayed by these lines at each epoch.

It is more likely that the discrepancy in the Fe I column densities results from a breakdown of the simplifying assumption of isotropy in the velocity gradient. In that case the radiative transfer near the surface of the emission region and along certain directions within the emission region may resemble more the static than the LVG situation. The result is that photons in a line can originate from a range of optical depths, making our characterization of the emission by a single τ erroneous. This error is more severe for the more optically thick line. For this reason, we discount the result on $\mathcal{N}$ or N derived from the Fe I (43) lines which, with A_{ij} values 70 to 2000 times larger than those in Fe I (15), have much larger opacities at the same column density. For example, if we adopt the Fe I opacity and column density derived from the Fe I (15) line pairs, then the corresponding optical depth for the fluoresced Fe I (43) lines would be several hundred. It also means that the τ and N_{FeI} determined from the Fe I (15) lines are only lower bounds. The N_{FeII} we find is also a lower bound, although for the BC it provides the most reliable estimate since the optical depths found are so low, $\lesssim 0.7$.

In summary, application of the LVG approximation to the 6 pairs of available Fe I and Fe II lines indicates that Fe II is the dominant ionization state of iron.

There is a suggestion that the NC is more optically thick than the BC in a given line. The current dataset gives sufficiently large errors in the Fe column densities that distinctions between the NC and BC cannot be discerned. The most solid result of the LVG analysis to this restricted set of common upper level pairs is the estimate for the Fe II column density in the BC, with $N_{FeII} \sim 10^{18}$-$10^{19}\,\mathrm{cm}^{-2}$ for kinetic temperatures in the range from 4000 K to 10,000 K. If one then assumes that most of the Fe is once ionized, this yields an approximate total column density for the BC region of $N_H \sim 3 \times 10^{22} - 3 \times 10^{23}\,\mathrm{cm}^{-2}$.

3.5.3. Kinetic Temperature

In principle, an estimate of the kinetic temperature in the Fe line formation region can be made by continuing the procedure from the previous section, where the comparison of intensities between a pair of lines from a common upper level defines an allowed $\mathcal{N}$-T or N-T locus. By superposing the loci from several line pairs, a simultaneous solution of temperature and column density will follow from their points of intersection. The success of this approach depends on maximizing the difference in excitation energy between line pairs. With our limited data set, the best lines we have are a pair of Fe I (15) lines with $E_{upper} \sim 3.3$ eV and a pair of Fe I (168) lines with $E_{upper} \sim 4.3$ eV. Unfortunately, the small W_λ's in the Fe I (168) pair lead to uncertainties in the $\mathcal{N}$-T locus which are too large to identify a good estimate of the kinetic temperature by this method.

Making use of the fact that the excitation temperature of a collisionally excited line is not higher than the kinetic temperature, a lower bound on T can be roughly estimated. This follows from determining the luminosity of a very optically thick line, assuming an area for the emission region, and calculating the line excitation temperature that would reproduce that luminosity. We restrict ourselves to the

luminosity of the narrow component for this exercise, since this component appears to be optically thicker in any given line. Furthermore, we have a better handle on the emitting area of the NC (see discussion in §3.6), which we assume is between 0.05 and 0.2 of the stellar surface area. In our spectra, the strongest NC transition is Fe II (42) λ4924, and we estimate its luminosity as being 1.2×10^{30} erg s^{-1}, based on our measured equivalent width, the average photometric state of DR Tau from Kenyon et al. (1994), an $A_V = 3.2$ (HEG) and a distance to Taurus of 140 pc. For a NC emission area between $0.05A_*$ and $0.2A_*$ the corresponding lower bound on temperature ranges between ~13,500 to ~ 8400 K.

A third approach provides information on the relative kinetic temperature between the NC and BC regions. It relies on identifying transitions arising from widely different energy levels whose intensities are not sensitive to opacity. We have identified two such lines, described below, but again, in the current data set this pair is observed non-simultaneously. However, since this approach only requires the NC/BC flux ratio for each line, it will be valid as long as the profile morphology is not time variable. The opacity insensitive transitions we have identified for this analysis are Fe I (2) λ4376 and Fe I (686) λ5616, arising from upper levels at 2.83 eV and 5.54 eV, respectively.

The insensitivity to opacity for the Fe I (2) λ4376 line comes from its being the dominant decay channel from its upper level and the estimate that its optical depth is not large. Specifically, its opacity depends on $\mathcal{N}$ and T roughly as $\tau \sim (\mathcal{N}/5.4 \times 10^{10}\ \mathrm{cm}^{-3}\ \mathrm{s})(10^4\ K/T)$, and with $\mathcal{N} \sim 10^{11}$ cm^{-3} s for both the NC and BC (cf. Fig. 33), τ is not more than a few. Since its spontaneous emission rate of $\sim 3 \times 10^4$ s^{-1} exceeds those of other decay routes from the same upper level by a factor of $\geq$50, emission of λ4376 will be the dominant radiative decay process when this level is populated. The additional assumption that collisional de-excitation is

not important, in light of λ4376's large A_{ij} rate and modest optical depth, results in a probability near unity that a λ4376 photon will be emitted following every excitation of the upper level, independent of the opacity.

The insensitivity to opacity for the Fe I (686) λ5616 line, which is the strongest transition from its upper state, comes from the fact that it maintains its optically thin branching fraction independent of the optical depth. The λ5616 line has a large A_{ij} rate of $\sim 2.6 \times 10^7$ s^{-1} and a branching fraction of $\sim$42% in the optically thin limit. The next two most important decay channels from the same upper state are Fe I (553) λ5324, and Fe I (816) λ6400, with A_{ij} rates of 2.1×10^7 s^{-1} and 9.3×10^6 s^{-1}, and branching fractions of 32% and 14.6%, respectively. All of these transitions have non-metastable lower levels at comparable energies, $\sim$ 3.4, 3.3 and 3.6 eV, respectively, which possess large and comparable decay rates ($A_{ij} \sim 1 \times 10^7$ s^{-1}). As $\mathcal{N}$ grows, the opacities of λ5616, λ5324 and λ6400 will be similar and increase slowly and in tandem because of the non-metastable nature of their lower levels. This results in their branching fractions remaining nearly uniform at their optically thin values. Fairly independent of its opacity then, Fe I λ5616 will account for $\sim$42% of the radiative decays from its upper level in both the NC and BC.

For both of these opacity insensitive lines, if collisional excitation is assumed, the line intensity will be determined by the kinetic temperature and the product of the collisional cross-section $\times$ the electron density $\times$ the Fe I number density $\times$ the emitting volume. If the collisional rate constants of the upper states of λ5616 and λ4376 were known, then T_{NC} (T_{BC}) could be obtained directly from the NC (BC) flux ratio between the two lines, provided that simultaneous flux ratios were available. Without knowledge of the collisional rate constants, we can take the NC/BC flux ratio for each profile to eliminate the dependence on collisional cross

section. Then the relative values of T_{NC} and T_{BC} can be compared by taking a ratio of the two separate NC/BC flux ratios, which eliminates the dependency on electron density, the Fe I number density, and the emitting volume. Specifically, this double ratio is given by

$$q = [W_\lambda(NC/BC)_{5616}/W_\lambda(NC/BC)_{4376}] = e^{-(E_{u,\lambda5616}/k - E_{u,\lambda4376}/k)(1/T_{NC} - 1/T_{BC})}$$

where $E_{u,\lambda5616}$ and $E_{u,\lambda4376}$ are the energies of the upper levels of λ5616 and λ4376, respectively, and $E_{u,\lambda5616}$ exceeds $E_{u,\lambda4376}$ by 2.7 eV.

Unfortunately, in our data $W_\lambda(NC/BC)_{5616}$ and $W_\lambda(NC/BC)_{4376}$ are not simultaneous ratios. However, these ratios vary by $< 40\%$ among all our observing epochs, so their average values will still yield a meaningful estimate of q. The average profile for each of these lines is shown in Figure 36, corresponding to an average value of $W_\lambda(NC/BC)_{4376} = 0.23$ and an average value of $W_\lambda(NC/BC)_{5616} = 0.96$, producing a value of $q = 4.2 \pm 1.7$.

Figure 37 illustrates how T_{NC} and T_{BC} depend on q for this pair of opacity insensitive lines. Any value of $q > 1$ requires that T_{NC} exceeds T_{BC}, which is certainly the case for DR Tau. Identifying the magnitude of the difference in kinetic temperature between the two regions requires a priori knowledge of one of them, however. For example, if T_{NC} is 10^4 K, the corresponding T_{BC} will be $\sim$ 6900 K. The result that T_{NC} exceeds T_{BC} is firm, unless the neglect of collisional de-excitation is erroneous. If the NC electron density is sufficiently high that λ4376 becomes collisionally de-excited before λ5616, then the observed value of q can be reproduced with a smaller difference between T_{NC} and T_{BC}, or even require that $T_{BC} > T_{NC}$.

In summary, we have a rough estimate for the temperature in the NC region of between 8000 K to 14000 K. We have evidence that the temperatures in the two

kinematic regions differ, and that T in the NC region exceeds that in the BC region. While the magnitude of the difference cannot be derived without independent knowledge of the temperature in one of the two regions, the BC temperatures that would follow from the above estimate in the NC region are 5900 to 8500 K.

3.5.4. Improving Estimates of Physical Quantities

The techniques outlined above demonstrate that unblended Fe lines in CTTS spectra can be important diagnostics of opacity, column density and kinetic temperature. Derivation of these quantities from an LVG analysis requires comparing simultaneous N, T loci from multiple common upper level line pairs. The sensitivity of this technique depends on: (1) maximizing the ratio of A_{ij} between pair members, which enhances the contrast in the line flux ratio between the weak and the strong line; and (2) maximizing the difference in the lower energy level of the stronger line among different pairs. The latter point follows from the fact that the shape and range of an N, T locus from each pair is determined by the column density and temperature required for the stronger line in the pair to become optically thick. Thus comparison of the N, T loci for two line pairs depends on the comparative behavior of the strong line in each pair. A line that decays to a higher-lying energy level will become optically thick at a different column density and temperature than a line decaying to an energy level closer to the ground state. Therefore two line pairs with a large difference in the energy of the lower level of the strong line are required to produce distinct N, T loci.

Significant improvements in evaluating column densities and kinetic temperatures from Fe line ratios could be achieved from flux calibrated spectra covering a broader range of wavelength than provided in our dataset. In Table 9 we present a list of some of the most suitable common upper level pairs of Fe I and

Fe II lines for determining these physical quantities. We include both optical and ultraviolet lines, which allow the greatest contrast in A_{ij} rates and excitation potentials. The selection criteria are: (a) an optically thin flux ratio for the pair $F = (A_s/A_w)(\lambda_w/\lambda_s) > 10$; (b) a spontaneous emission rate in the weaker line of a pair $A_w > 10^3$ s^{-1} for Fe II and $A_w > 10^4$ s^{-1} for Fe I , which correspond to line equivalent widths ~ 0.04 Å in DR Tau; c) no neighboring lines of comparable or greater strength within $\sim 50\,\mathrm{km\,s^{-1}}$ of line center, as determined from either the optical spectra of DR Tau or the solar UV spectrum. The Fe I and Fe II pairs are ordered by increasing excitation potential of the lower level of the strong line in each pair, which spans $\sim 2.7\ eV$ for Fe I and $\sim 3.2\ eV$ for Fe II . This list of line pairs should provide a starting point for future analysis of Fe lines in CTTS.

An additional benefit to acquiring UV spectra of CTTS would be the ability to assess the luminosity radiated by Fe lines, since the strongest transitions are found in this spectral range (see §3.6). Indeed, the recent compilation of low dispersion IUE spectra of T Tauri stars by Gomez de Castro and Franqueira (1997) clarify that Fe II lines are very abundant in the UV spectra of CTTS.

3.6. Discussion

From an analysis of the Fe I and Fe II profiles in DR Tau we have shown that the Fe emission may arise in two distinct kinematic zones. The most compelling argument for this interpretation is that, at each epoch of observation, the *NC* and *BC* kinematic properties are each described by a uniform set of parameters, thereby resolving the differences among Fe I and Fe II profiles of different intensities in a self consistent manner. In addition, there are indications that the kinematic distinction between the components is accompanied by physical differences.

The implication of the presence of distinct kinematic zones in the Fe line formation region of CTTS accretion disk systems is not yet clear. Preliminary findings are reported for He I lines in 30 CTTS (Edwards 1997) where it is demonstrated that the presence of two kinematic components is also an excellent description of these higher excitation lines. In the context of the magnetospheric accretion model the large linewidths of the *BC* are compatible with velocities expected in a magnetic funnel flow. The tendency for the *BC* to be blueshifted, and the fact that redshifted inverse P Cygni absorption below the veiling continuum, just redward of the *BC* emission, is sometimes seen in our DR Tau spectra in both He I λ5876 and the strongest Fe II lines (see Figure 19) could be accounted for by a funnel flow origin for this component.

As clarified in chapter 2, two component Gaussian fits to the He I lines in DR Tau yields a *BC* linewidth that is twice the width of that found for Fe I and Fe II , with FWHM $= 232 \pm 15\,\mathrm{km\,s^{-1}}$, and a centroid velocity that has twice the blueshift exhibited by the Fe lines: $-29 \pm 9\,\mathrm{km\,s^{-1}}$. In a funnel flow origin, a factor of two difference in *BC* linewidth between He I and Fe would result if the He I lines are formed in the infalling pre-shock gas closer to the accretion shock. There, where the free-fall velocity is the highest, the veiling continuum can more easily ionize He and lead to the production of He I lines via recombination and cascade.

The column densities we derive for the Fe I *BC* are also consistent with an origin in the funnel flow. This follows from (1) the finding that Fe II is the dominant ionization state of iron in the *BC*; and (2) the estimate that $N_{FeII} \sim 10^{18}$-10^{19} cm^{-2} for kinetic temperatures in the range 10,000 K to 4,000 K. If most of the Fe is assumed to be in Fe II , the corresponding hydrogen column density is then $N_H \sim 3 \times 10^{22} - 3 \times 10^{23}\,\mathrm{cm^{-2}}$. This compares favorably with column densities expected in a funnel flow geometry in a high accretion rate CTTS. For example,

the recent multi-level statistical equilibrium calculations to derive hydrogen line luminosities and profiles in magnetic funnel flows, employing a dipole geometry and a disk truncation radius of several R_* (MCH) have column densities $N_H \sim 10^{23}\ cm^{-2}$ for $\dot{M}_{acc} \sim 10^{-7}\ M_\odot\ yr^{-1}$ (James Muzerolle, personal communication).

However, one problem with the current modeling of the magnetospheric funnel flow is that the source of heating needed to produce the assumed temperature is not specified. This problem is particularly acute if the Fe lines, when the UV transitions are included, constitute a luminosity comparable to that in the hydrogen Balmer lines. The Fe lines pose a problem in that these lines are most probably collisionally excited and therefore require local heating, as opposed to the hydrogen lines which can also be produced by recombination and cascade via utilization of the energy in the photon continuum. We propose here an alternative origin of the Fe *BC* emission. It is the boundary layer where loading of the gas from the accretion disk onto the field lines of the stellar magnetosphere takes place. The attractive feature of this scenario is that if this coupling region lies well within the co-rotation radius of the star and disk, dissipation of the gas particle's Keplerian rotational energy before it can co-rotate with the stellar field line and begin its free fall toward the star produces naturally the heating necessary for collisional excitation of the Fe lines. The evolution in the rotational motion of the gas can also produce the observed *BC* linewidth.

The heating in such a boundary layer would also produce hydrogen lines. The relative amount of hydrogen versus Fe emission will depend strongly on the equilibrium temperature reached from the balance between the heating and cooling rates. If this temperature is $\lesssim$7000 K, Fe emission will dominate. Even if the temperature is >7000 K, however, the hydrogen emission produced in this boundary layer would likely only constitute a fraction of the observed Balmer emission, in view of

the presence of other sources of energy, such as the veiling continuum and the heating in the post-shock region of the accretion shock. This equilibrium temperature, however, is not likely to be high enough to produce He I lines, and the He I *BC* would then arise entirely in the pre-shock gas in the funnel flow.

The dynamics of the gas in this boundary layer may be complicated. The dissipation of the kinetic energy of the gas, allowing some gas to fall towards the star along the stellar magnetic field lines may also be accompanied by the ejection of other gas particles from this layer as a means of transporting angular momentum outwards. This ejection of matter may be a source for the outflow that is later collimated into the jet. For either gas infalling along the stellar magnetic field lines or gas ejected out from the boundary layer, the resulting acceleration outward from the disk could account for the small blueshift observed in the *BC* of the Fe lines.

We plan to explore this boundary layer scenario further by calculating the excitation of the Fe I and Fe II UV and optical lines in order to evaluate the total cooling rate produced by the two ions and hence obtain an estimate of the minimum heating rate required, and to compare this with the hydrogen emission rate. If the luminosity from the Fe lines constitutes a significant fraction of the accretion luminosity, then a boundary layer at the interface between the disk and the stellar magnetosphere may turn out to be an important source of line emission in CTTS.

The interpretation of the *NC* is less problematic. Its relatively small linewidth and the fact that it is always observed to be centered on the photospheric velocity suggests that this component is very close to the stellar surface. These kinematic properties would be consistent with either a stellar chromosphere or with emission from the post-shock gas after accreting material has arrived at the star. Formation in the post-shock gas is favored because the Ca II *NC* line flux is correlated with the continuum veiling, r, among a sample of CTTS (Batalha et al. 1996).

A full study of both the *NC* and *BC* emission among a large sample of CTTS and WTTS is in preparation (Beristain, Edwards, Kwan and Hartigan) that lends additional support to this interpretation. We also find that this region displays some complexity. For example in DR Tau the *NC* in the He I lines has a FHWM of $48 \pm 4\,\mathrm{km\,s^{-1}}$ (see Figure 19), which is twice as wide as that of the Fe lines. This could be accounted for by a greater turbulence in the higher excitation region closer to the accretion shock.

The possibility that the *NC* in Fe and He originates in the post-shock gas may affect the interpretation of the Balmer lines in CTTS as well. Although Balmer emission in CTTS has been well modeled as arising in a funnel flow (HHC, MCH), MCH find that contributions from the accretion shock are also required to account for both the small observed $H\beta/H\gamma$ ratios and the Stark-broadened wings at $H\alpha$. Our study of the Fe lines in DR Tau suggests that line radiation from the accretion shock will be kinematically distinct, with small linewidths and at rest relative to the star. Indeed, in many CTTS of low to modest accretion rate, the upper Balmer lines display a profile morphology reminiscent of the Fe lines in DR Tau, with a broad base and a central peak. Further study is needed to determine whether this central peak in the Balmer lines is a signature of the accretion shock, or whether it is formed by gas at low projected velocities in the funnel flow, as predicted by the HHC and MCH models.

3.7. Conclusions

We analyze 62 unblended Fe I and Fe II emission lines from optical echelle spectra of DR Tau, an extreme CTTS with $\dot{M}_{acc} \sim 10^{-6}$ $\mathrm{M_\odot}$ yr^{-1}, in order to probe the region where the stellar magnetosphere interacts with the accretion disk. The

unblended Fe lines span a range of upper excitation potential from 2.4-5.6 eV in Fe I and from 4.8-5.9 eV in Fe II, with spontaneous transition rates spanning a factor of 10^4 for Fe I and a factor of 600 for Fe II .

Our primary conclusions are:

(1) The morphology of the Fe profiles in DR Tau varies systematically with line strength. Line widths increase from a minimum FWHM of $\sim$ 20 km s^{-1} for the weakest lines (W_λ = 0.03 Å) to a maximum FWHM of 70 to 90 km s^{-1} for the strongest lines (W_λ from 0.5 Å to 3.5 Å). The functional form best describing the shape of the line profile evolves from a Gaussian to an exponential form as the W_λ increases.

(2) The progression of the width and shape of Fe profiles in DR Tau with increasing line strength is best accounted for by differing relative contributions from two Gaussian components. The narrow component (NC) has a FWHM of $22 \pm 4\,\mathrm{km\,s^{-1}}$, comparable to the width of the photospheric Li I line, and is centered on the photospheric velocity. The broad component (BC) has a FWHM of $102 \pm 7\,\mathrm{km\,s^{-1}}$, and is frequently blueshifted by up to 10 km s^{-1}. The normalized peak amplitudes of the NC range from 1.0 for the weakest lines to 0.1 for the strongest.

(3) Estimates of opacities and column densities are obtained by comparing observed intensity ratios of lines from a common upper level with values expected from a local escape probability calculation. We find (1) opacities in the NC exceed those in the BC by factors of 2-4; and (2) for the BC, $N_{FeI} \gtrsim 10^{17} - 10^{18}\,\mathrm{cm^{-2}}$ and $N_{FeII} \gtrsim 10^{18} - 10^{19}\,\mathrm{cm^{-2}}$ for kinetic temperatures in the range 4000 K to 10,000 K. The corresponding total BC column density is $N_H \sim 3 \times\ 10^{22} - 3 \times 10^{23}\ cm^{-2}$.

(4) We estimate the temperature in the Fe NC region to lie between $\sim$ 8400 to 14,000 K, assuming that the size of the emitting region is between $0.2A_*$ and $0.05A_*$. The ratio of NC/BC emission from a pair of Fe I lines which are insensitive

to opacity reveals that the kinetic temperature in the NC exceeds that in the BC by several thousand degrees. For example, if $T_{NC} = 10^4$ K, $T_{BC} \sim 7,000$ K.

At present, we can only speculate on the relevance of these two kinematic components in accretion disk systems. In the context of a magnetospheric accretion model, the NC is consistent with an origin in the post-shock gas close to the stellar surface. In contrast, the BC is likely to be broadened by bulk motion, such as infalling gas in the accretion funnel or rotation in the region coupling the inner disk to the stellar magnetic field.

This chapter describes the potential of using Fe lines in CTTS as diagnostics of the inner accretion zone. To fully utilize these lines requires high signal to noise spectrophotometry over as wide a wavelength range as possible. Some of the most promising line pairs for deriving physical parameters require simultaneous optical and ultraviolet coverage, which would provide the largest possible range of Einstein A_{ij} rates between members of a line pair. In addition, the ultraviolet spectrum includes the strongest transitions in both Fe ions, and would thereby allow an estimation of the the total cooling rate due to Fe, which is expected to be substantial.

Table 6
DR Tau Spectra.

Veiling	HJD	λ Range (Å)	Strongest Multiplets Observed	
r_R	2440000+		Fe I	Fe II
20	7170.7	5128 - 6760	15, 37, 168, 169, 686	46, 48, 49, 55, 74
10	7167.8	5130 - 6760	15, 37, 168, 169, 686	46, 48, 49, 55, 74
9	7908.8	5272 - 6760	15, 37, 168, 169, 686	46, 48, 49, 55, 74
6	7495.9	4985 - 6806	15, 37, 168, 169, 686	42, 46, 48, 49, 55, 74
r_B	2440000+		Fe I	Fe II
13	8958.8	4023 - 4970	2, 41, 42, 43, 68	27, 28, 37, 38, 42
9	7485.8	3985 - 4920	2, 41, 42, 43, 68	27, 28, 37, 38
8	8959.8	4020 - 4970	2, 41, 42, 43, 68	27, 28, 37, 38, 42

Table 7
Unblended Fe I lines in DR Tau.

Multiplet	λ (Å)	E_u (eV)	log A_{ij} (s^{-1})	W_λ(Å) $r_R = 6$ $r_B = 8$	9 9	10 13	20
$a^5D - z^7F^o$							
(2)	4375.93**	2.83	4.47	0.25	0.59	0.16	
$a^3F - z^5D^o$							
(15)	5371.49*	3.27	6.02	0.11	0.20	0.30	0.22
	5405.77	3.28	6.00	0.09	0.14	0.21	0.13
	5455.61	3.28	5.78	0.10	0.10	0.19	0.10
	5429.70*	3.24	5.63	0.12	0.21	0.36	0.23
	5397.13*	3.21	5.41	0.11	0.18	0.30	0.15
	5497.52*	3.27	4.80	0.06	0.07	0.09	0.05
	5506.78*	3.24	4.70	0.05	0.07	0.09	0.04
	5501.46*	3.21	4.43	0.05	0.06	0.07	0.04
$a^5F - z^5F^o$							
(16)	5083.34	3.40	4.75	<0.03	...	...	...
	5051.63	3.37	4.71	0.04	...	...	...
	5151.91	3.42	4.38	<0.02	...	0.03	<0.01
	5142.93	3.37	4.37	<0.02	...	...	...
$a^3F - z^3D^o$							
(37)	5341.02	3.93	5.72	0.07	0.11	0.18	0.08
$a^3F - y^5F^o$							
(39)	4531.15	4.22	5.40	0.02	0.09	<0.01	
$a^3F - z^5G^o$							
(41)	4404.75	4.37	7.48	0.39	1.30	0.35	
$a^3F - z^3G^o$							
(42)	4250.79	4.47	7.18	0.06	0.36	0.14	
	4202.03	4.43	6.91	0.20	0.52	0.14	

Continued on Next Page

Table 7 Continued

Multiplet	λ (Å)	E_u (eV)	log A_{ij} (s^{-1})	W_λ(Å)			
				$r_R = 6$	9	10	20
				$r_B = 8$	9	13	
$a^3F - z^3F^o$							
(43)	4045.81	4.55	7.94	0.28	0.78	0.21	
	4063.59*	4.61	7.82	0.90	3.27	0.69	
	4132.06*	4.61	7.07	0.38	1.35	0.26	
$a^3P - y^5D^o$							
(62)	6335.34	4.15	5.15	0.02	0.04	0.06	0.04
	6219.28	4.19	5.10	0.04	0.05	0.04	0.02
	6265.13	4.15	4.84	<0.01	<0.01	0.02	0.03
$a^5P - x^5D^o$							
(68)	4494.56	4.96	6.54	0.03	0.20	0.02	
$a^3P - z^3P^o$							
(111)	6663.45	4.28	5.72	...	<0.02	<0.02	0.02
	6421.35	4.21	5.57	0.03	<0.04	0.04	0.02
$a^3H - z^5G^o$							
(168)	6494.98*	4.31	5.88	0.03	0.07	0.10	0.07
	6393.60	4.37	5.83	0.03	0.03	0.07	0.05
	6593.88*	4.31	4.72	<0.02	<0.06	0.03	<0.04
$a^3H - z^3G^o$							
(169)	6191.56	4.43	5.94	0.03	0.08	0.12	0.08
	6252.55	4.39	5.50	<0.01	0.03	0.03	0.04
$b^3F - y^3F^o$							
(207)	6065.48	4.65	6.03	0.01	<0.01	0.02	0.02
	6230.73	4.55	6.00	0.03	0.04	0.06	0.05
	6200.32	4.61	4.96	<0.01	<0.01	<0.01	<0.01

Continued on Next Page

Table 7 Continued

Multiplet	λ (Å)	E_u (eV)	log A_{ij} (s^{-1})	W_λ(Å)			
			$r_R = 6$	9	10	20
			$r_B = 8$	9	13	
$a^3G - y^3F^o$							
(268)	6592.91	4.61	5.87	...	...	0.12	...
$z^5F^o - e^5D$							
(686)	5615.64**	5.54	7.42	0.02	0.07	0.09	0.06
	5572.84	5.62	7.36	0.02	0.02	0.03	0.02
	5569.62	5.64	7.32	<0.01	0.01	0.02	0.03
	5624.54	5.62	6.87	<0.01	<0.01	<0.01	0.02
	5709.38	5.54	6.33	<0.02	<0.02	0.05	0.02
$z^5P^o - e^5D$							
(816)	6400.00	5.54	6.97	0.03	0.04	0.06	0.06
	6411.65	5.59	6.77	<0.02	<0.02	0.02	0.02
	6408.02	5.62	6.49	<0.01	<0.01	<0.01	0.02

Note.— There are 4 entries for W_λ from the red spectra, and 3 from the blue spectra. Each spectrum is identified by its veiling state, either r_R (columns 7-10) or r_B(columns 7-9). The grating settings for each observing epoch differ somewhat, so that some lines are observable at one epoch but not another, as indicated by ... . Lines comprising common upper level line pairs used in the LVG analysis for opacity and column density estimates is marked with a single asterisk; the two opacity insensitive lines used to estimate kinetic temperatures is marked with a double asterisk. Atomic parameter data for Fe I come from Fuhr, Martin & Wiese (1988); Bard, Kock & Kock (1991); O'Brian et al. 1991; Nave et.al. (1994).

Table 8

Unblended Fe II lines in DR Tau.

Multiplet	λ (Å)	E_u (eV)	log A_{ij} (s^{-1})	W_λ(Å)			
				$r_R = 6$	9	10	20
				$r_B = 8$	9	13	
$b^4P - z^4D^o$							
(27)	4351.76*	5.55	5.67	0.62	2.61	0.85	
$b^4F - z^4F^o$							
(37)	4555.89	5.55	5.32	0.25	1.51	0.37	
	4515.34	5.59	5.32	0.47	1.11	0.20	
	4629.34	5.48	5.16	0.57	1.67	0.56	
	4520.23	5.55	4.93	0.17	0.69	0.28	
$b^4F - z^4D^o$							
(38)	4522.63	5.58	5.88	0.40	1.56	0.31	
	4508.28	5.61	5.83	0.40	1.22	0.31	
	4576.33*	5.55	4.79	0.06	0.41	0.12	
$a^6S - z^6P^o$							
(42)	4923.93	5.41	6.60	1.59	···	1.35	
	5018.45	5.36	6.40	1.52	···	···	···
$a^4G - z^6F^o$							
(46)	5991.37	5.22	3.63	<0.03	0.04	0.11	0.09
	6084.10	5.24	3.48	<0.06	<0.03	0.05	0.05
$a^4G - z^4D^o$							
(48)	5362.86	5.49	4.85	0.23	0.31	0.44	0.30

Continued on Next Page

Table 8 Continued

Multiplet	λ (Å)	E_u (eV)	log A_{ij} (s^{-1})	W_λ(Å)			
				$r_R = 6$	9	10	20
				$r_B = 8$	9	13	
$a^4G - z^4F^o$							
(49)	5276.00	5.55	5.53	0.49	0.66	0.97	0.80
	5197.56	5.62	5.69	0.33	···	0.74	0.50
	5234.62	5.59	5.36	0.48	···	0.95	0.62
$b^2H - z^4F^o$							
(55)	5534.83	5.48	4.57	0.21	0.23	0.39	0.27
$b^4D - z^4P^o$							
(74)	6456.39	5.82	5.23	0.21	0.33	0.57	0.38

Note.—See comments for Table 7. Atomic parameter data for Fe II come from Fuhr, Martin & Wiese (1988); Heise & Kock (1990), and Giridhar & Arellano-Ferro (1995).

Table 9
Desirable Common Upper Level Pairs.

Pair Origin		E_l [c]	λ_s	λ_w	log A_s	log A_w	F [d]
Term [a]	PM [b]	(eV)	(Å)	(Å)	(s^{-1})	(s^{-1})	
Fe I							
z^5D^o	4; 15	0.05	3856	5497	6.66	4.80	106
y^5D^o	20; 62	0.96	3878	6335	6.89	5.15	90
z^3G^o	42; 169	1.49	4202	6192	6.91	5.69	25
y^3D^o	45	1.59	3903	3966	7.32	6.15	15
z^5P^o	60; 106	2.20	8327	8805	5.98	4.23	61
z^5G^o	168	2.42	6495	6594	5.89	4.72	15
z^3G^o	268	2.75	6593	6704	5.74	4.18	37
Fe II							
z^6P^o	uv3; 42	0.05	2333	5019	8.18	6.43	120
z^4F^o	uv35; 37	0.23	2360	4629	7.38	5.11	362
z^6D^o	uv1; uv32	0.55	2626	2732	7.38	4.96	393
z^6P^o	uv61; 5	0.99	2881	3426	6.34	4.11	201
z^4D^o	6	1.70	3211	3167	6.41	5.15	18
z^4D^o	38; 73	2.86	4508	7225	6.00	4.40	64
z^4F^o	49; 57	3.31	5235	5628	5.56	3.18	260

[a]spectroscopic designation of the upper term for each pair.

[b]Parent Multiplets of the strong;weak lines in each pair.

[c]lower level energy of the strong line of each pair.

[d] $F = (A_s/A_w)(\lambda_w/\lambda_s)$; this is the expected flux ratio of the strong to the weak line in the optically thin limit.

Note.— Atomic parameter data are from Fuhr, Martin & Wiese (1988); Heise & Kock (1990); Bard, Kock & Kock (1991); O'Brian et.al. 1991; Nave et.al. (1994) and Giridhar & Arellano-Ferro (1995).

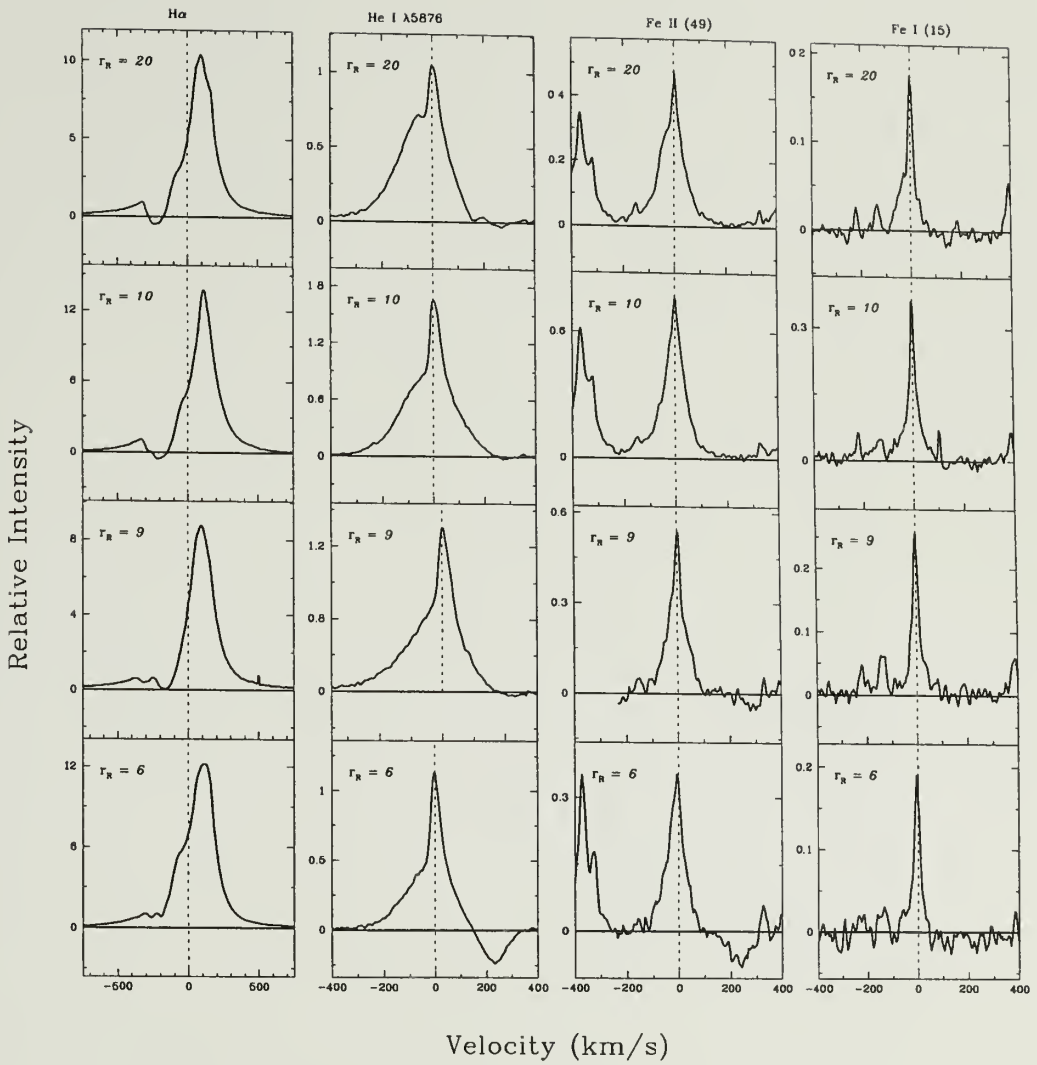

Figure 19. Residual emission profiles are shown for Hα, He I λ5876, Fe II (49) λ5276 and Fe I (15) λ5397 for the 4 red observing epochs, ordered by the magnitude of the veiling at λ5700 Å, r_R. The velocity scale for the Balmer lines is almost twice that for the other lines. The ordinate is in units of the continuum flux and the velocity is measured relative to the photosphere.

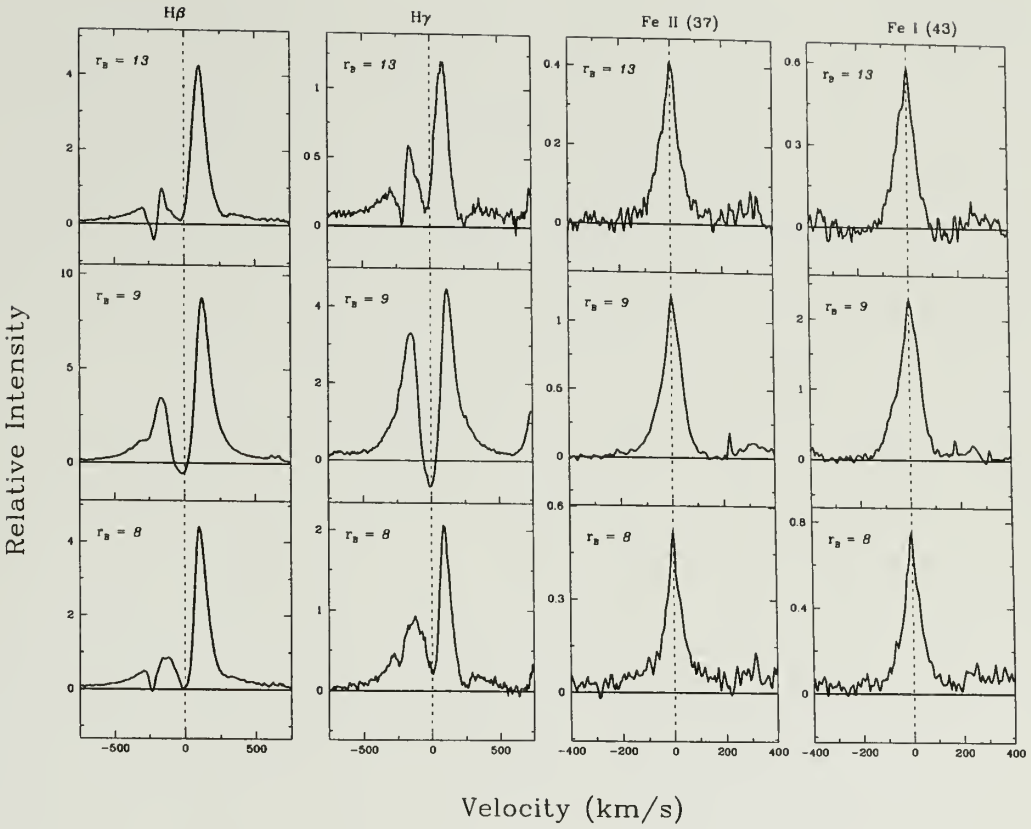

Figure 20. Residual emission profiles are shown for Hβ, Hγ, Fe II (37) λ4629 and Fe I (43) λ4064 for the 3 blue observing epochs, ordered by the magnitude of the veiling at λ4500 Å, r_B. The velocity scale for the Balmer lines is almost twice that for the other lines. The ordinate is in units of the continuum flux and the velocity is measured relative to the photosphere.

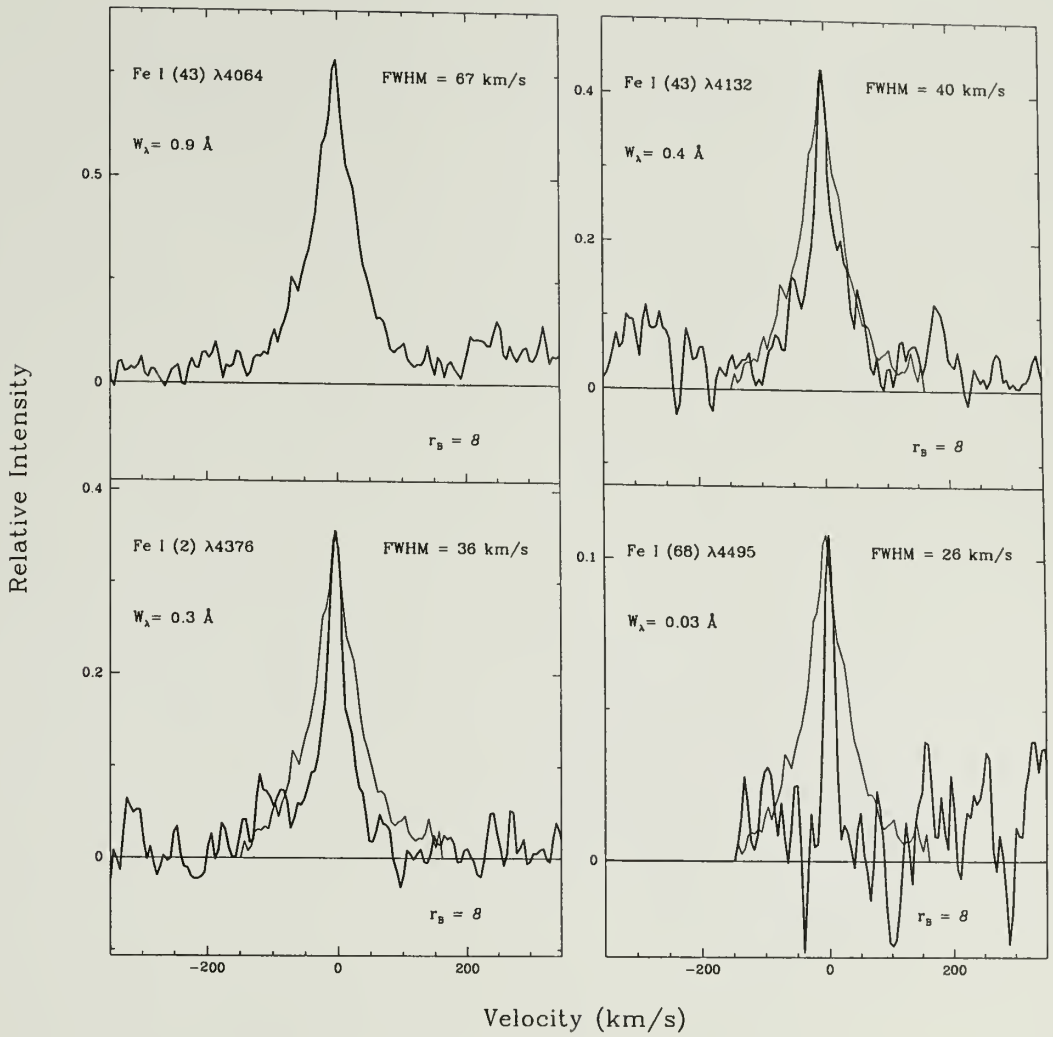

Figure 21. Four Fe I lines from the $r_B = 8$ spectrum show the variation in line width with line strength. The lines are ordered from the strongest to the weakest line, with the profile of the strongest line superposed on each profile. As the W_λ decreases from 0.9 Å to 0.03 Å the FWHM decreases from 67 to 26 km s^{-1}.

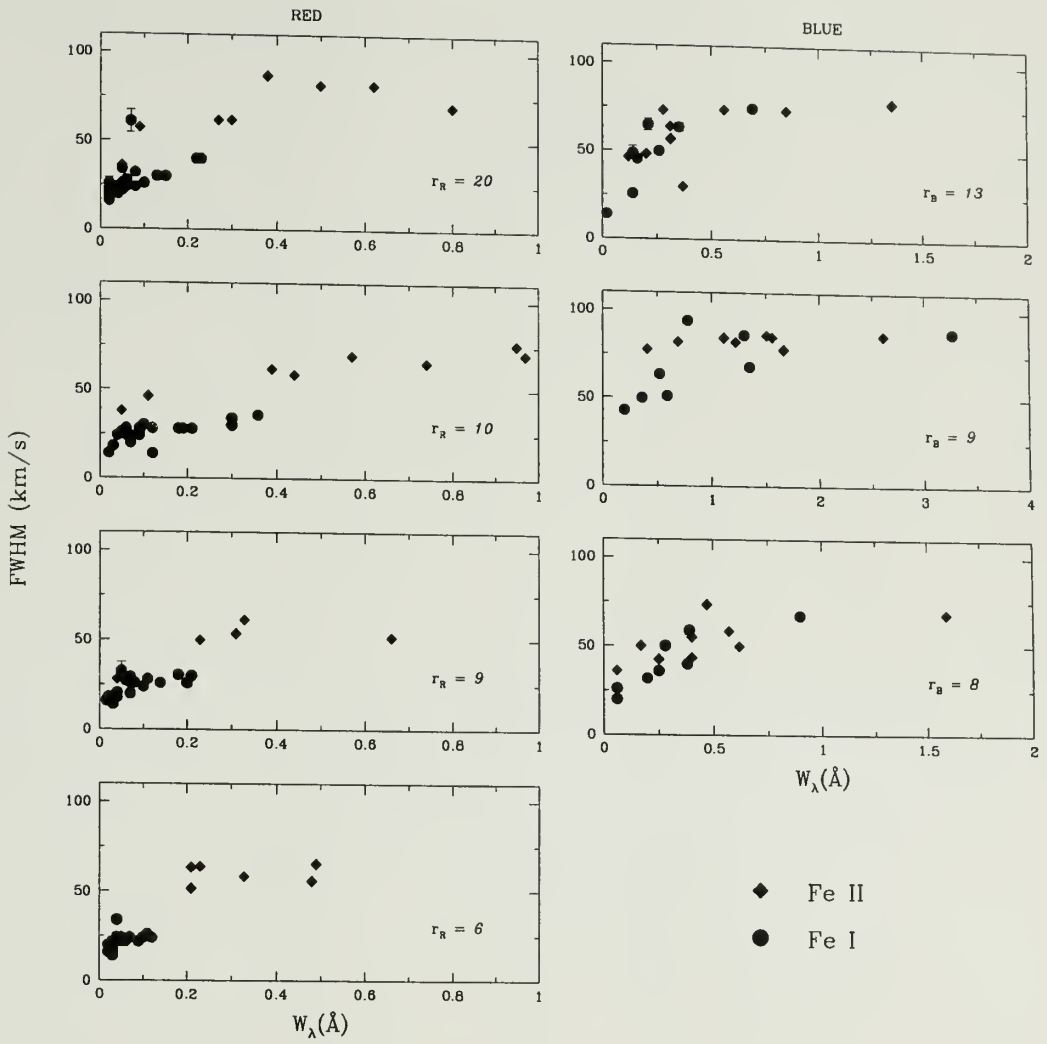

Figure 22. The FWHM of the 62 unblended Fe I and Fe II profiles is plotted against the line W_λ for each epoch of observation, illustrating the trend of increasing line width with increasing line strength. The 4 red spectra are in the left-hand panels, the 3 blue spectra in the right-hand panels and both are ordered by veiling. Circles denote lines of Fe I and squares denote lines of Fe II .

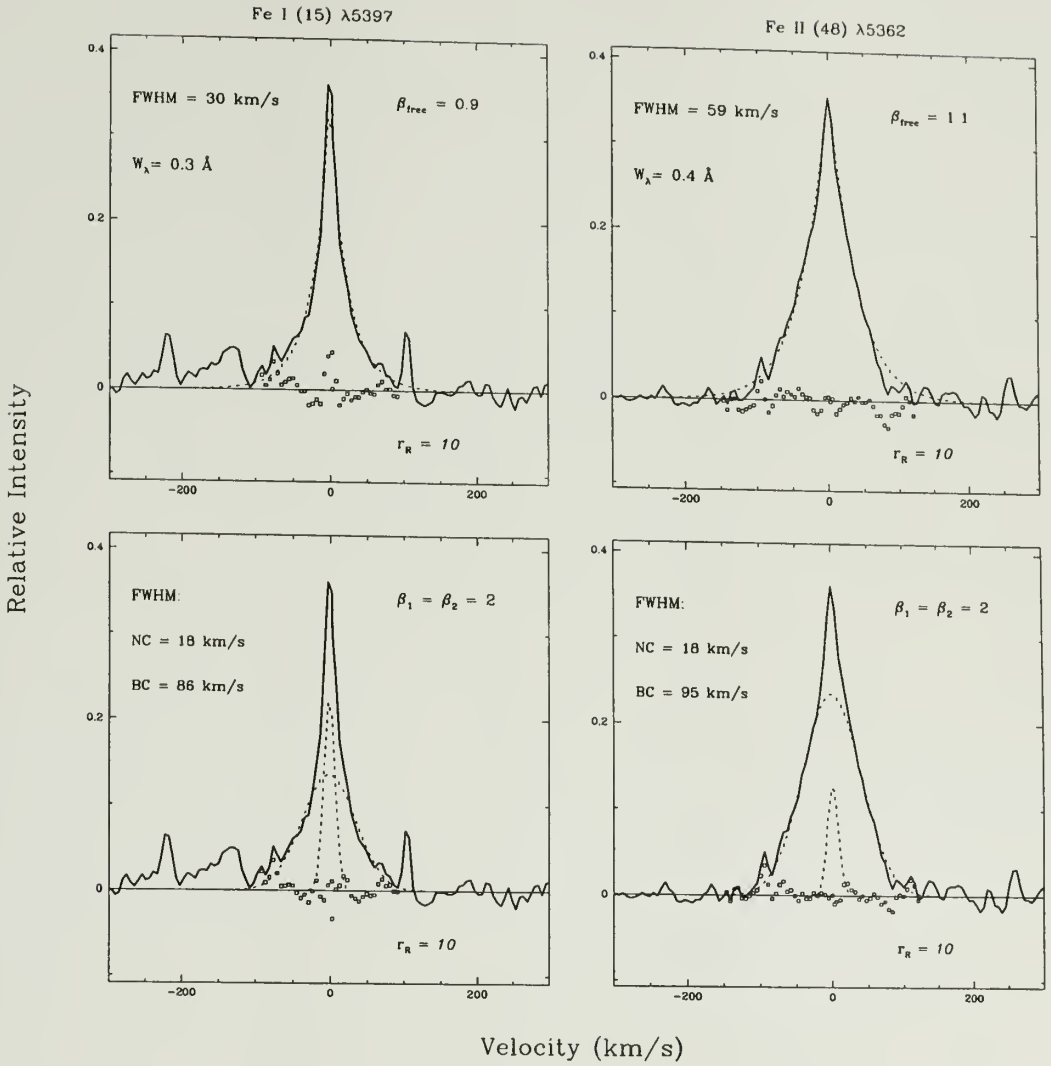

Figure 23. Single free shape and double Gaussian fits (dashed lines) are superposed on the observed profiles (solid lines) for a representative pair of lines, Fe I (15) and Fe II (48), at the $r_R = 10$ epoch. In each panel, the small open squares are the residuals between the observed and computed profiles. The single function fits (upper panels) yield a shape parameter $\beta \sim 1$, for both ions, although the Fe II line is twice as broad as Fe I . The bottom panels show double-Gaussian fits, with each profile decomposed into a narrow component (NC) and a broad component (BC). For each ion, the resultant line widths for the NC and the BC, respectively, are nearly identical.

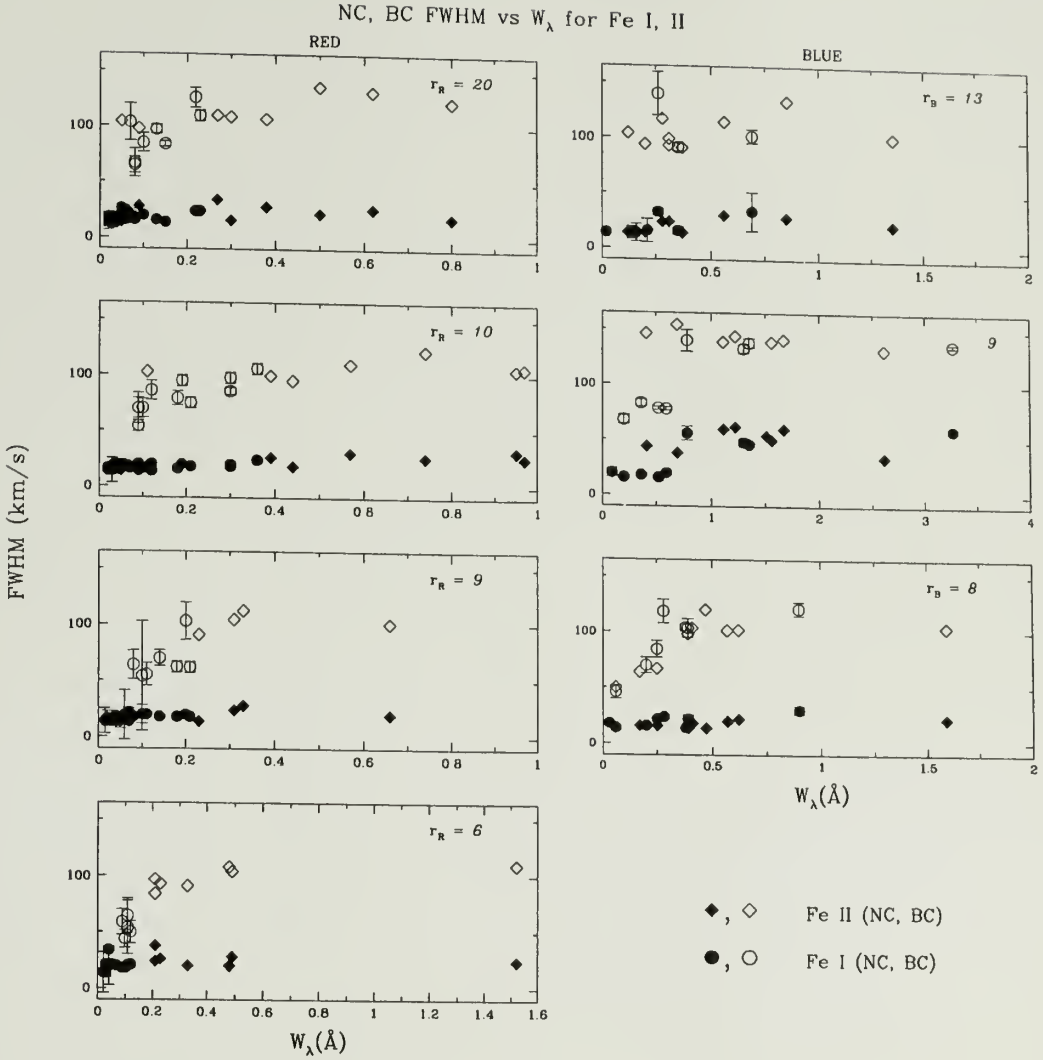

Figure 24. The FWHM for the two Gaussian components that fit the 62 unblended Fe I and Fe II profiles is plotted against the equivalent width. Each panel is a different observing epoch, with Fe I lines plotted as circles, and Fe II lines as squares. The average FWHM of the *NC* (filled symbols) from all measurements except those at the $r_B = 9$ epoch is $22 \pm 4\,\mathrm{km\,s^{-1}}$. The average FWHM of the *BC* (open symbols) from all lines with $W_\lambda > 0.1$ Å, except for the $r_B = 9$ spectrum, is $102 \pm 7\,\mathrm{km\,s^{-1}}$.

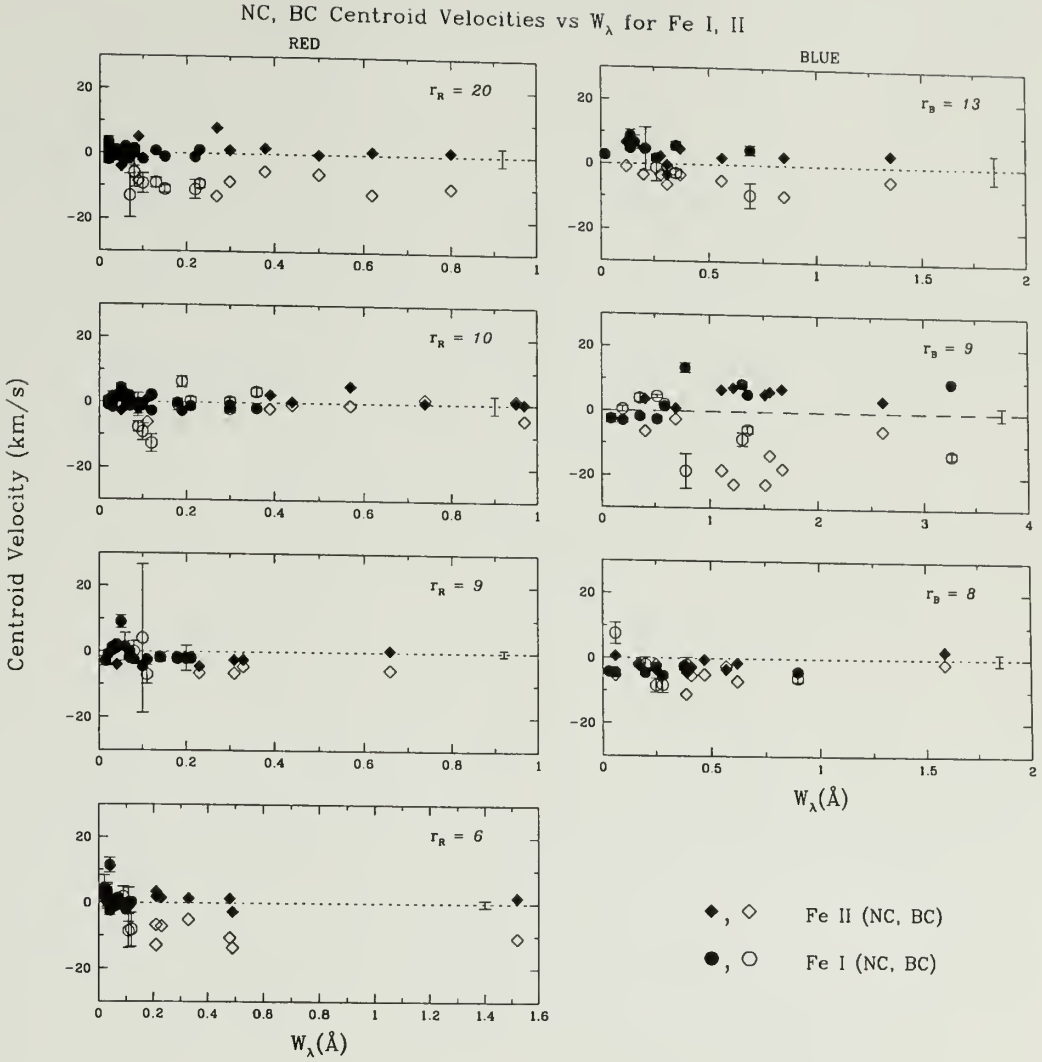

Figure 25. The velocity centroid for the *NC* and *BC* is plotted against the equivalent width. Each panel is a different observing epoch, with Fe I lines plotted as circles, and Fe II lines as squares. Velocities are relative to the stellar photosphere, except at $r_B = 9$, where photospheric lines are weak and measurements are relative to the average peak velocity for each ion. The *NC* average velocity from all measurements except those at $r_B = 9$, is $-1 \pm 2\,\mathrm{km\,s^{-1}}$. The *BC* average velocity varies from epoch to epoch, and ranges from 0 to -11 km s^{-1}. Error bars about the line of zero velocity are the uncertainties in the photospheric velocity.

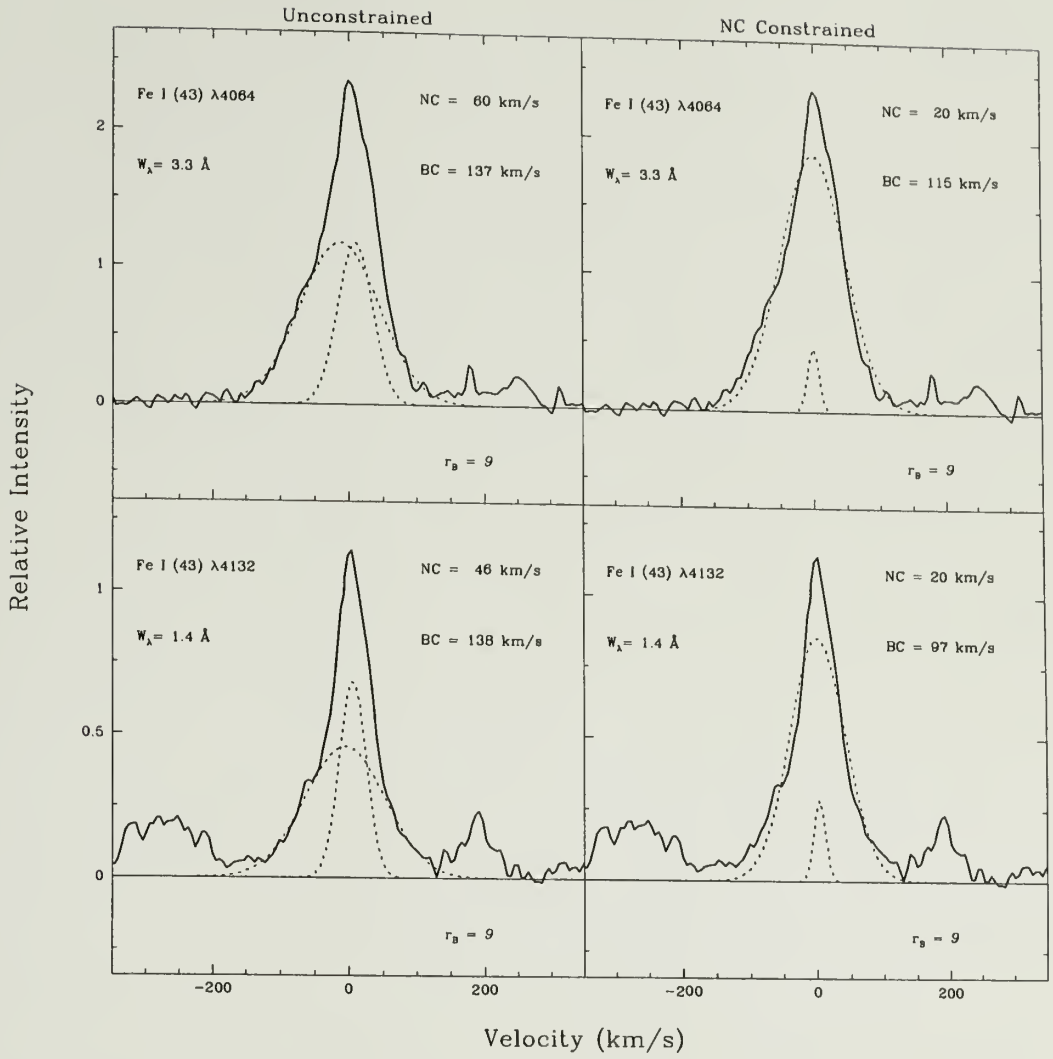

Figure 26. The left and right panels compare free and constrained fits for the anomalous $r_B = 9$ spectrum. **Left panels:** The Gaussian components from an unconstrained chi-square search on two Fe I profiles yield NC and BC widths significantly broader than those at other epochs. **Right panels:** The Gaussian components from a constrained chi-square search, with the NC set to a width of 20 km s^{-1} and a velocity centroid at the line peak, for the same two profiles. In each panel, the NC and BC fits are shown as dashed lines. The constrained fits yield NC and BC parameters which are consistent with those found from free fits at all other epochs. What distinguishes the $r_B = 9$ epoch is the low peak amplitude of a 20 km s^{-1} wide NC, with $\alpha_{NC} = 0.2$.

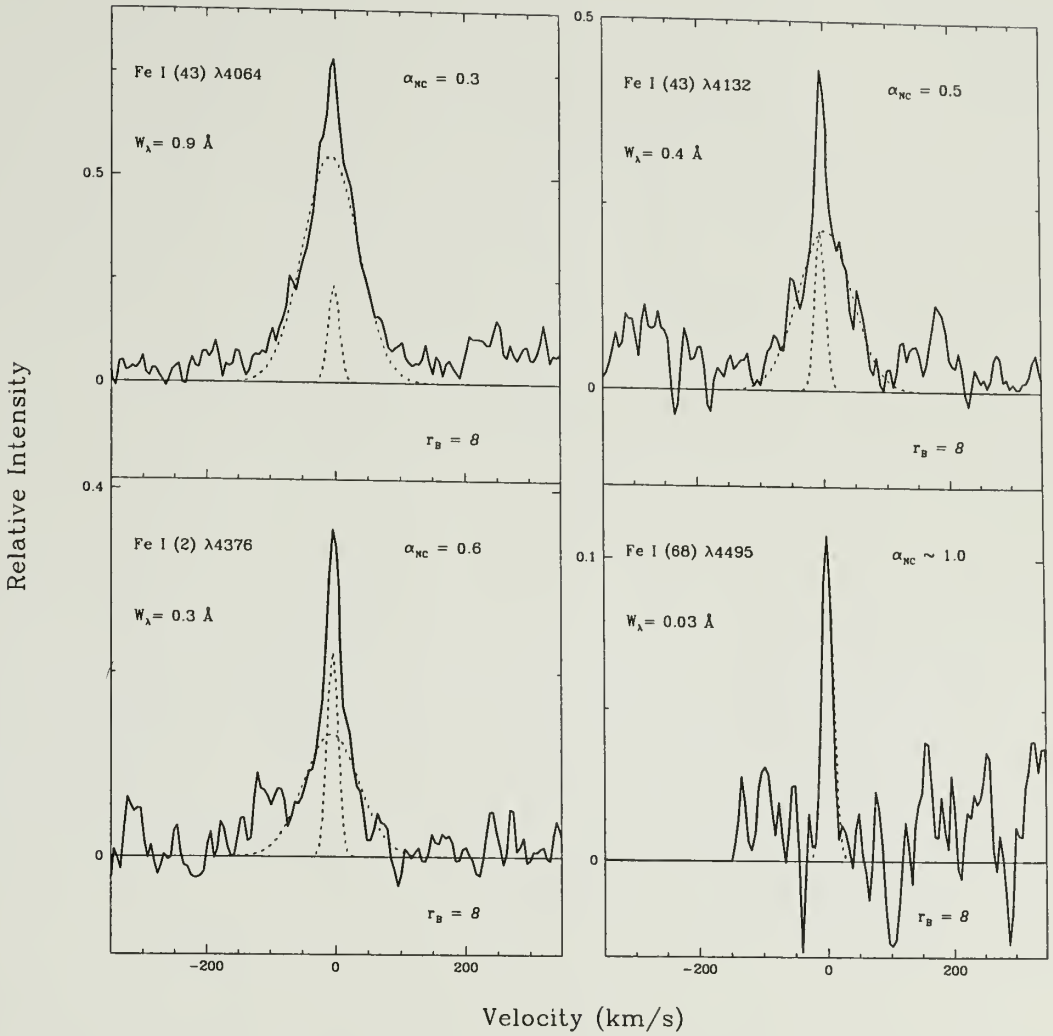

Figure 27. Four Fe I profiles from the $r_B = 8$ spectrum (identical to the set from Figure 21) are selected to illustrate how the *NC* peak amplitude, α_{NC}, depends on line strength. For each profile the two Gaussian components are shown with dashed lines. For the weakest line, $W_\lambda = 0.03$ Å and $\alpha_{NC} = 1.0$, while for the strongest line, $W_\lambda = 0.9$ Å and $\alpha_{NC} = 0.3$.

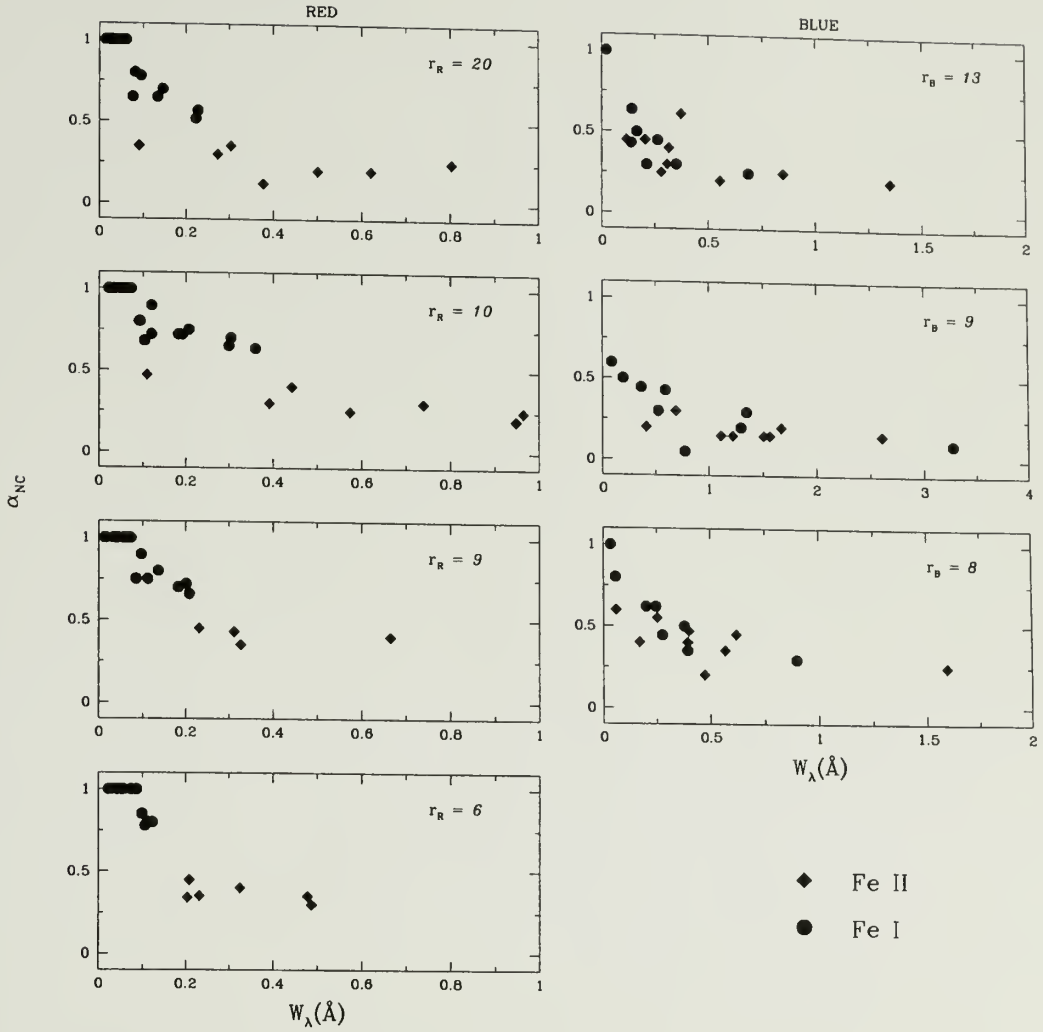

Figure 28. The relation between the NC peak amplitude, α_{NC}, and line strength for all 62 unblended Fe I and Fe II lines at each observing epoch is shown. The value of α_{NC} is ~ 1 for the weakest lines and is ~ 0.2 for the strongest lines. The exception is the $r_B = 9$ spectrum, where $\alpha_{NC} = 0.1$ for the strongest lines. In contrast to the fitting parameters shown in Figures 24 and 25, here we show the α_{NC} which results when the constrained NC fitting procedure is applied to all lines (see text).

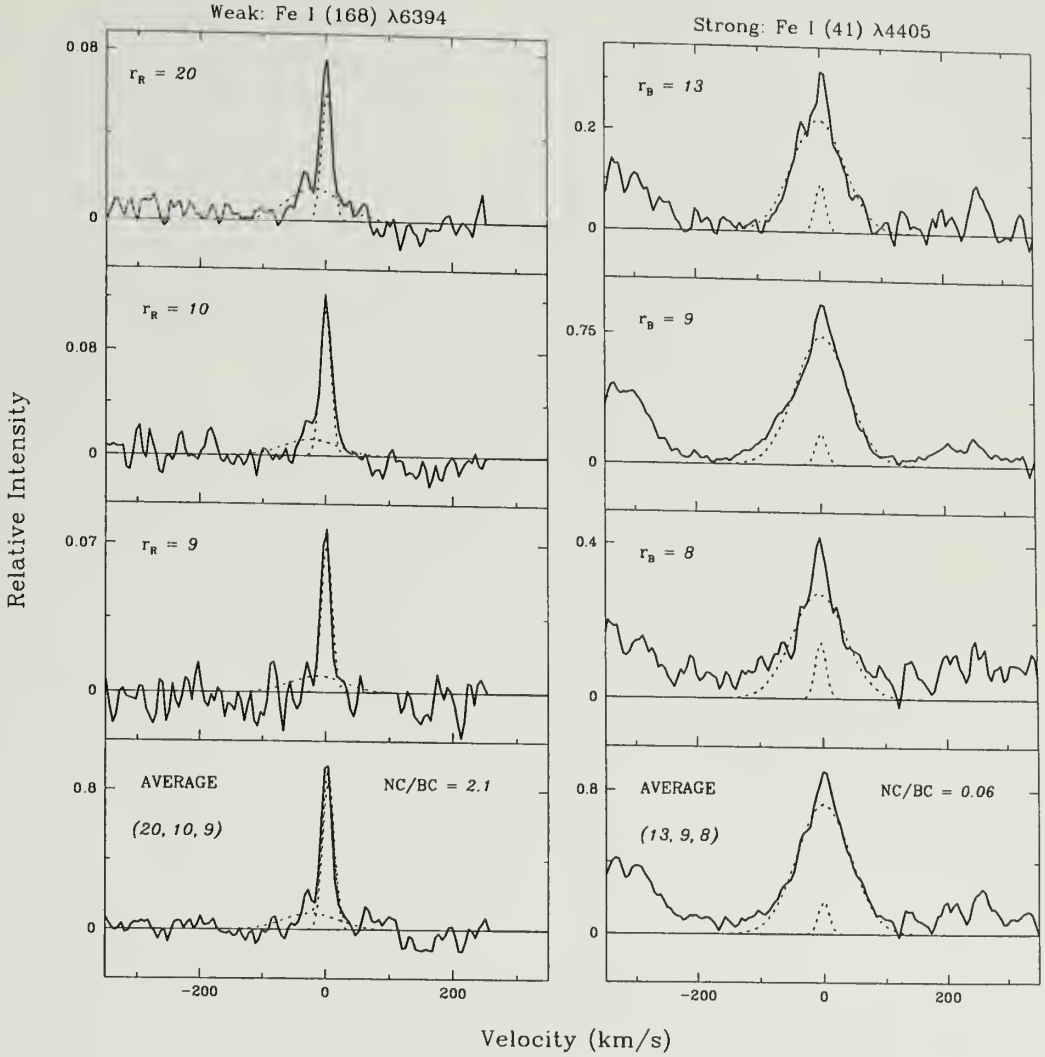

Figure 29. A pair of non-simultaneous Fe I lines arising from a common upper level with an A_{ij} ratio of 42. The left panels show 3 individual profiles of the weaker line in the pair, Fe I (168) λ6394, and the average of those 3 observations. At all epochs this line is dominated by the NC, with $\alpha_{NC} \sim 0.9$ and an equivalent width ratio of $NC/BC = 2.1$. In contrast, the right panels show the individual and average profiles for the stronger line of the pair, Fe I (41) λ4405. In this line the BC contribution dominates at all epochs, with average values of $\alpha_{NC} \sim 0.2$ and $NC/BC = 0.06$. In each panel, the NC and BC fits to each profile are shown as dashed lines.

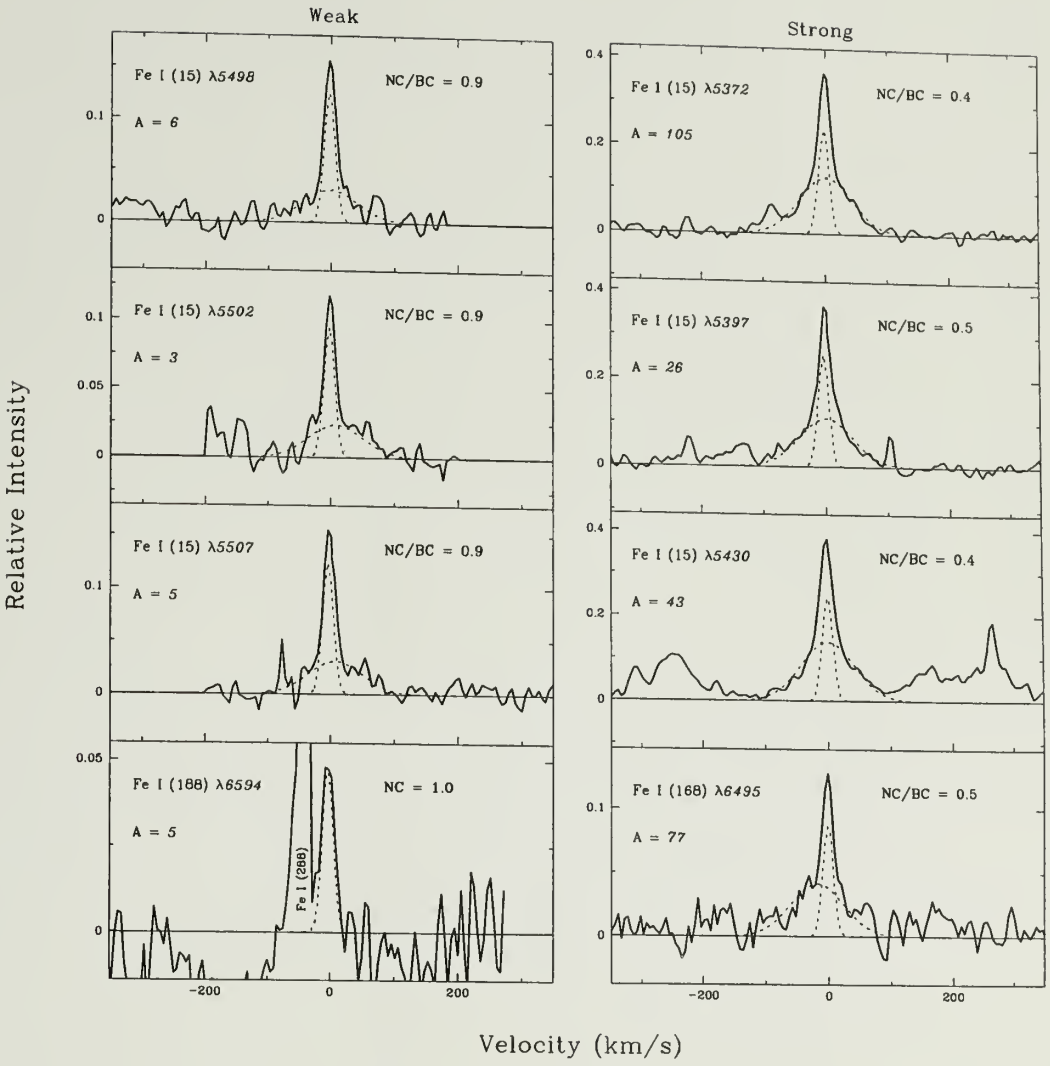

Figure 30. Profiles pairs of simultaneously observed Fe I lines arising from a common upper level are shown for the $r_R = 10$ epoch. Each pair comprises a weak (left panel) and a strong (right panel) member, i.e., in terms of the relative strength of the spontaneous emission rates A_{ij} in each line, shown in units of 10^4 s^{-1}. In contrast to the non-simultaneous pair in Figure 29, the ratio of NC/BC emission between these pair members differs only by a factor of two. The NC and BC fits to each profile are shown as dashed lines.

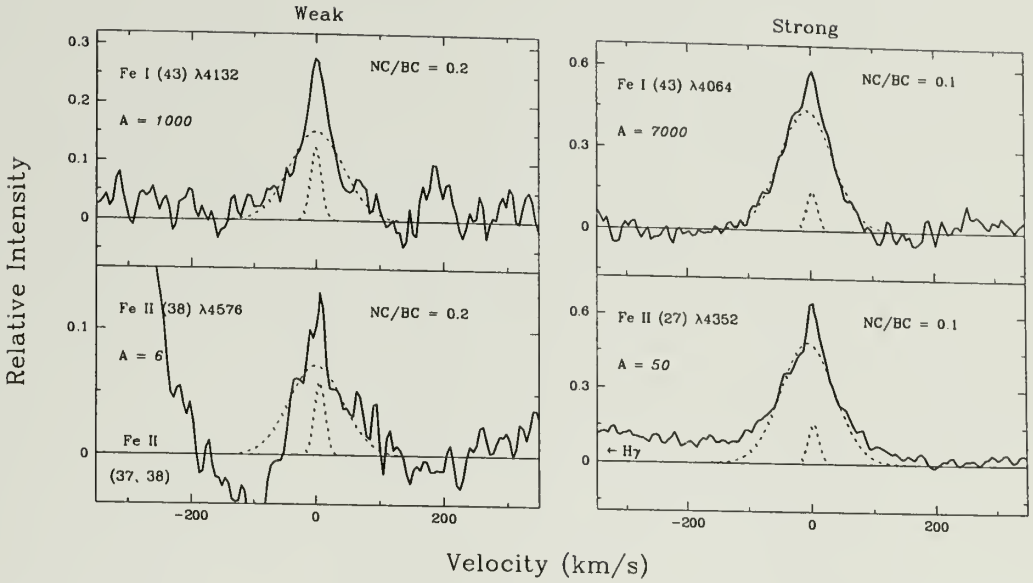

Figure 31. Profiles are shown for the 2 pairs of simultaneously observed Fe I and Fe II lines which arise from a common upper level at the $r_B = 13$ epoch. Each pair is composed of a weak (left panel) and a strong (right panel) member, which refers to the relative strength of the spontaneous emission rate A_{ij} in each line, shown in units of 10^4 s^{-1}. In contrast to the non-simultaneous pair in Figure 29, the ratio of NC/BC emission between these pair members differs only by a factor of two. The NC and BC fits to each profile are shown as dashed lines.

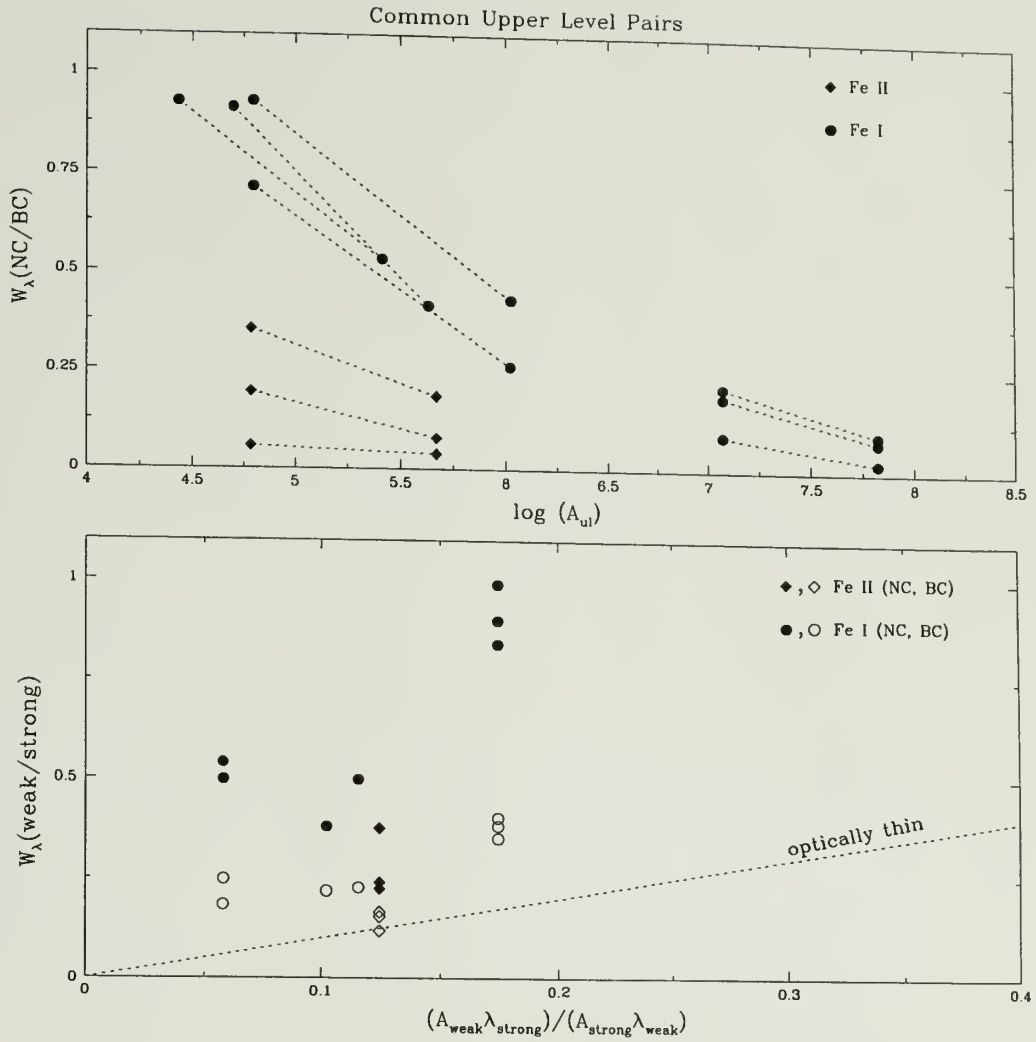

Figure 32. A comparison of the *BC* and *NC* emission for pairs of lines from a common upper level and for which the *BC* and *NC* can be reliably extracted. Included are 3 pairs from Fe I (15) at $r_R = 10$ and 1 pair from Fe I (15) at $r_R = 20$ in the red, and 1 pair each from Fe I (43) and Fe II (38), at all 3 epochs in the blue. In the upper panel the $W_\lambda(NC/BC)$ ratios are plotted against the spontaneous emission rate A_{ij}, with pair members joined by a dashed line. In the lower panel, the $W_\lambda(weak/strong)$ ratios for the *NC* and the *BC* are plotted against the expected value in the optically thin limit. For most pairs the ratios exceed the optically thin value, indicating that in both the *NC* and the *BC* the stronger line at least is optically thick. Also for most pairs, the ratio for the *NC* exceeds that for the *BC*, suggesting a greater opacity in the *NC* emission.

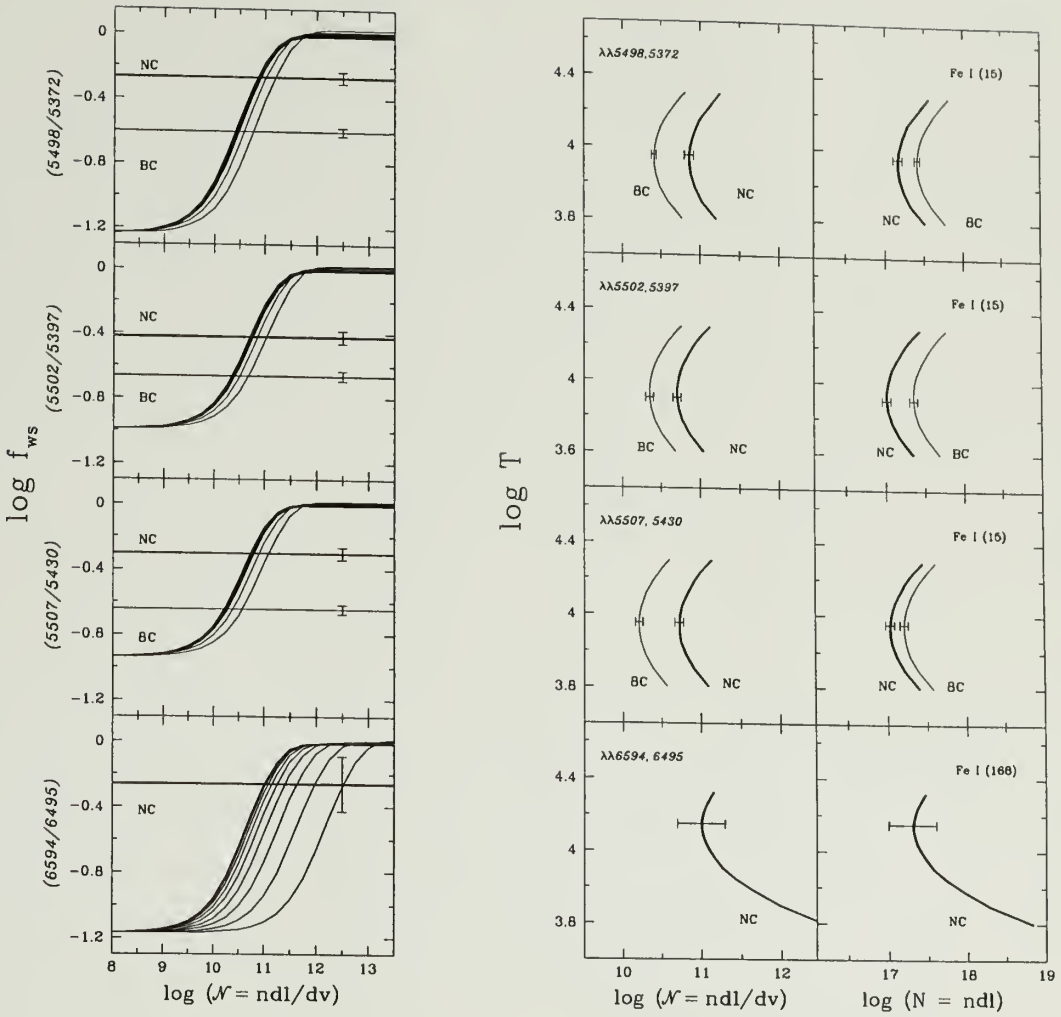

Figure 33. Results for the column densities from the Sobolev calculations, for the 4 common upper level line pairs from our red spectra. *Left panels:* Curves of growth relating f_{ws}, the intensity ratio of the weak to the strong line in each pair, to $\mathcal{N} = ndl/dv$, plotted for temperatures between $4{,}000 \leq T \leq 20{,}000$ K. Horizontal lines are the observed values of f_{ws} in the *NC* and the *BC*. *Center panels:* Theoretical loci of $\mathcal{N}$ and T compatible with the observed f_{ws} ratios shown in the growth curves, for the *NC* and the *BC*. *Right panels:* Theoretical loci of N and T, with $N = ndl \approx \mathcal{N}\Delta v$ calculated from the results in the center panels. The conversion from $\mathcal{N} = ndl/dv$ to a standard column density via Δv for each component shifts what were distinctly lower values of $\mathcal{N}$ for the *BC* to values of N that are comparable between the *NC* and the *BC*.

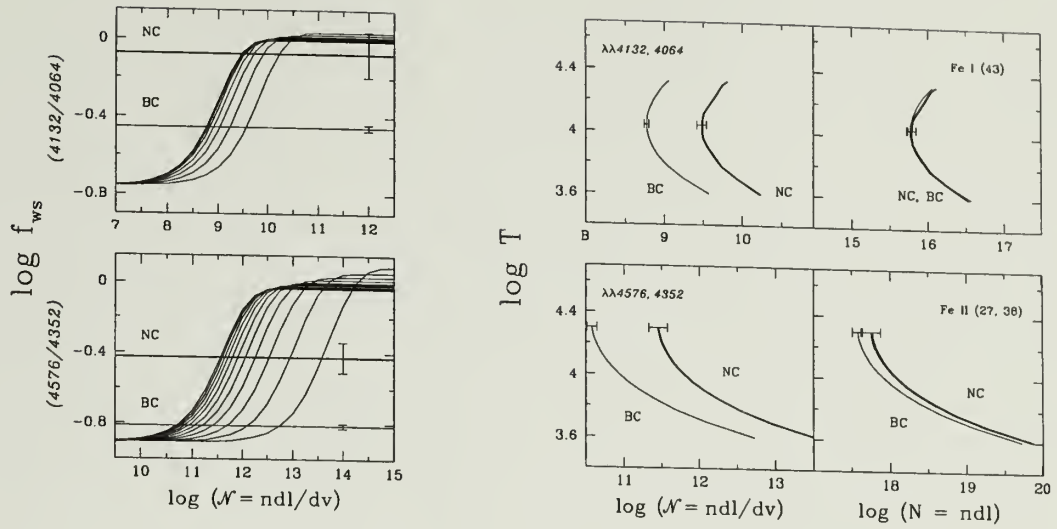

Figure 34. Results from the Sobolev LVG calculations for the 2 common upper level line pairs from our blue spectra. *Left panels:* Curves of growth relating f_{ws}, the intensity ratio of the weak to the strong line in each pair, to $\mathcal{N} = ndl/dv$. Growth curves in each panel are plotted for temperatures between 4,000 $\leq T \leq$ 20,000 K. Horizontal lines are the observed values of f_{ws} in the *NC* and the *BC*. *Center panels:* The theoretical loci of $\mathcal{N}$ and T compatible with the observed f_{ws} ratios shown in the growth curves, for the *NC* and the *BC*. *Right panels:* The theoretical loci of N and T, where $N = ndl \approx \mathcal{N}\Delta v$, calculated from the results in the center panels. In the conversion from $\mathcal{N} = ndl/dv$ to a standard column density via Δv for each component shifts what were distinctly lower values of $\mathcal{N}$ for the *BC* to values of N that are comparable between the *NC* and the *BC*. Thus for T between 4,000 and 20,000 K there is no significant difference in the column densities of the *NC* and *BC*.

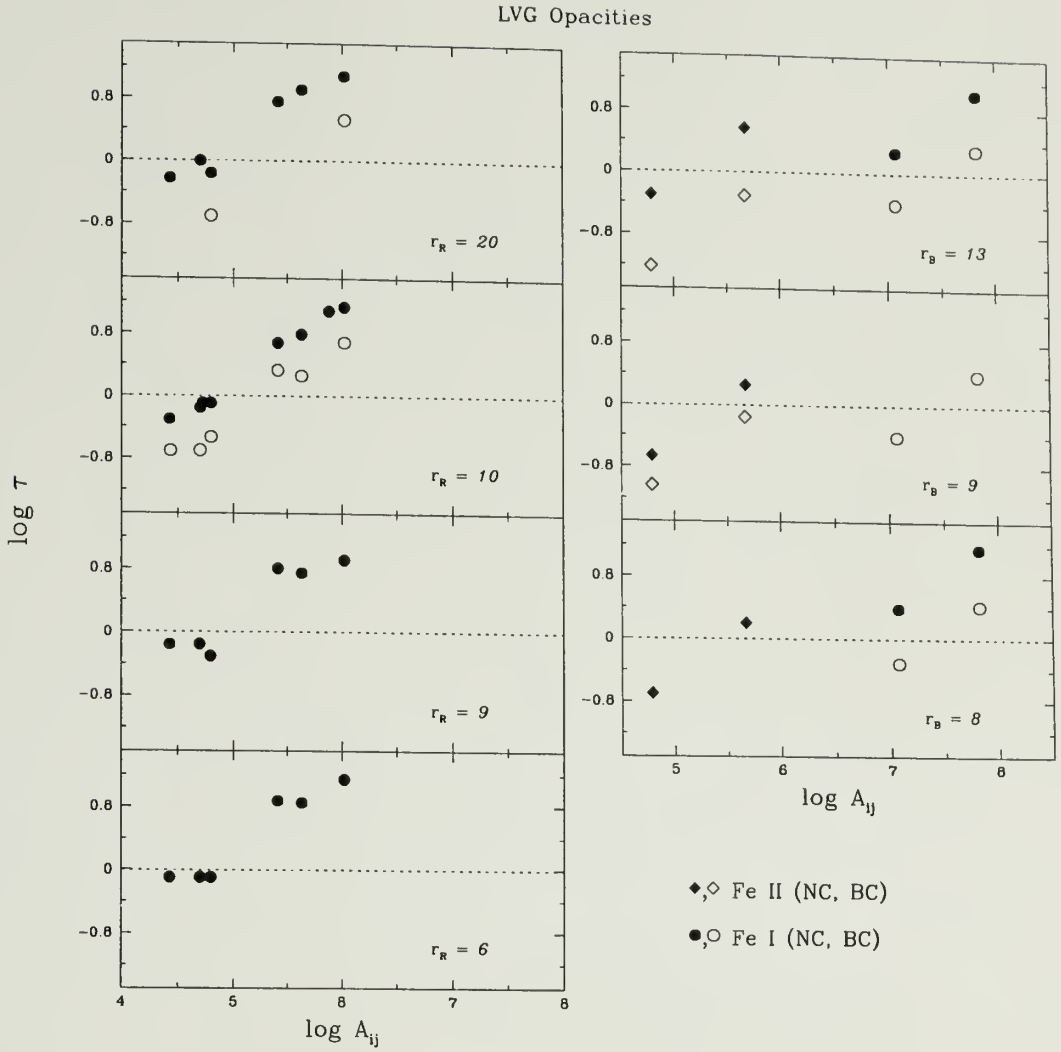

Figure 35. Opacities for the lines in our 6 common upper level line pairs, shown for each epoch of observation. The opacities can be derived from the growth curves of Figures 33 and 34, but are independent of $\mathcal{N}$ and T (see text). Derived values range from about 0.1 to 10 for these lines. The data suggest that the optical depth of the *NC* exceeds that of the *BC* by a factor of 2-4 in each line, consistent with the trend inferred from the comparison of the observed line ratios with their optically thin values shown in Figure 32.

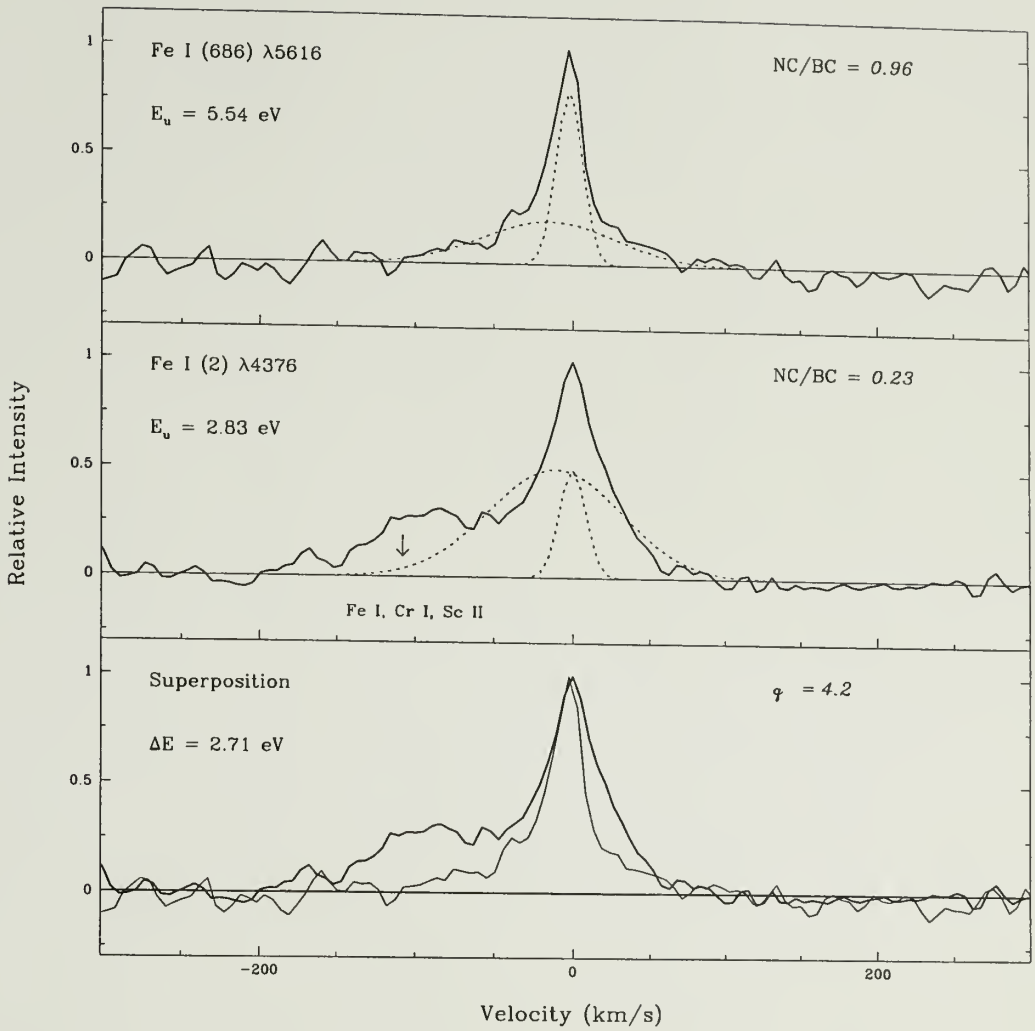

Figure 36. Average profiles are shown for the two Fe I lines which are insensitive to opacity (see §3.5.3). In the top two panels, the *NC* and *BC* fits for each average profile are shown as dashed lines. The lower panel superposes the two average profiles to facilitate their comparison. The temperature sensitive parameter $q = [W_\lambda(\frac{NC}{BC})_{5616}/W_\lambda(\frac{NC}{BC})_{4376}] = 4.2$.

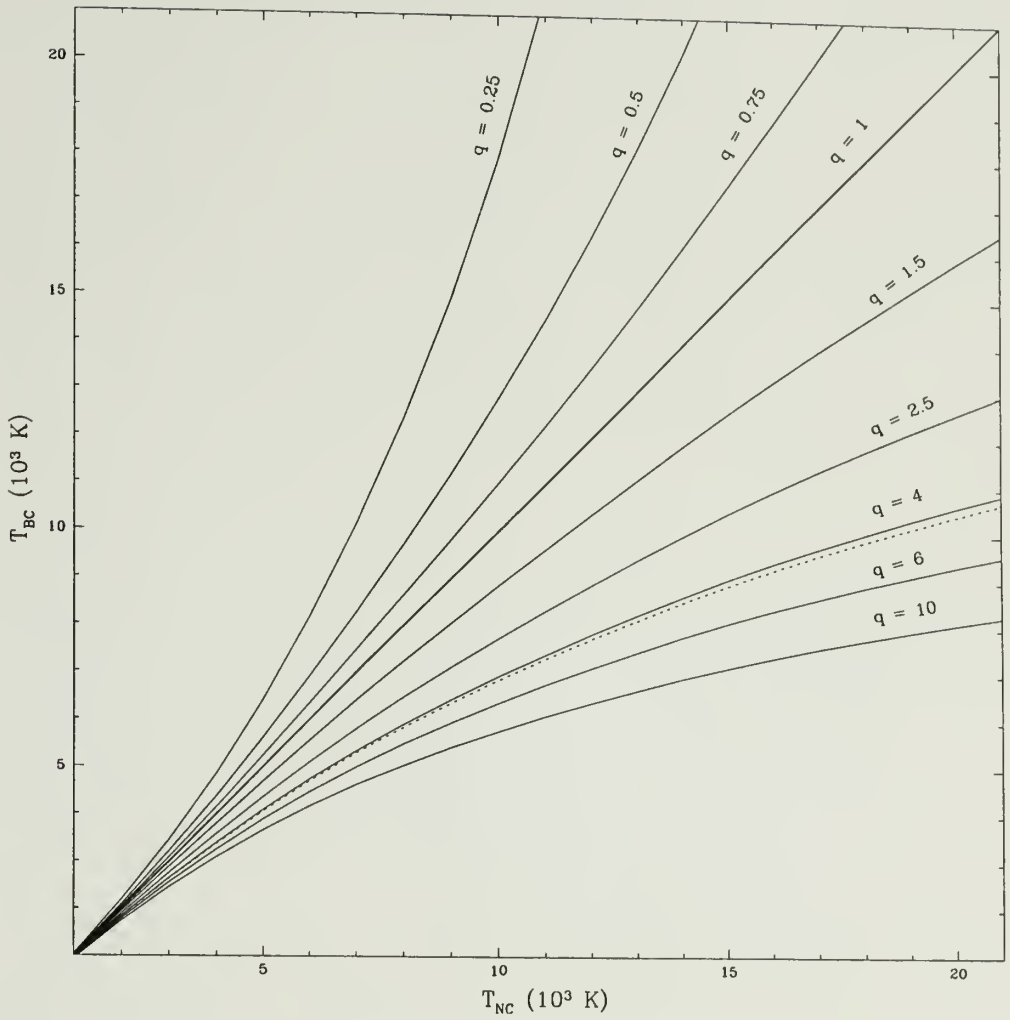

Figure 37. The relative values of T_{NC} and T_{BC} are shown for $10 \geq q \geq 0.25$, where $q = [W_\lambda(\frac{NC}{BC})_{5616}/W_\lambda(\frac{NC}{BC})_{4376}]$ (see §3.5.3). Curves of constant q are plotted at q = 10, 6, 4, 2.5, 1.5, 1, 0.75, 0.5, and 0.25. At q = 1, $T_{NC} = T_{BC}$. The observed q of 4.2 $\pm$1.7, corresponding to the regime where $T_{NC} > T_{BC}$, is shown as a dashed line. For example, if $T_{NC} = 10^4$ K, then $T_{BC} = 6900$ K.

BIBLIOGRAPHY

Aiad, A., Appenzeller, I., Bertout, C., Isobe, S., Shimizu, M., Stahl, O., Walker, M. F., & Wolf, B. 1984, *A&A*, **130**, 67

Alencar, S.H.P., & Basri, G. in print

Appenzeller, I., Reitermann, A., & Stahl, O. 1988, *PASP*, **100**, 815

Appenzeller, I., Jankovics, I., & Jetter, R. 1986, *A&AS*, **64**, 65

Appenzeller, I., Krautter, J., Smolinski, J., & Wolf, B. 1980, *A&A*, **86**, 113

Armitage, P.J., & Clarke, C.J. 1996, *MNRAS*, **280**, 458

Artymowicz P., & Lubow, S.H. 1996, *ApJ*, **467**, L77

Athay, R.G. 1965, *ApJ*, **142**, 755

Athay, R.G., & Johnson, H.R. 1960, *ApJ*, **131**, 413

Avrett, E.H., Vernazza, J.E., & Linsky, J.L. 1976, *ApJ*, **207**, L199

Bard, A., Kock, A., & Kock, M. 1991, *A&A*, **248**, 315

Basri, G., Johns-Krull, C.M., & Mathieu, R.D. 1997, *AJ*, **114**, 781

Basri, G., & Batalha, C.C. 1990, *ApJ*, **363**, 654

Basri, G., & Bertout, C. 1989, *ApJ*, **341**, 340

Batalha, C.C., Stout-Batalha, N.M., Basri, G., & Terra, M.A.O. 1996, *ApJS*, **103**, 211

Beristain, G., Edwards, S., & Kwan, J. 1998, *ApJ*, **499**, 828

Bertout, C. 1989, *ARA&A*, **27**, 351

Bertout, C., Basri, G., & Bouvier, J. 1988, *ApJ*, **330**, 350

Bertout, C., Krautter, J., Möllenhof, C., & Wolf, B. 1977, *A&A*, **61**, 737

Boesgaard, A.M. 1984, *AJ*, **89**, 1635

Bouvier, J., Covino, E., Kovo, O., Martín, E.L., Mathews, J.M., Terranegra, L., & Beck, S.C. 1995, *A&A*, **299**, 89

Bouvier, J., Cabrit, S., Fernández, M., Martín, E.L., & Mathews, J.M. 1993, *A&A*, **272**, 176

Brocklehurst, M. 1972, *MNRAS*, **157**, 211

Brown, A., de M. Ferraz, M.C., & Jordan C. 1984, *MNRAS*, **207**, 831

Calvet, N., & Gullbring, E. 1998, *ApJ*, **509**, 802

Calvet, N., & Hartmann, L.W. 1992, in *Seventh Cambridge Workshop on Cool Stars, Stellar Systems, and the Sun*, ed. M.S. Giampapa & J.A. Bookbinder (Berlin: Springer)

Calvet, N., Hartmann, L.W., Hewett, R. 1992, *ApJ*, **386**, 229

Calvet, N., Basri, G., Imhoff, C.L., & Giampapa, M.S. 1985, *ApJ*, **293**, 575

Calvet, N., Basri, G., Kuhi, L.V. 1984, *ApJ*, **277**, 725

Camenzind, M. 1997, in IAU Symposium 182, *Herbig Haro Flows & the Birth of Low Mass Stars,* ed. B. Reipurth & C. Bertout (Dordrecht: Kluwer), 241

Camenzind, M. 1990, *RevModAstron*, **3**, 234

Cram, L.E. 1979, *ApJ*, **234**, 949

Edwards, S. 1997, in IAU Symposium 182, *Herbig Haro Flows & the Birth of Low Mass Stars,* ed. B. Reipurth & C. Bertout (Dordrecht: Kluwer), 433

Edwards, S., Hartigan, P., Ghandour, L., & Andrulis, C. 1994, *AJ*, **108**, 1056 [EHGA]

Edwards, S., Strom, S.E., Hartigan, P., Strom, K.M., Hillenbrand, L.A., Herbst, W., Attridge, J., Merrill, K.M., Probst, R., & Gatley, I. 1993, *AJ*, **106**, 372

Fuhr, J.R., Martin, G. A., & Wiese, W.L. 1988, *JPhysChemRefData*, **17**, Supplement 4

Ghosh P. 1995, *MNRAS*, **272**, 763

Ghosh P., Lamb, F.K., & Pethick, C.J. 1977, *ApJ*, **217**, 578

Giridhar, S., & Arellano Ferro, A. 1995, *RevMexAA*, **31**, 23

Goldberg, L. 1939, *ApJ*, **89**, 673

Gomez de Castro, A., & Franqueira, M. 1997, *IUE-ULDA Access Guide No. 8*, ESA SP1205

Guenther, E., & Hessman, F.V. 1993, *A&A*, **268**, 192

Gullbring, E., Hartmann, L., Briceno, C., & Calvet, N. 1998, *ApJ*, **492**, 323

Gullbring, E., Petrov, P.P., Ilyin, I., Tuominen, I., Gahm, G.F., & Loden, K. 1996, *A&A*, **314**, 835

Hamann, F., & Persson, S.E. 1992, *ApJS*, **82**, 247

Hartigan, P., Edwards, S., & Ghandour, L. 1995, *ApJ*, **452**, 736 [HEG]

Hartigan, P., Hartmann, L., Kenyon S., Strom, S.E., & Skrutskie, M.F. 1990, *ApJ*, **354**, L25

Hartmann, L., Calvet, N., Gullbring, E., & D'Alessio, P. 1998, *ApJ*, **495**, 385

Hartmann, L. 1998, *Accretion Processes in Star Formation* (Cambridge: Cambridge University Press)

Hartmann, L. 1997, in IAU Symposium 182, *Herbig Haro Flows & the Birth of Low Mass Stars,* ed. B. Reipurth & C. Bertout (Dordrecht: Kluwer), 391

Hartmann, L., Hewett, R., & Calvet, N. 1994, *ApJ*, **426**, 669 [HHC]

Hartmann, L., Calvet, N., Avrett, E.H., & Loeser, R. 1990, *ApJ*, **349**, 168

Hartmann, L., Edwards, S., & Avrett, E.H. 1982, *ApJ*, **261**, 279

Hartmann, L. 1982, *ApJS*, **48**, 109

Heasley, J.N., Mihalas, D., & Poland, A.I. 1974, *ApJ*, **192**, 181

Heise, C., & Kock, M. 1990, *A&A*, **230**, 244

Herbig, G.H. 1962, *AdvAstr&Ap,* **1**, 47

Hessman, F.V., & Guenther, E. 1997, *A&A*, **321**, 497

Hirayama, T. 1971, *Sol. Phys.*, **17**, 50

Hirth, G., Mundt, R., & Solf, J. 1997, *A&AS*, **126**, 437

Isobe, S., Norimoto, Y., & Kitamura, T. 1988, *PASJ*, **40**, 89

Johns-Krull, C.M., & Basri, G. 1997, *ApJ*, **474**, 433

Joy, A.H. 1945, *ApJ*, **102**, 168

Kenyon, S.J., Hartmann, L., Hewett, R., Carrasco, L., Cruz-Gonzalez, I., Recillas, E., Salas, L., Serrano, A., Strom, K.M., Strom, S.E., & Newton, G. 1994, *AJ*, **107**, 2153

Kock, M., Kroll, S., & Schnehage, S. 1984, *Phys. Scr*, **T8**, 84

Königl, A. 1991, *ApJ*, **370**, L39

Krautter, J., Appenzeller, I., & Jankovics, I. 1990, *A&A*, **236**, 416

Krautter, J., & Bastian, U. 1980, *A&A*, **88**, L6

Kuhi, L.V. 1964, *ApJ*, **140**, 1409

Kwan, J. 1997, *ApJ*, **489**, 284

Kwan, J., & Tademaru, E. 1995, *ApJ*, **454**, 382

Kwan, J., & Tademaru, E. 1988, *ApJ*, **332**, L41

Lago, M.T.V.T. 1982, *MNRAS*, **168**, 603

Lamzin, S.A., 1989, *AZh*, **66**, 1330

Leinert, C., Zinnecker, H., Weitzel, N., Christou, J., Ridgway, S.T., Jameson R., & Haas, M. 1993, *A&A*, **278**, 129

Li, J., Wickramasinghe, D., & Ruediger, G. 1996, *ApJ*, **469**, 765

Lynden-Bell, D., & Pringle, J.E. 1974, *MNRAS*, **168**, 603

Mathieu, R.D., Stassun, K., Basri, G., Jensen, E.L.N., Johns-Krull, C.M., Valenti, J. A., & Hartmann, L.W. 1997, *AJ*, **113**, 1841

Mathieu, R.D., Martin, E.L., & Magazzu, A. 1996, *BAAS*, **28**, 920 (188th AAS Meeting, abstract number 60.05)

Mathieu, R.D., 1994, *ARA&A*, **32**, 465

Mitskevich, A.S., Natta, A., & Grinin, V.P. 1993, *ApJ*, **404**, 751

Moore, C.E., Minnaert, M.G.J., & Houtgast, J. 1966, *The Solar Spectrum 2935λ to 8770λ, National Bureau of Standards Monograph 61* (Washington, D.C.: US Government Printing Office)

Mundt, R. 1984, *ApJ*, **280**, 749

Muzerolle, J., Calvet, N., & Hartmann, L. 1998, *ApJ*, **492**, 743 [MCH]

Muzerolle, J., Hartmann, L., Calvet, N. 1998, *ApJ*, **116**, 455

Najita, J., & Shu, F. H. 1994, *ApJ*, **429**, 808

Natta, A. 1999, *'Star Formation' in Infrared Space Astronomy, To-day and To-morrow*, eds. F. Casoli, F. David, & J. Lequeux, EDP-Sciences (Berlin: Springer-Verlag)

Natta, A., & Giovanardi, C. 1990, *ApJ*, **356**, 646

Nave, G., Johansson, S., Learner, R.C.M., Thorne, A.P., & Brault, J.W. 1994, *ApJS*, **94**, 221

O'Brian, T. R., Wickliffe, M.E., Lawler, J.E, Whaling, W., & Brault, J.W. 1991, *JOptSocAm B*, **8**, 1185

Osterbrock, D.E. 1974, *Astrophysics of Gaseous Nebulae* (San Francisco: Freeman)

Ostriker E., & Shu, F. 1995, *ApJ*, **447**, 813

Paatz, G., & Camenzind, M. 1996, *A&A*, **308**, 77

Press, W.H., Teukolsky, S.A., Vetterling, W.T., & Flannery, B.P. 1992, *Numerical Recipes in C: The Art of Scientific Computing, 2nd ed.* (New York: Cambridge University Press)

Safier, P. 1977, *ApJ*, in press

Schneeberger, T.J., Linsky, J.L., & Worden, S.P. 1978, *A&A*, **62**, 447

Shu, F.H., Najita, J., Ostriker, E., Wilken, F., Ruden, S., & Lizano, S. 1994, *ApJ*, **429**, 781

Simon, M., & Prato, L. 1995, *ApJ*, **450**, 824

Simon, M., et al 1995, *ApJ*, **443**, 625

Simon, M., Chen, W.P., Howell, R.R., Benson, J.A., & Slowik, D. 1992, *ApJ*, **384**, 212

Smith, K.W., Bonnell, I.A., Lewis, G.F., & Bunclark, P.S. 1997, *MNRAS*, **289**, 151

Smits, D.P. 1996, *MNRAS*, **278**, 683

Smits, D.P. 1991, *MNRAS*, **248**, 193

Thiébaut, E., Balega, Y., Balega, I., Belkine, I., Bouvier, J., Foy, R., Blazit, A., and Bonneau, D. 1995, *A&A*, **304**, L17

Uchida, Y., & Shibata, K. 1985, *PASJ*, **37**, 515

Ulrich, R.K., & Wood, B.C. 1981, *ApJ*, **244**, 147

Van Ballegooijen, A.A. 1994, *SpaceSciRev*, **68**, 299

Wahlstrom, C., & Carlsson, M. 1994, *ApJ*, **433**, 417

Wiese, W.L., Smith, M.W., & Glennon, B.M. 1966, *Atomic Transition Probabilities Hydrogen through Neon* (NSRDS-NBS 4)

Willson, L.A. 1975, *ApJ*, **197**, 365

Willson, L.A. 1974, *ApJ*, **191**, 413

Wolff, S.C., & Heasley, J.N. 1984, *PASP*, **96**, 231

Zirin, H. 1975, *ApJ*, **199**, L163